Synthesis and Characterization of Nanostructured Electro-active Materials

Peiqi Wang

A dissertation

submitted in partial fulfillment of the

requirements for the degree of

Doctor of Philosophy

University of Washington

2016

Reading Committee:

Jiangyu Li, Chair

Guozhong Cao

Stuart B. Adler

Program Authorized to Offer Degree:

Mechanical Engineering

University of Washington

Abstract

Synthesis and Characterization of Nanostructured Electro-active Materials

Peiqi Wang

Chair of the Supervisory Committee:
Professor Jiangyu Li
Mechanical Engineering

With the rapidly increasing demand for better energy sources, material development for alternative energy storage and conversion systems has become extremely important. Among those, lithium ion batteries have achieved huge success in commercial use; however, progress still needs to be made to improve the performance. Toward this end, nanostructured materials have emerged as potential solutions toward smaller, cheaper, safer, and longer lasting batteries. One part of this dissertation focuses on the synthesis and characterization of nanostructured carbon materials for lithium ion batteries using electrospinning and nanoimprint lithography as primary synthesis methods. By appropriate nanostructuring, we have achieved improvement in electrochemical performance compared to that of the current state-of-art graphite anode, yet more effort is needed for further advancement.

The other major portion of this dissertation is on the use of various scanning probe microscopy techniques to thoroughly characterize synthetic ferroelectrics for solar cell applications, and biological ferroelectrics for bio-compatible molecular electronics. The fundamentals of each scanning probe microscopy technique are first introduced, followed by a description of how they are applied to the ferroelectric materials to study different properties and behaviors. By combining piezoresponse force microscopy (PFM) and Kelvin probe force microscopy, we are able to establish solid proof that the perovskite is indeed ferroelectric, and also to observe the charge separation process when used as the light absorber layer in solar cells. More importantly, we investigated how the external light illumination interacts with the intrinsic ferroelectricity, to help understand the role of ferroelectricity in its superior performance in solar cells. PFM and conductive atomic force microscopy (c-AFM) also applied to study the ferroelectric resistive switching behavior in the biological ferroelectric elastin and its monomer level tropoelastin. Experimentally, we observed switchable diode-like conductance behavior and strong correlation to ferroelectric polarization which opens up new applications for those biological tissues.

TABLE OF CONTENTS

TABLE OF CONTENTS

LIST OF FIGURES

LIST OF TABLES

ACKNOWLEDGEMENTS

I would like to convey my deep appreciation to my advisor, Professor Jiangyu Li, for his guidance, support and also trust over the past five years, and also to my committee, Professor Guozhong Cao, Professor Nicholas S. Boechler, and Professor Stuart B. Adler for their advice and time in reading and evaluating my dissertation.

I would also like to thank all the members of the multifunctional materials lab for their help in my research. Without their support and companion, I would not be able to complete my work.

Also, I would like to thank all the collaborators for not only generously providing me samples but also kindly spending time teaching me, in particular, Tim Geary, Jinjin Zhao, Evan Uchaker, Stephanie Candelaria and Rong Wu.

Last but not least, I would like to thank my dearest family and friends for their mental and emotional support over the years.

Chapter 1. INTRODUCTION

1.1 Motivation

The development of new types of energy sources has become more and more important due to the fact that global energy consumption is increasing rapidly. It is estimated that the world demand for energy will double by 2050 [1]. Toward this end, both energy conversion technology (such as solar cells and fuel cells) and energy storage technology (such as supercapacitors and batteries) have been extensively studied. Particularly, lithium ion battery, which was first commercialized by Panasonic in 1991, has achieved huge success in the market as one of the dominating energy storage systems. However, in consumer electronics such as cell phones and laptops where lithium ion batteries are used as power supplies, batteries are often considered as the heaviest, most bulky, and least environmentally friendly component. In order to reduce the weight, volume and cost of consumer electronics, increasing the energy and power density while reducing the cost of batteries has become extremely important. On the other hand, in those new-released electric vehicles and hybrid electric vehicles where lithium ion batteries are designed to replace gasolines as the power source, increasing the energy and power density while improving the performance at higher surge current is even more crucial. Besides, potential safety hazard is always a significant concern.

In order to fulfill the requirements for the wide variety of applications, lots of different strategies have been proposed. One straightforward solution is to improve the current state-of-art lithium ion battery, making it more feasible. Another solution is to develop much advanced battery systems based on different chemistries, such as lithium sulfur battery, sodium ion battery and magnesium ion battery.

Apparently, the first solution is more practical and thus has attracted lots of research efforts. Many researchers have tried to "push the limit" by nanostructuring and nanoarchitecturing. One major route is to make modifications on graphite and lithium cobalt oxide, which are currently used in commercial lithium ion batteries. Large improvement of battery performance has achieved by synthesizing nanostructured carbon [2] which can provide shorter diffusion path and thus accommodate higher current rate and provide higher power density, and by doping additional transition metal into the layered $LiCoO_2$ structure [3]. The other route is to synthesize new suitable materials for both anodes and cathodes. Nanostructured silicon [4], tin [5], transition metal oxides [6], and composites [7] have been explored as promising next generation anode materials, which in general exhibits much higher specific capacity than graphite. While for the cathode materials, high voltage (> 4V) oxides with different crystal structures such as olivine $LiFePO_4$ [8] and spinel $LiMn_2O_4$ [9] have been synthesized and studied. In general, the overall performance of nanostructured materials is better than bulk materials, benefiting from the surface effects. With nanostructuring, the volume expansion/contraction and the resulted mechanical stress can be better accommodated, and thus the stability can be improved. Besides, with reduced diffusion path length and much higher surface area exposed for both electrons and ions, faster transport can be realized, therefore, faster charging and discharging can eventually be realized.

In the first part of my dissertation, I mainly focus on developing nanostructured carbons to improve the performance as anode of lithium ion battery, which will be discussed in details in Chapter 2 and 3. I tried to introduce micropores and mesopores to the nanocarbons and studied the correlation between the overall battery performance and the porous structure, and also tried to improve the battery performance by creating patterned structure on the carbon films.

In addition to the efforts put in synthesizing nanostructured carbon materials with improved electrochemical performance, I also spent lots of time in combining various scanning probe microscopy techniques, to study in depth different nanostructured electrochemical materials, motivated by the lack of a complete understanding of the material properties on the nanoscale. It is well known that a complete set of material structure and property characterization can facilitate the design of appropriate material structure for certain application. For example, the invention of in-situ transmission electron microscopy [10] enables direct observation of the morphology evolution of silicon anode during lithiation and de-lithitation process. On the other hand, the recently developed electrochemical strain microscopy [11-13] allows the probe of localized ionic transport in different electrochemical materials, such as lithium ion transport in lithium ion battery electrode materials. Development of advanced material characterization techniques has improved the community's fundamental understanding of the materials and corresponding performance. Among various characterization techniques, scanning probe microscopy draws our attention. It is a versatile technique that uses a tiny tip which comes in contact with the sample in order to image the sample surface morphology and also to probe the sample-tip interactions under different stimuli such as temperature variation and external electric field. When applying different stimuli, different material properties can be investigated, rendering different functional modules of scanning probe microscopy, such as conductive atomic force microscopy, piezoresponse force microscopy and the electrochemical strain microscopy. If different modules can be combined for characterization, it would provide a more comprehensive understanding, which motivates my research covered in the second part of my dissertation. I mainly focused on using piezoresponse force microscopy combined with Kelvin-probe force microscopy to systematically characterize organic-inorganic perovskites used as light absorber

layer in solar cells, trying to address some confusion regarding its ferroelectric property and the interplay between ferroelectricity and light illumination. Last but not least, I have also explored the resistive switching behavior of the bio-ferroelectric materials using piezoresponse force microscopy together with conductive atomic force microscopy.

1.2 Energy Storage Systems

1.2.1 *Lithium Ion Batteries*

Rechargeable lithium ion batteries have become the dominant power source for portable electronics like cell phones, laptops, etc, due to their high energy density compared to other conventional rechargeable batteries [14]. The motivation for developing Li metal chemistry based battery is that Li is most electropositive as well as the lightest metal, thus facilitating the design of high energy density energy storage system. After the discovery of the best intercalation compound TiS_2 at that time, the first lithium battery was made in 1976 with Li metal as anode, TiS_2 as cathode and lithium perchlorate in dioxolane as electrolyte [15]. However, safety issues soon arised from the use of Li metal as anode, mainly due to the dendritic lithium growth during subsequent cycles and the potential short circuiting hazards. Later on, researchers have come up with the concept of "rocking-chair" lithium ion battery in the early 1990s and achieved huge success since then. A simplified schematic of this concept is shown in figure 1.1, in which two intercalation compounds are used as cathode and anode, successfully avoiding the formation of lithium dendrite that occurs when using lithium metal. The most commonly used electrode materials are graphite as anode and lithium cobalt oxide ($LiCoO_2$) as cathode, both of which have layered structures. Besides, an electrically insulating and ionic conducting porous polymer membrane is used as separator. Electrolytes employed in the system are typically lithium salts

such as lithium perchlorate and lithium hexafluorophosphate dissolved in carbonates solvents, for example propylene carbonate and mixture of ethylene carbonate and dimethyl carbonate.

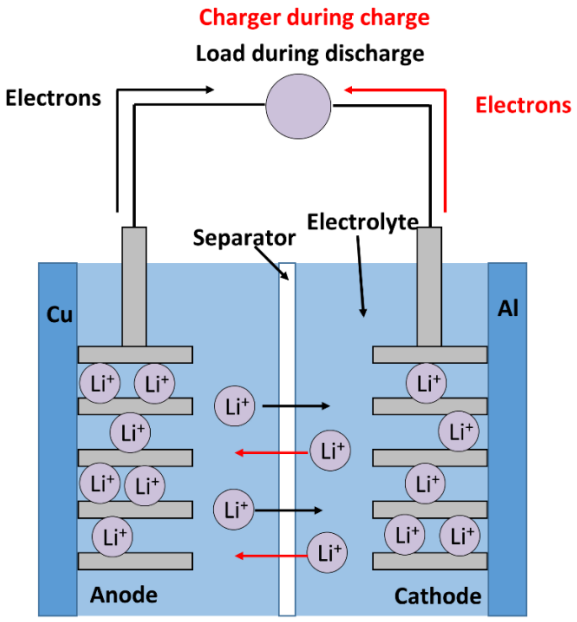

Figure 1.1 Schematic of rechargeable lithium ion battery

Upon charging of a lithium ion battery, lithium ions are first extracted from the cathode, then diffuse through the separator to the anode side and then are inserted into the anode, while electrons flow through the external circuit. Upon discharging, lithium ions reverse the motion, flowing from anode to cathode. The amount of lithium ions that can be reversibly inserted into and extracted out of the electrode determines one of the key parameters—specific capacity C of the electrode. The specific capacity C can be calculated using equation (1.1) below, where Q is the total amount of charge that can be stored and m is the weight of the electrode.

$$C = \frac{Q}{m} = \frac{I*t}{m} \quad (1.1)$$

Another important parameter is the energy density, which is an integration of voltage with the specific capacity. Voltage of the cell is calculated by subtracting the potential of the anode

from that of the cathode. In general, cathode with higher potential and anode with lower potential is preferred, to increase the total energy density.

1.2.2 *Carbon Anodes*

To meet the rapidly increasing requirements of batteries, lots of efforts have been made to improve the battery overall performance including specific capacity, lifetime, energy density and power density, by either synthesizing new material compositions or designing new structures [14, 16]. On the anode side, graphite is the current standard material in commercialized lithium cells thanks to its structural and chemical stability and thus long lifetime. Graphite is a two-dimensional layered structure composed of planar hexagons of sp^2 hybridized carbon bonds. The planes (or graphene sheets) are weakly bonded together by van der Waals forces into an ABAB… stacking sequence along the c-axis, as drawn in figure 1.2 [17]. Each carbon atom is bonded to three adjacent carbon atoms, leaving one free electron, thus forms the delocalized π electron cloud of each graphene layer, which contributes to the good electrical conductivity of graphite. Benefiting from its layered structure, lithium ions can intercalate in between the graphene sheets easily and form LiC_6. This LiC_6 stoichiometry allows a theoretical capacity of 372 mAh/g of graphite.

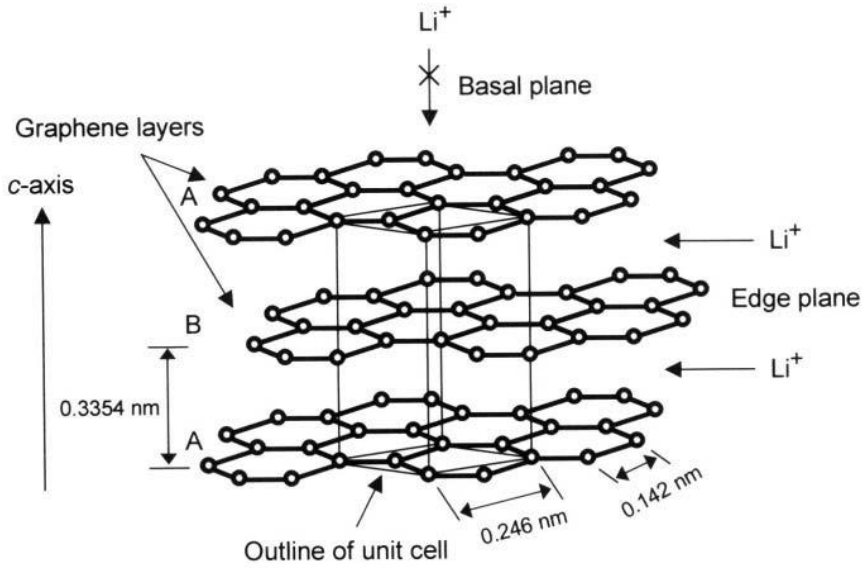

Figure 1.2 Crystal structure of graphite showing the ABAB… stacking sequence

After applying graphite as a well-behaved lithium ion host, various kinds of carbonaceous materials upon heat treated at low temperatures (< 1500 ˚C) are also tested as anodes. Those carbons have lower crystallinity and more structure disorder, referred to as disordered carbon. The carbon atoms are still arranged in a planar hexagonal network with sp^2 bonding, similar to graphite, but the size and orientation of those planar crystallites can vary a lot, and thus inducing defects and structure disorder. The structure disorder leads to different lithium ion storage mechanisms proposed by different researchers, as shown in figure 1.3. Compared to the graphite storage mechanism [18] shown in figure 1.3(a), Sato [19] proposed that lithium ions can be stored in the form of Li2 covalent molecules, as shown in 1.3(b). Also, the nanopores can function as lithium ion reservoirs [20], as plotted in 1.3(c), moreover, Dahn [21] proposed that lithium ion can be adsorbed on both sides of the graphene layer, as schematically shown in 1.3(d). As a result, they show a higher capability of reversible lithium ion storage than graphite, with capacities ranging between 400 and 2000 mAh/g depending on the carbon precursor and also the heat treatment process.

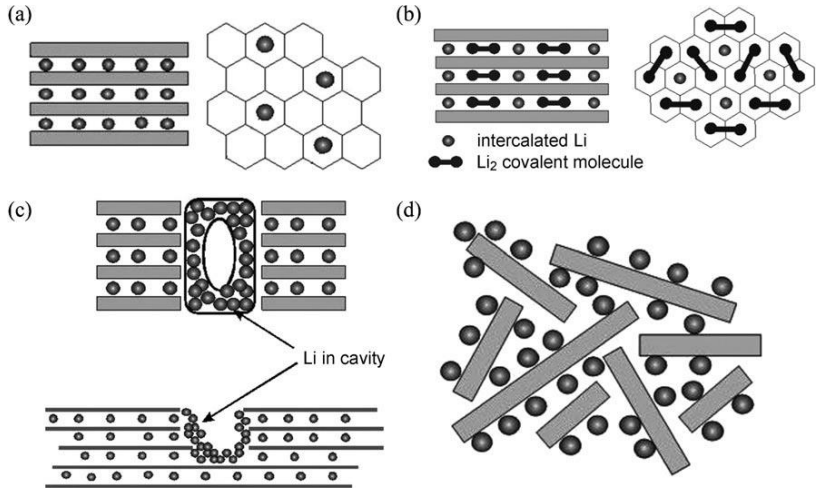

Figure 1.3 Different lithium ion storage mechanisms in carbon materials

Later on, the unique characteristics of nanostructured electrodes make them promising candidates for the next generation battery design. The advantages include increased electrochemically active surface areas for charge transfer and reduction of electronic and ionic transport resistance due to the smaller diffusion lengths. Therefore, lots of different nanostructured carbon such as carbon nanotube and graphene, have been explored and successfully demonstrated superior performance [2, 22]. And here, we tried different synthesis route to fabricate nanostructured carbon materials, and tried to improve the capacity performance.

1.3 Energy Conversion Systems

While energy storage remains an issue, energy shortage is another critical issue, due to the exhaustion of fossil fuel sources. With the sun being the most plentiful energy source for the earth, researchers have been trying to produce electricity from the solar radiation. The discovery of photovoltaic effect by Becquerel [23] in 1839 and the commercialization of the very first photovoltaic cell in the early 1950s has opened new perspectives on the photovoltaic technology development based on solar energy. Since then, the photovoltaic system undergoes rapid development, and emerging technologies with higher conversion efficiencies such as Si solar cell,

dye sensitized solar cell (DSSC) and organic solar cell (OSC) have been commercialized. Over the past few decades, lots of progress has been made in the improvement of the conversion efficiencies of all those technologies. However, quite some problems still need to be addressed before solar cells can be used as dominant energy conversion system, for example, how to maintain the high efficiency while reducing the cost and eliminating the use of toxic materials like gallium arsenide (GaAs). Towards this end, researchers have been on the hunt for better materials as the light harvester in solar cells, and recently the discovery of inorganic-organic hybrid lead halide perovskites [24] has attracted significant attention as light absorbers, which has motivated the development of low-cost and high-efficiency perovskite solar cell through a solution process.

1.3.1 *Perovskite Solar Cells*

The inorganic-organic hybrid perovskite solar cell research started back in 2009 [24] with an initial efficiency of 3.8%. Through the past seven years' effort, the photovoltaic conversion efficiency has reached over 22% [25] and the stability is relatively good. This efficiency approaches the highest efficiency of thin film solar cell based on $Cu(In,Ga)Se_2$ and exceeds that of both conventional organic solar cells and dye-sensitized solar cells [26]. Aside from the high efficiency and good stability, another major advantage associated with the perovskite solar cell is that the device is fabricated through low cost solution processing.

The schematic of the perovskite solar cell is shown below in figure 1.4. In general, it consists of both top and bottom electrode as current collector, and then another two layers for electron and hole transport, and sandwiched in between is the perovskite layer as light absorber. Typically, titanium dioxide (TiO2) is used as electron conducting layer and poly(3,4-ethylenedioxythiophene): poly(p-styrene sulfonate) (PEDOT:PSS) is used as hole conducting

layer. The device can be fabricated with a n-i-p or p-i-n structure, depending on whether the electron transport layer is in front of the incident light or not.

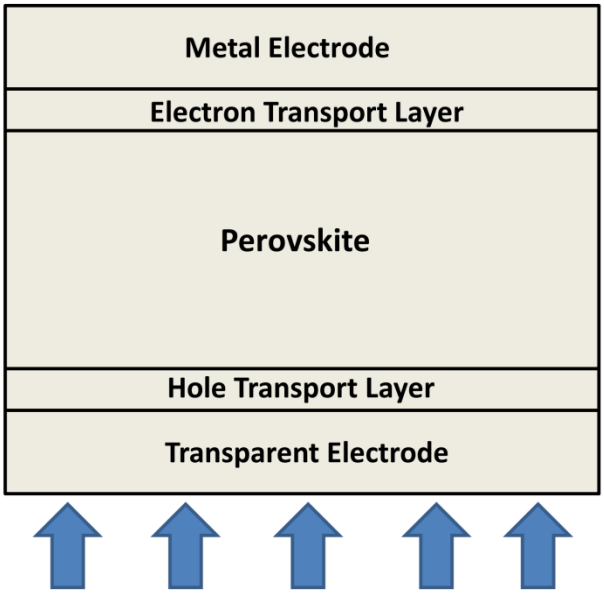

Figure 1.4 Schematic of a perovskite solar cell

As mentioned above, the organic halide perovskites are used as light absorbers in the cell, which have the crystal structure of ABX_3, where, A refers to organic cation (most often methylammonium CH_3NH_3), B refers to metal cation (typically Pb), and X refers to halide anion (usually I or Cl, Br). The band gap of this family of organic halide perovskites can be well tuned from absorbing ultraviolet to infrared region by composition engineering [27-30]. In addition to the tunable band structure, the high electron and hole mobility, large absorption coefficients (10^4 – 10^5 cm^{-1}), low exciton binding energy (< 50 meV), and long charge-carrier diffusion length (~175 μm) also favor the application as light absorber in solar cells [31, 32]. However, to better understand the underlying mechanism and design better devices, there are still some critical problems remaining to be solved, for example, the current-voltage (J-V) hysteresis [33, 34] and the device performance degradation [35, 36]. Among those problems and question marks, the one that attracted our attention is the intrinsic ferroelectric property of organic halide perovskites.

1.3.2 *Ferroelectricity*

It is well known that a number of inorganic perovskite materials such as $PbTiO_3$ and $PbZrO_3$ are well-behaved ferroelectrics [37]. Similarly, organic halide perovskites such as $CH_3NH_3PbX_3$ (X=I, Cl, Br) should also behave like ferroelectrics. At room temperature, the $CH_3NH_3PbX_3$ prepared with solution processing is typically in tetragonal phase, as shown below in figure 1.5 [38], which results in asymmetric crystal structure. With such structure, both CH_3NH_3 ion and Pb ion shows off-center motion, intrinsic polarization will be induced, suggesting its ferroelectric nature [38].

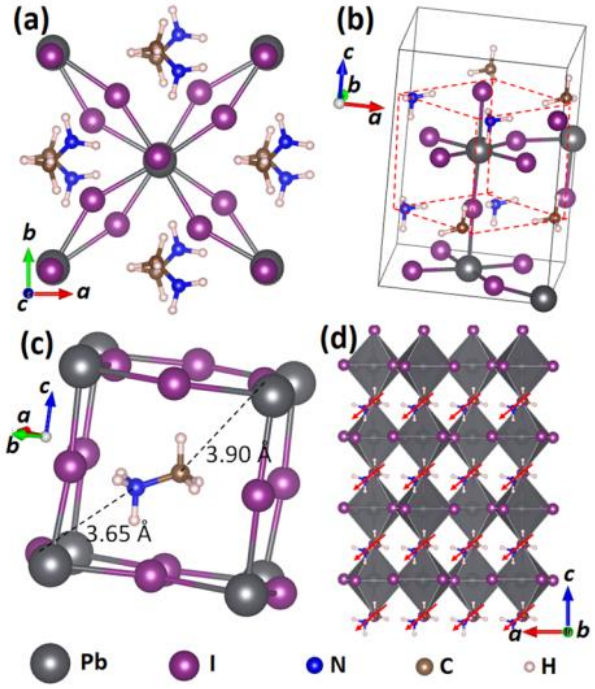

Figure 1.5 Tetragonal phase of $CH_3NH_3PbI_3$

However, there are some controversial arguments around the intrinsic ferroelectric properties of the halide perovskites, both experimentally [39, 40] and theoretically [41, 42]. Macroscopic ferroelectric measurement [40, 43] yielded giant apparent polarization that is largely contributed by leakage and ionic current, which complicated the understanding and interpretation of the data.

At microscopic level, some literature results reveal well defined ferroelectric domains [39, 44, 45], while some leading experts in this field reported neither ferroelectric domain nor polarization switching behavior [46]. Furthermore, some researchers argue that the undesired current-voltage hysteresis is due to the ferroelectricity [47, 48], while other researchers attribute the high conversion efficiency to the ferroelectric properties [41, 49], which may favor the charge separation and reduce the charge recombination. What we tried to address is to first establish strong evidence of the ferroelectricity and then study the interplay between the ferroelectric property and the light illumination.

1.4 Ferroelectrics and Resistive Switching

Ferroelectric materials have been used in a wide range of applications [50, 51], such as high-permittivity dielectrics, pyroelectric sensors, piezoelectric devices, electro-optic devices, and also energy conversion systems, due to its unique properties and superior performance. If a material has spontaneous polarization and can be reversed by external electric field, then this material is ferroelectric. The spontaneous polarization is in general temperature dependent, and thus has a critical temperature, above which the material undergo a phase transformation from ferroelectric to pyroelectric.

The very first ferroelectric material discovered is Rochelle salt ($NaKC_4H_4O_6{\cdot}4H_2O$) back in 1921. Later on, the mostly used ceramic ferroelectric barium titanate ($BaTiO_3$) was discovered and used in commercial transducers. Then, more and more ferroelectric materials, including polycrystalline ceramics [52] and polymers [53], with different material properties such as critical phase transition temperature, spontaneous polarization and piezoelectric coefficient have been discovered and commercialized.

In addition to the conventional applications associated with ferroelectric materials such as capacitor, sensor and actuators, there is also emerging application of ferroelectric thin films resulting from the newly discovered switchable diode behavior [54]. Back in 2009, Choi et al. [54] reported that the polarized $BiFeO_3$ (BFO) crystals show diode like rectifying characteristics, and the direction of the diode can be switched by polarization reversal. The switchable diode behavior of ferroelectric material is also categorized as ferroelectric resistive switching, which is strongly associated with the polarization switching of ferroelectrics. In contrast, another type of resistive switching behavior is more commonly observed is non-ferroelectric transition oxides [55] such as TiO_2, which is closely related to the redox reaction and the conductive filament formation due to the ion migration. The resistive switching behavior found in both materials have attracted lots of research attention for its application in non-volatile memory devices (NVM), also referring to as resistive random access memories (RRAMs) [56, 57]. In order to achieve robust application, the resistive switching behavior and the underlying mechanism of how the ferroelectric polarization couples with the resistive switching becomes more and more important, and researchers have come up with extensive characterization method using for example atomic force microscopy.

1.5 Atomic Force Microscopy

1.5.1 *Overview*

Atomic force microscopy (AFM), invented by Binnig et al. in the 1980s [58], belongs to a series of scanning probe microscopes (SPM). With the tip coming in physical contact with the material, AFM allows imaging of the surface topography, in some cases with atomic resolution. The capability of imaging all materials no matter hard or soft, synthetic or natural, has made AFM attractive as a characterization tool. Therefore, AFM has experienced significant

development, inducing more functionalities such as force measurement [59] which can provide valuable information on material mechanical properties like elasticity and hardness.

Various techniques based on atomic force microscopy have also been developed to provide more insights of the material properties. They can be divided into two categories according to the tip-material interaction. The first one is non-contact dynamic AFM [60] including electrostatic force microscopy (EFM) [61], Kelvin probe force microscopy (KPFM) [62] and magnetic force microscopy (MFM) [63]. And the other is contact mode AFM including conductive-AFM (c-AFM) [64], piezoresponse force microscopy (PFM) [65] and electrochemical strain microscopy (ESM) [11, 12]. With the rapid development of new techniques, AFM has become an extremely powerful characterization tool of multifunctional materials.

1.5.2 *Kelvin Probe Force Microscopy*

As mentioned above, KPFM is a non-contact dynamic AFM technique, which was first introduced by Nonnenmacher et al back in 1991 [62]. Unlike scanning tunneling potentiometry, which is limited to measurement on metallic surfaces, KPFM enables the imaging of surface potential of a broad range of materials by measuring the local contact potential difference between a conductive AFM tip and the sample based on electrostatic interactions [66, 67]. It is one of the best tools to image the surface potential distributions with sub-nanometer resolution [66]. When the AFM tip is brought close to the sample surface, electrons will flow from one surface to another driven by the difference in the Fermi energy levels, until equilibrium is established. Along with the electron flow, some net surface charge will build up on the surfaces of the tip and the sample, which will in turn generate the contact potential difference (CPD), as illustrated in the schematic below [66]. The CPD is a highly material-dependent parameter and directly related to the work function of the materials. This potential difference between the AFM

tip and sample surface causes electrostatic force interactions, which will vibrate the AFM tip. During the KPFM scanning, the external direct-current (DC) voltage is adjusted such that the electrostatic force between the tip and the sample becomes zero and thus the tip vibration becomes minimized. Using such a feedback loop control, the surface potential of the sample can be mapped out by measuring these external DC voltages.

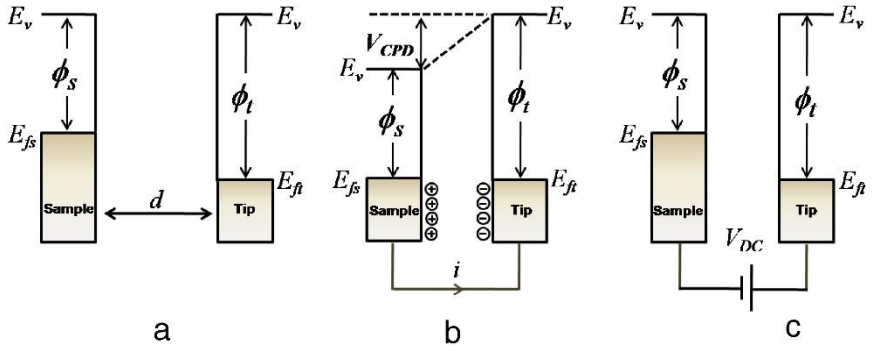

Figure 1.6 Schematic of the Fermi energy level of the AFM tip and the sample surface

Over the past decade, the instrumentation of KPFM has been greatly improved for a higher spatial resolution and good repeatability. Researchers have used KPFM to study a wide range of materials, including semiconductors [68] and metallic nanostructure catalysts [69], and also devices such as solar cells [70, 71].

1.5.3 *Piezoresponse Force Microscopy*

PFM is a powerful tool to probe the piezoelectric and ferroelectric properties of materials at the nanoscale, which was first developed and used to observe the domain structure in ferroelectrics by Franke in 1994 [72]. PFM is a strain based probe technique, as illustrated in figure 1.7 below. During the PFM operation, a conductive tip scans over the sample surface in contact mode, applying a localized electric field to excite the piezoresponse. The localized electric field causes a displacement on the sample surface which in turn leads to the bending of the cantilever accordingly. Once the cantilever is bent to certain degree, the reflection pass of the

laser that shines on top of the cantilever will change, which can be measured and recorded by the photodiode. However, with some materials that intrinsically shows a relatively small response, it becomes extremely difficult to separate the signal from the inherent noise in the system or environment noise. Measurements of such materials will require the use of higher voltages, which becomes undesirable for some materials due to the potential damage to the sample. In order to non-destructively magnify the response, the alternating current (AC) voltage is applied at or close to the resonant frequency of the tip-sample interaction so that the signal to noise ratio can be greatly enhanced. Plotted below in the solid dots in figure 1.8 is the measured strain response amplitude and phase with respect to the frequency of the AC voltage applied to the AFM tip. It is clearly seen that near the tip-sample resonance frequency, the response amplitude gets enhanced a lot and the phase response changes by 180˚ as well. And the black lines are the fitted results based on the damped driven harmonic oscillator model, as illustrated in figure 1.9 [73, 74], showing a good fit. By fitting this model, the intrinsic surface deflection amplitude and phase response can be extracted using equations (1.2) and (1.3).

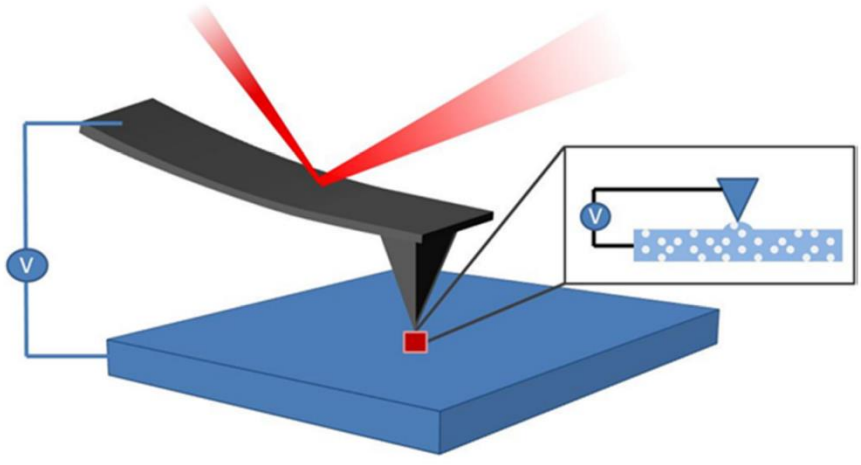

Figure 1.7 Schematic illustration of strain based SPM, for example, PFM

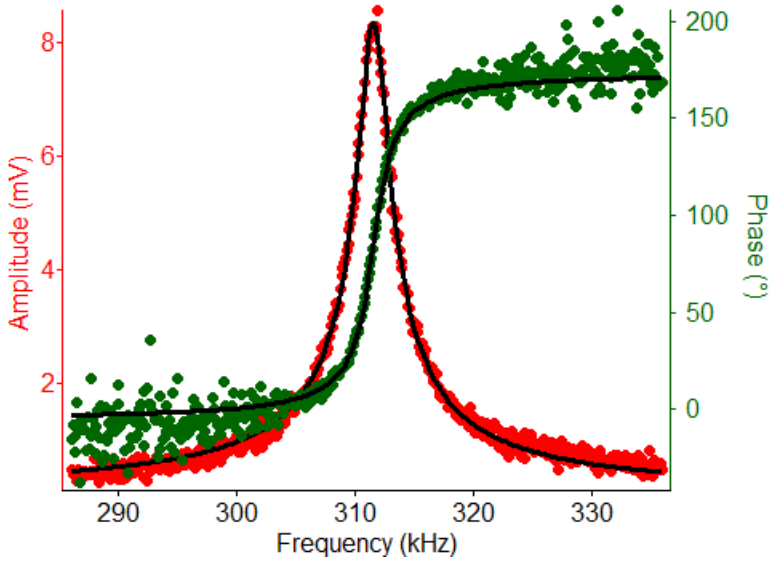

Figure 1.8 Example of how contact resonance enhancement works

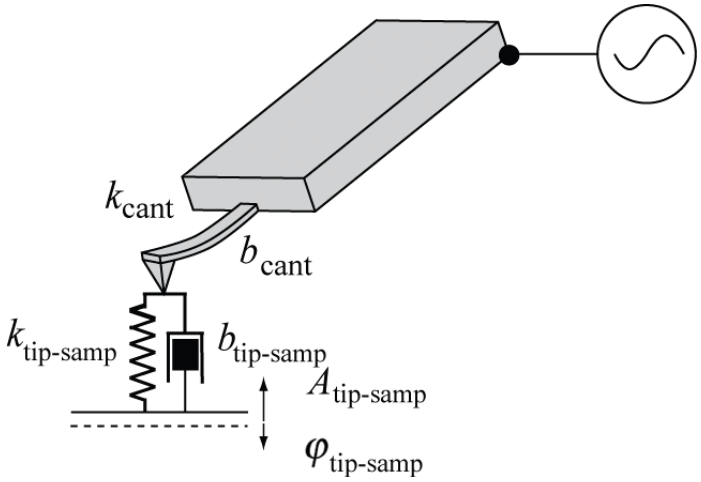

Figure 1.9 Schematic of the damped driven harmonic oscillator model

$$A(\omega) = \frac{A_{drive}\omega_0^2}{\sqrt{(\omega_0^2 - \omega^2)^2 + (\omega\omega_0/Q)^2}} \quad (1.2)$$

$$\varphi(\omega) = tan^{-1}\left(\frac{\omega_0\omega}{Q(\omega_0^2 - \omega^2)}\right) + \varphi_{drive} \quad (1.3)$$

In the above governing equations, ω_0 is the resonance frequency, Q is the quality factor, and A_{drive} and φ_{drive} corresponds to the intrinsic surface deflection amplitude and phase, which can all be quantified by doing the model fitting. With such method, in theory we can map out not

only the intrinsic piezoresponse under an external AC voltage excitation, but also the domain orientation of a ferroelectric material, in which 180˚ phase contrast is expected for domains with opposite orientations. To better characterize the piezoelectric and ferroelectric properties at the nanoscale, some novel techniques based on PFM have been developed, including dual amplitude resonance tracking PFM[75] (DART-PFM), switching spectroscopy PFM[76] (SSPFM), band excitation PFM[77] (BE-PFM), and I will be using some of those in my later work.

1.5.4 *Electrochemical Strain Microscopy*

ESM is a relatively new technique for studying the nanoscale electrochemistry of energy storage and conversion systems mentioned above. ESM was first developed by Sergei Kalinin at Oak Ridge National Laboratory a few years ago [11, 12], and the underlying mechanism is quite similar to the more well-established and better-understood PFM, which is discussed in previous session. Application wise, since ESM is capable of detecting strains or displacement on the order of picometers, it is capable of studying a wide range of electrochemical systems such as lithium ion battery electrodes [78] and solid oxide fuel cell electrolytes [79].

However, unlike the well understood behaviors of piezoelectric and ferroelectric materials studied with PFM, the electrochemical processes and the resulted responses measured with ESM can be rather complicated due to multiple factors contributing [80-82], such as electrostatic interactions, and induced dipoles, causing the data interpretation quite difficult and challenging.

1.5.5 *Conductive Atomic Force Microscopy*

CAFM measures the electrical properties of the material by passing a voltage across the sample and measure the current flow between the conductive AFM tip and the sample. The advantage of CAFM is that both collecting a current and topography map of a sample surface at

a fixed DC voltage bias and measuring the current-voltage characteristics at specific locations by sweeping the voltage can be realized. Also, instead of applying a voltage to the tip in PFM and ESM, here the DC voltages are applied directly to the sample surface and the tip is virtually grounded, which is connected to a current amplifier for measurement. Figure 1.10 below shows a simplified illustration of how the current flow is measured using a resistor R and a current amplifier.

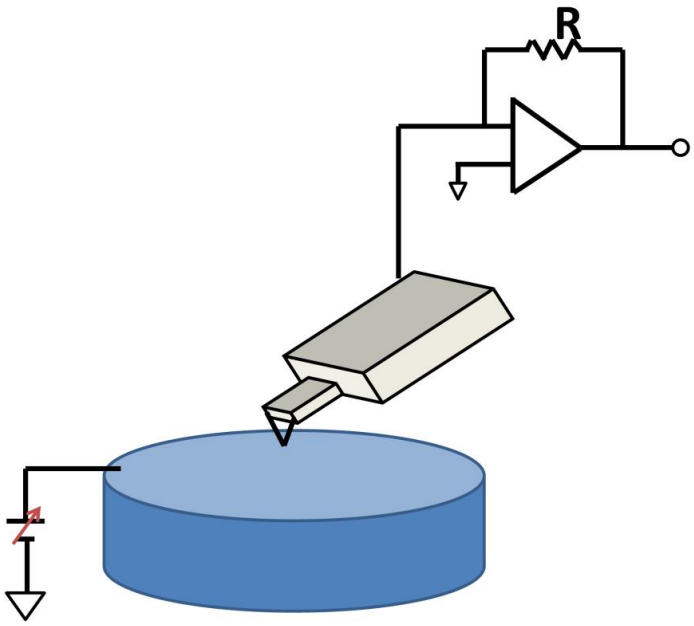

Figure 1.10 Schematic of how CAFM works

As a powerful current sensing technique for electrical characterization of conductivity variations in resistive samples, CAFM has been mostly used on including thin dielectric films [83], ferroelectric films [84], nanotubes [85], conductive polymers [86], and others.

1.6 Dissertation Overview

This dissertation covers research performed over the past five years in both synthesizing and characterization of nanostructured electrochemical materials. Chapter 2 talks about the synthesis

of carbon nanofibers through electrospinning and post annealing steps, characterization of electrochemical performance as lithium ion battery anode, and also further process optimization to achieve better performance. Chapter 3 continues with nanostructured carbon films synthesis for lithium ion battery application using nanoimprint lithography. Chapter 4 and 5 covers the characterization aspect using scanning probe microscopy, with chapter 4 focusing on studying $CH_3NH_3PbI_3$ for solar cell application and chapter 5 focusing on studying the switchable diode behavior of the bio-ferroelectric elastin and tropo-elastin. Finally, Chapter 6 will summarize the research covered in this dissertation and present some ideas for future work.

Chapter 2. CARBON NANOFIBER ELECTROSPUN FROM POLYVINYLPYRROLIDONE FOR LITHIUM ION BATTERIES

2.1 Motivation

Lithium ion battery has become one of the most important energy storage devices since its first commercialization in 1991. Thanks to the high energy density[87], lithium ion batteries have been widely used in small portable electronic devices and extended to large scale applications such as electric and hybrid electric vehicles[1, 88]. With the rapid increasing demand for energy, researchers have been focused on developing alternative electrode materials to achieve higher energy and power densities, better rate performance and longer lifetime[1, 2, 89-92].

The success of graphite as the most commonly commercialized lithium ion battery anode has driven researchers' attention in exploring different carbon structures, trying to overcome the disadvantages of graphite such as low specific theoretical capacity (372 mAh/g) and limited rate capability. To improve the current state of art graphite anode, various nanostructured carbon materials have been studied, including carbon nanotubes[93], nanofibers[94], nanofoams[95], graphene[96] and their composites[97, 98]. In particular, porous carbon nanofiber stands out, for the reason that not only the one dimensional nanostructure shortens the diffusion length for lithium ions but also the porous structure offers large electrode/electrolyte interface for charge-transfer reaction to happen[99]. Besides, the typical synthesis method is electrospinning, which is one of the simplest and most effective technologies to produce nanomaterials in a cost effective fashion.

In this work, solution-based electrospinning combined with thermal treatment is adopted to produce porous carbon nanofibers. Post activation process is also carried out to further improve the porous structure. Polyvinylpyrrolidone (PVP) instead of polyacrylonitrile (PAN) is chosen to be the carbon precursor. Even though PAN is the most commonly used carbon precursor for electrospinning due to its high melting point and large carbon yield [100, 101], it has the disadvantage of low solubility and compatibility with many organic solvents and also relatively high cost. While in contrast, PVP is easily dissolved in ethanol, water and many other solvents, low cost and environmentally-friendly as well.

2.2 Principles of Electrospinning

Electrospinning, or electrostatic spinning is a versatile method that allows the fabrication of continuous fibers with diameters ranging from a few nanometers to micrometers [102-105]. This technique can be applied to a wide variety of materials, including polymers, ceramics and composites, also fibers with complex structures, such as core-shell fibers [106, 107] and hollow fibers [108, 109] can be fabricated. In recent years, electrospinning has been increasingly used in the field of sensors [110], energy storage devices [94, 111], filtration [112] and tissue engineering [113, 114]. The basic setup consists of three major parts: a grounded collector, a spinneret with metallic needle and a high voltage power supply, as shown in figure 2.1. A polymer solution or melt is loaded into a syringe first and then can be fed through at a constant rate controlled by the syringe pump. With a high voltage applied, the solution experiences two types of electrostatic forces: the electrostatic repulsion between the surface charges and the Coulombic force induced by the external voltage, which together distort the solution into a conical object, known as the Taylor cone. When the applied electric field overcomes the surface tension of the solution, the ejection of a liquid jet forms and undergoes a stretching and whipping

process. The liquid jet is then continuously elongated and thinned until deposited on the grounded collector.

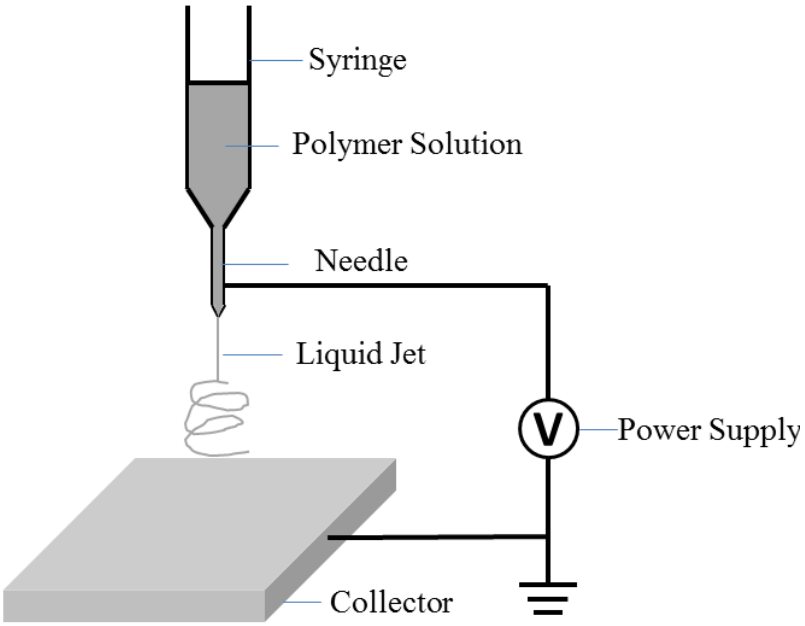

Figure 2.1 Schematic of electrospinning process

It has been found that the fiber morphology and uniformity depends on many parameters, which can be divided into three main categories: solution properties, processing conditions and ambient conditions. Solution properties include viscosity, molecular weight, concentration, electrical conductivity and surface tension. For example, beads are less likely to form for more viscous solutions but fiber diameter gets larger. However, if the viscosity is too high, it becomes extremely difficult to force the solution through the needle, making the solution flow unstable. Processing conditions include the applied voltage, distance between needle tip and collector, feed rate and needle diameter. With varying voltage supply and distance, the fiber diameters can be finely tuned and the formation of spheres can be eliminated. The last category includes temperature and humidity, which plays an important role in the solvent evaporation process.

To summarize, electrospinning is a versatile and easy to scale up technique to produce fibers with tunable structures for a wide range of applications. In this research project, we employ this

technique to fabricate porous carbon nanofiber (CNF) with high surface area and study the performance of those nanofibers as lithium ion battery anode. In order to carbonize the polyvinylpyrrolidone fibers without losing the fibrous structures, structural characterization is also performed to help identify the optimal heat treatment process.

2.3 Synthesis and Characterization of Carbon Nanofiber

2.3.1 *Identifying the Heat Treatment Process*

To synthesize carbon nanofiber, we first started with preparing precursor by dissolving polyvinylpyrrolidone (PVP, M_w = 1,300,000) in ethanol to form a clear solution with a moderate viscosity. The solution was then loaded to a 5 mL syringe connected with a 22G stainless steel needle, which was then pumped out through the needle at a constant rate of 0.8 mL/h. All the samples were electrospun at a voltage of 16 kV applied at a distance of 14 cm from the needle to the collector. Scanning electron microscope (SEM) images of the as-pun fibers are shown in figure 2.2. As can be seen, long PVP nanofibers with uniform diameter around 600 nm were obtained after electrospinning.

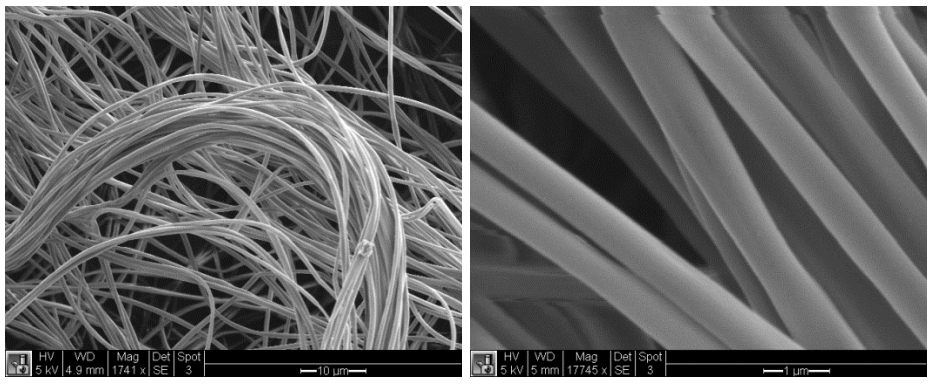

Figure 2.2 SEM images of the as-spun PVP nanofibers

The next step is to carbonize the PVP fibers while maintaining the fibrous structure. The first route we tried was the typical two-step heat treatment process for carbonizing PAN nanofibers,

including pre-oxidation at 360 °C and carbonization at 800 °C. However, the fiber morphology was completely lost, as shown in figure 2.3.

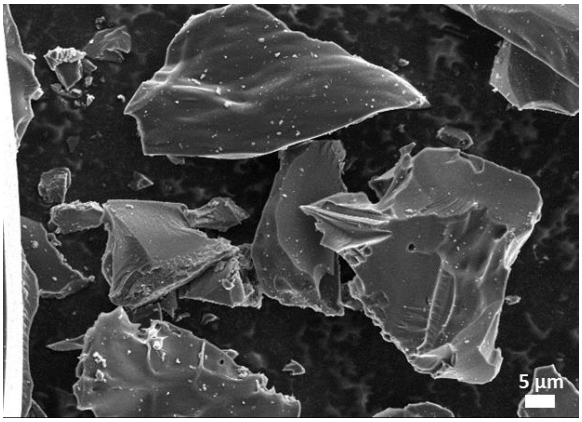

Figure 2.3 SEM image of the fibers after pre-oxidation and carbonization

In order to identify the appropriate heat treatment process, thermal analyses including Thermogravimetric Analysis (TGA) and Differential Scanning Calorimetry (DSC) were carried out. As seen from the TGA curves in figure 2.4 (A), the as-spun nanofibers lose a small amount of weight around 100 °C, and there is a corresponding large heat adsorption peak in the DSC curves as shown in figure 2.4 (B). Such weight loss and heat adsorption are believed to be caused by solvent evaporation, and in order to mitigate such effects and stabilize the fiber morphology, PVP nanofibers were first heated at 150 °C to remove all the solvents, followed by carbonization at 800 °C. This stabilization process indeed leads to nanofibers with inter-connected structure as shown in figure 2.5 (A), though these fibers appears to be flattened and quite different from those PVP fibers. Meanwhile, TGA and DSC curves of the stabilized PVP nanofibers in figure 2.4 show significant weight loss starting at 210 °C and large heat adsorption peak around 412 °C. As such, a pre-oxidization process at 360 °C was added in between stabilization and carbonization. Then, the final carbonization step was carried out at 800 °C under inert gas flow (nitrogen or argon), when oxygen, hydrogen and other foreign atoms are released as compounds such as CO_2, CO, CH_4 and also H_2 gas is released, turning the final product to a carbonaceous material.

However, some small amounts of oxygen and nitrogen still remain as impurities and the complete removal requires further heating to above 1500 °C.

We also noticed that the PVP nanofibers must be stabilized sufficiently long enough to maintain the fibrous structure. For example, if the stabilization step is only held for 6 hours followed by the same pre-oxidization and carbonization process, the structure as shown in figure 2.5 (B) was obtained, where nanofibers seem to collapse into larger fibers. In contrast, once the stabilization step at 150 °C is kept for 24 hours or longer, the resulted carbon nanofibers, as shown in figure 2.5 (C) exhibit uniform fibrous structures, as desired.

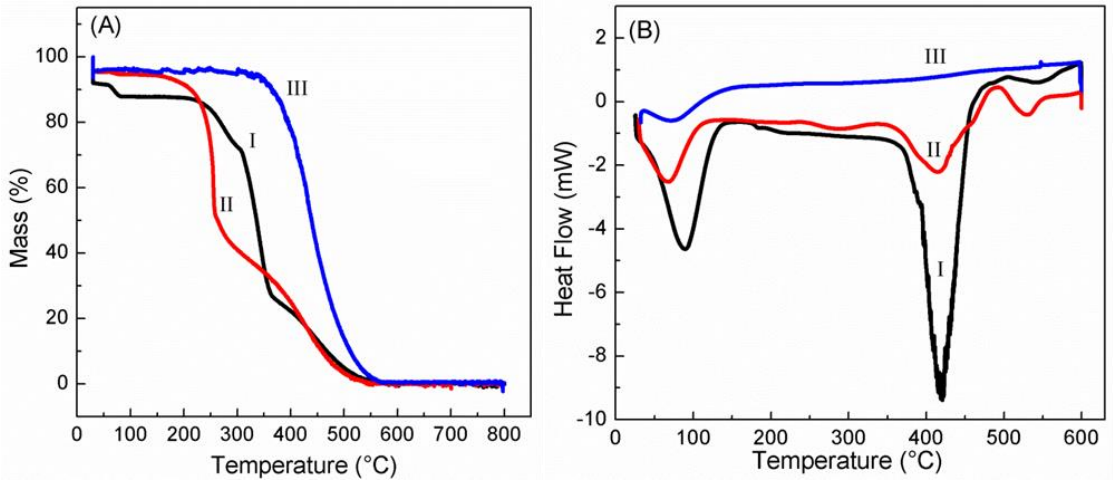

Figure 2.4 (A) TGA curves and (B) DSC curves of (I) as-spun PVP nanofibers, (II) stabilized PVP nanofibers, and (III) pre-oxidized PVP nanofibers

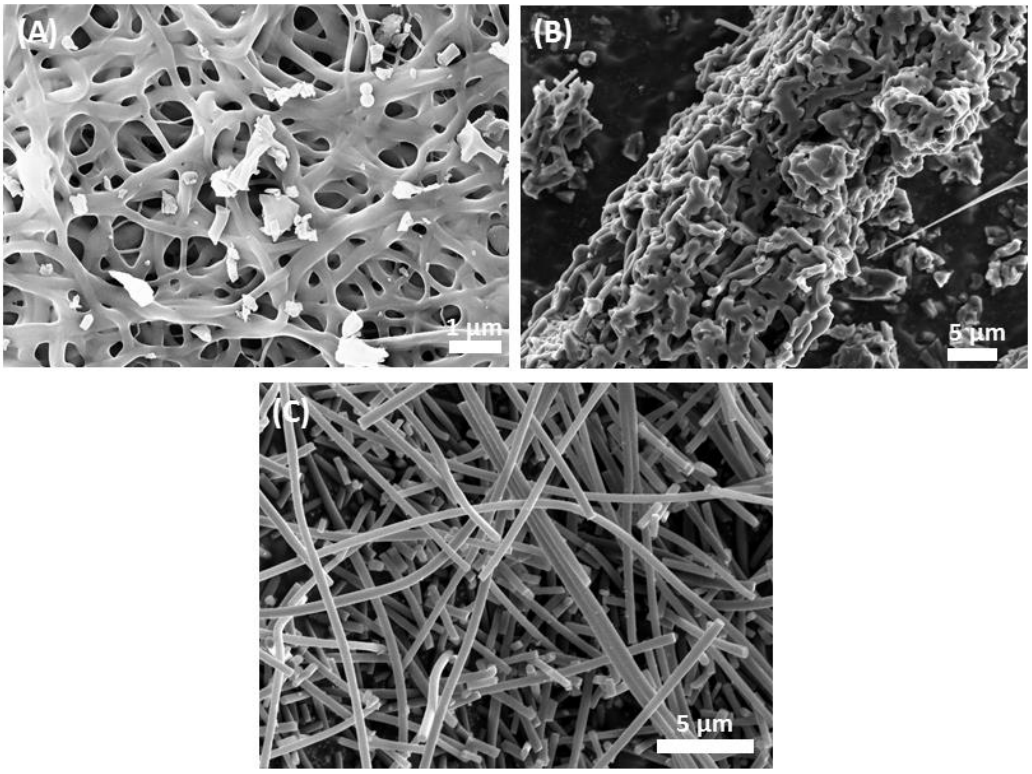

Figure 2.5 SEM images of fibers after different treatments: (A) stabilized and then carbonized; (B) stabilized for 6 hours (C) stabilized for 24 hours

In addition to TGA and DSC, Fourier Transform Infrared Spectroscopy (FTIR) was also conducted on the PVP fibers and fibers after each heat treatment step, so that the molecular structure changes could be examined. As can be seen in the spectra displayed in figure 2.6, stabilization process at 150 °C does not change the molecular structure; while significant differences can be observed when comparing the spectrum of pre-oxidized fibers with that of PVP fibers. The spectra show that the typical CH_2 stretching vibration at 2950 cm^{-1} and C-N stretching vibration at 1288 cm^{-1} disappeared after pre-oxidation, suggesting that the side chain was destroyed. And the carbon atoms on the main chain gets oxidized to form the carbon hydroxyl group (C-OH) bonding, and the hydroxyl group contributes to the broad remaining peak around 3500 cm^{-1}.

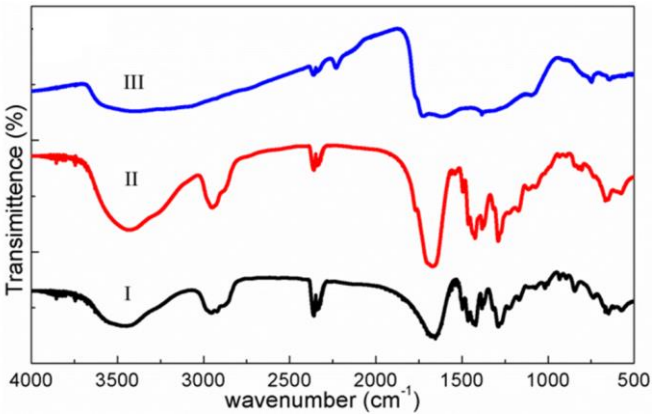

Figure 2.6 FTIR sectra of (I) as-spun PVP nanofibers, (II) stabilized PVP nanofibers, and (III) pre-oxidized PVP nanofibers

2.3.2 *Structural Characterization*

An appropriate heat treatment process thus is identified to convert the as-spun PVP nanofibers to CNFs, consisting of stabilization at 150 °C in air for 24 hours, pre-oxidization at 360 °C for 4 hours in ambient environment, and carbonization at 800 °C under nitrogen flow for 4 hours. Figure 2.7 shows the representative SEM images of the fibers after each heat treatment step. The PVP fibers and the fibers after stabilization exhibit long and uniform shape with diameters of around 600 nm. The pre-oxidized nanofibers as shown in figure 2.7 (C), on the other hand, have reduced diameters of around 500 nm, and some of the nanofibers appear to be broken into shorter fibers, suggesting substantial structure changes consistent with the FTIR spectra. After carbonization, both the diameter and the length of the fibers get further reduced, as seen in figure 2.7 (D).

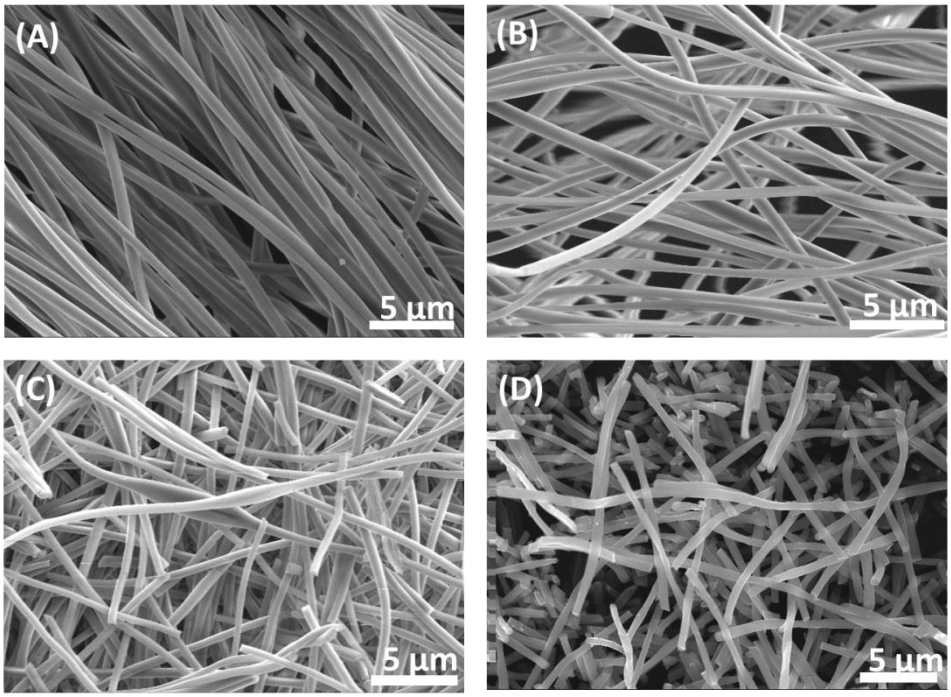

Figure 2.7 SEM images of (A) as-spun PVP nanofibers, (B) stabilized PVP nanofibers, (C) pre-oxidized PVP nanofibers, and (D) carbon nanofibers

We also took a look at those CNFs under TEM. As shown in figure 2.8 (A), the fibers are quite dense and uniform. The selected area electron diffraction (SAED) pattern in the inset shows broad diffraction rings, suggesting that the CNFs are amorphous. This is also confirmed by XRD pattern shown in figure 2.8 (B), where no obvious peak is observed at $2\theta=26°$ that would correspond to the typical (002) layer of graphite [115]. Such amorphous structure of CNFs could be due to the low carbonization temperature of 800 °C, while the typical graphitization temperature to get good crystalline graphite is around 2800 °C or higher [116].

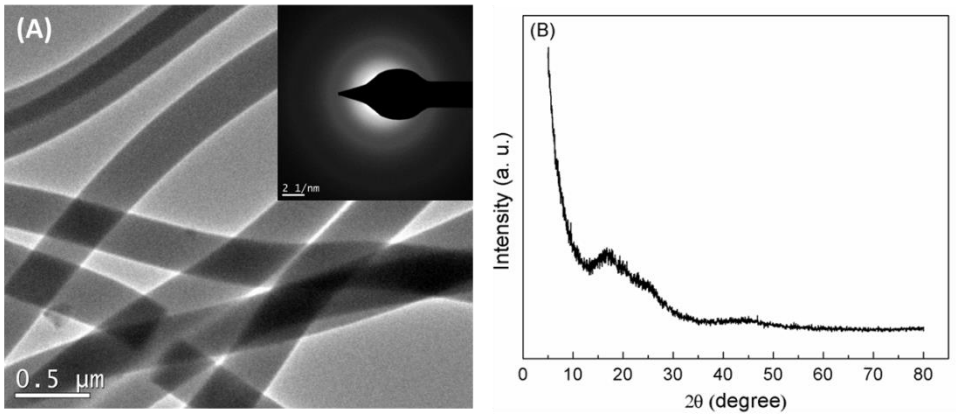

Figure 2.8 Structure of CNFs (A) TEM image of CNFs, with the inset showing the SAED pattern; and (B) XRD pattern of CNFs

2.3.3 *Optimizing the Heat Treatment Process*

With the structural characterization confirming that we have successfully synthesized carbon nanofiber, the next step is to change the heat treatment process parameters to optimize the structure. With the treatment temperature fixed, we studied the effect of different heating rates. Four combinations of fast/slow pre-oxidization and fast/slow carbonization were investigated and the porous properties were evaluated by physical adsorption of nitrogen at 77 K in a volumetric adsorption system (Quantachrome Nova 4200E). The representative nitrogen adsorption-desorption isotherm curve is displayed in figure 2.9. It does not behave like any typical isotherm among the four different types defined in the Brunauer classification [117, 118]. Instead, it's more like a combination of both type I (microporous) and type IV (mesoporous) isotherm behavior. Using the Brunauer-Emmett-Teller (BET) theory, the specific surface area, the micropore and mesopore volume, and the averaged pore size of the sample evaluated can be calculated [119]. The calculated BET specific surface areas of the four CNFs samples are summarized in table 2.1 and the corresponding SEM images are shown in figure 2.10, where CNFs with excellent morphology are observed in all the samples. Due to the different heating

rates, fiber diameters vary a lot. CNFs treated with fast pre-oxidation but slow carbonization have the largest average diameter of around 700 nm, while those treated with slow pre-oxidation and slow carbonization have smallest average diameter of around 300 nm. In addition, the nitrogen adsorption measurements suggest that the heating rate has a large influence on the porous properties of CNFs, with the fast pre-oxidization and fast carbonization process producing the largest specific surface area, as can be seen in table 2.1, while fast pre-oxidization and slow carbonization producing the second largest surface area, suggesting that fast pre-oxidization is necessary.

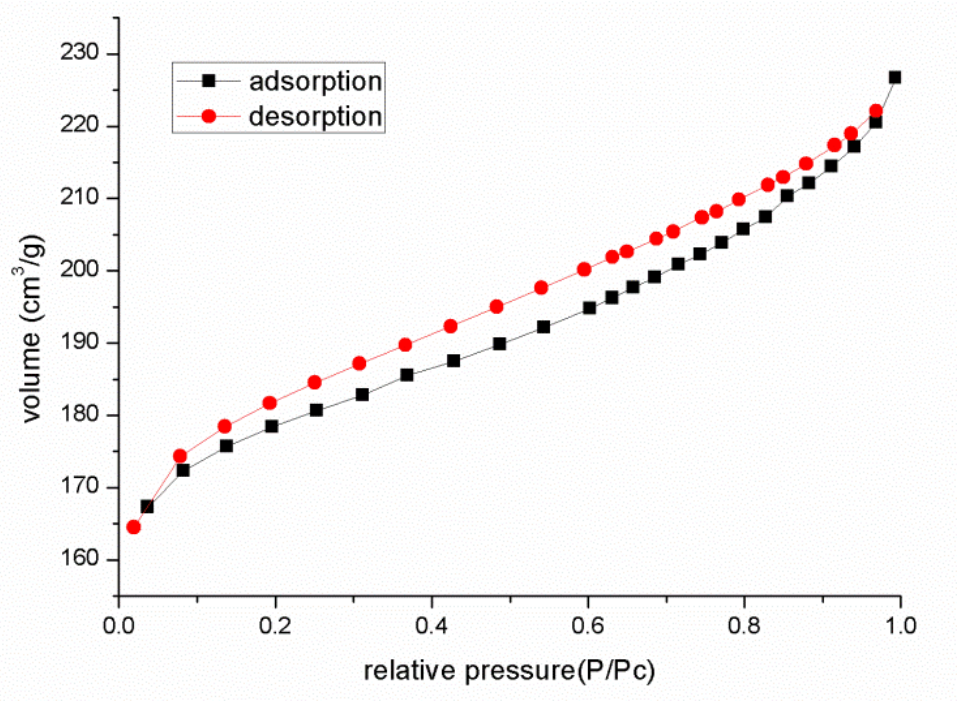

Figure 2.9 Representative nitrogen adsorption-desorption isotherm

Table 2.1 The effect of heat treatment parameters on the porous properties of CNFs

Sample	Pre-oxidation heating rate	Carbonization heating rate	BET surface area
A	60 °C/min	80 °C/min	512.4 m^2/g
B	60 °C/min	5 °C/min	267.5 m^2/g

C	1 °C/min	80 °C/min	131.2 m^2/g
D	1 °C/min	5 °C/min	63.19 m^2/g

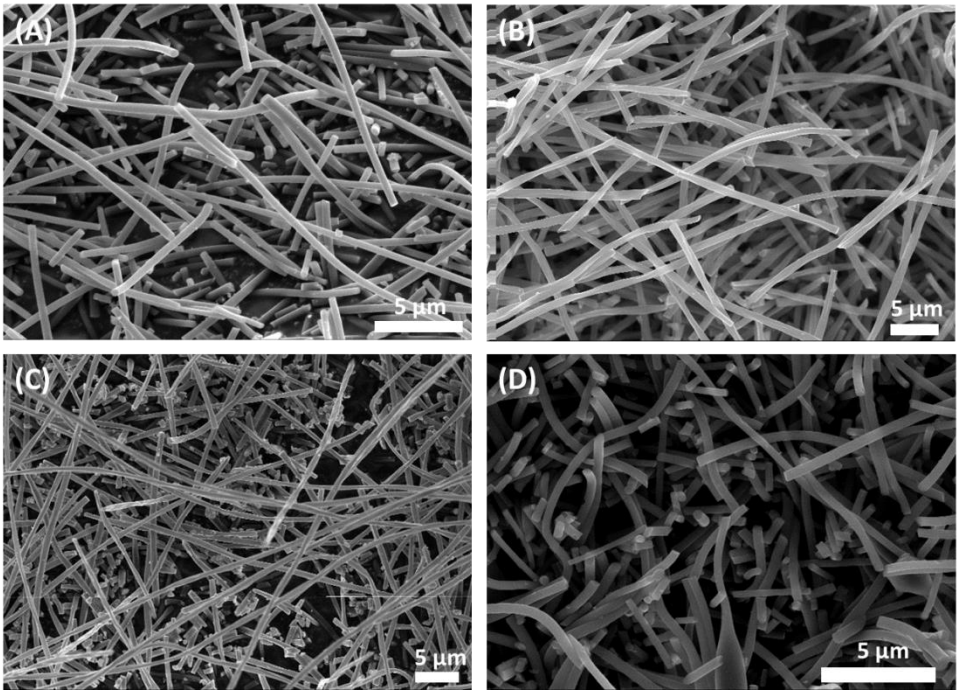

Figure 2.10 SEM images of carbon nanofibers with different heat treatment parameters as listed in table 2.1

2.3.4 *Performance of CNF as Li-ion Battery Anode*

As an example to demonstrate the potential applications of porous carbon nanofibers, the electrochemical performances of those CNFs as lithium ion battery anode were examined, described as followed.

The collected CNFs were grinded into powders and then mixed with polyvinylidene fluoride (PVDF) as binder with the weight ratio of 9:1. Then sufficient amount of n-methyl-2-pyrrolidone (NMP) was added as solvent and the mixture was grinded for another about half an hour to get homogeneous slurry with the texture similar to honey. The slurry was then spread onto a clean copper foil with doctor blade and dried at 80 °C for 12 hours to fully remove the NMP solvent.

After the overnight drying process, the carbon electrodes were punched into multiple disks and ready for the battery assembly. The coin cells are assembled in a glove box filled with argon, with lithium metal as counter electrode and 1 M lithium hexafluorophophate ($LiPF_6$) dissolved in a mixture of ethylene carbonate (EC) and dimethyl carbonate (DMC) (1:1 by weight) as electrolyte. Galvanostatic cycling charge/discharge was then performed with the constant rate of C/5 and voltage window of 0.01-3V.

The capacity performance and voltage profile displayed in figure 2.11 are the data collected from the fast pre-oxidized and fast carbonized CNFs which possess most pores and exhibit highest specific surface area. A very large irreversible capacity loss during the first cycle is observed, which is believed to be caused by the formation of solid electrolyte interface (SEI) layer and some side reactions with those residual nitrogen, oxygen and hydrogen atoms due to the low temperature carbonization process. After the first cycle, the capacity is much more stabilized and well maintained at 215 mAh/g. In the voltage profile as shown in figure 2.11 (B), there are no obvious plateaus other than the first discharge process, indicating that the intercalation of lithium ion is a continuous process and the porous structure plays an important role in storing lithium ions. However on the other hand, the as resulted voltage hysteresis, which is defined by the voltage difference between the voltage of lithium ion insertion during discharge process and the voltage of lithium ion extraction during charge process, does not favor the application of such material. Even though the specific capacity is not comparable to the commercialized graphite which has a specific capacity of 372 mAh/g, there is still much room for improvement, for example, substantial activation process can be carried out.

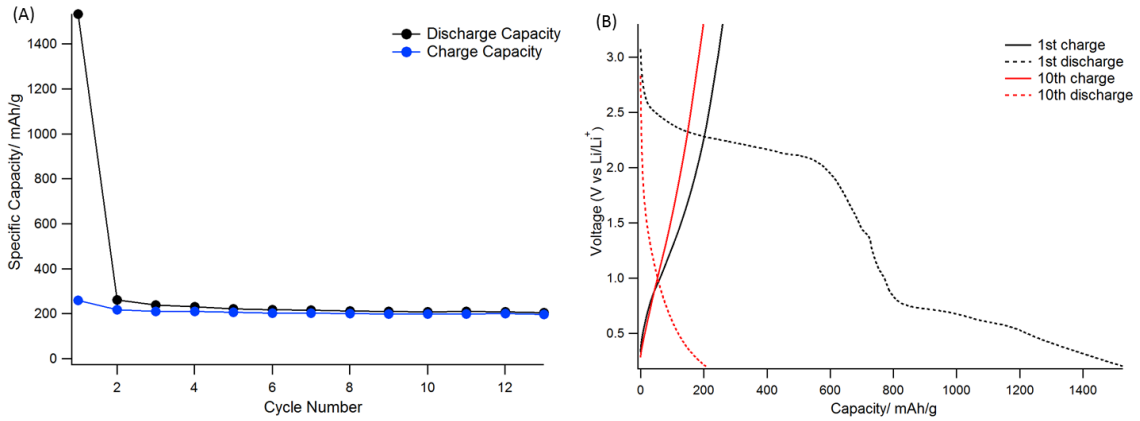

Figure 2.11 Battery performance of CNFs as lithium ion battery anode, (A) cycling performance and (B) voltage profile of 1st and 10th cycle

2.4 Activation of Carbon Nanofiber

Previous work has demonstrated the synthesis of porous CNFs using electrospinning technique, with moderate pore structure. With the rapid development of lithium ion battery electrodes, researchers have demonstrated that micropores and mesopores can both function as reservoirs for storing Li-ions, therefore, the capacity can be greatly improved with more pores. Thus, we tried to further improve the as-synthesized CNFs by physical activation, trying to create more pores. There are two types of activation for carbon samples: physical and chemical [120]. Chemical activation typically involves reacting with certain chemicals such as potassium hydroxide (KOH), or sodium hydroxide (NaOH) at temperatures between 450 and 900 °C, where it is believed that activation and carbonization happens at the same time. Physical activation typically refers to heat the sample at elevated temperatures in an oxidizing environment, such as under the flow of oxygen, carbon dioxide, air or steam. In both processes, carbon reacts and some disordered carbons are removed, resulting in a mass loss [120]. The amount of mass loss during the process depends on multiple parameters such as the temperature and duration, and thus can be tuned for specific applications. With a 50% activation, meaning weight loss after

activation is 50 %, new micropores are exposed, leading to a higher surface area, while higher level activation leads to larger average pore size but smaller surface area [121].

2.4.1 *Identifying the Activation Process*

Here in this study, we chose the physical activation process thanks to its simplicity and not involving any new hazardous chemicals. In order to determine an appropriate activation process to get an optimal porous structure, thermal analysis was first carried out on the synthesized CNFs with the help of TGA. Figure 2.12 shows the weight change when the CNFs were heated at 5 °C/min under constant air flow. As discussed above, a 50% level activation can lead to higher surface area with more exposed micropores, which should favor more lithium ion storage in theory. Therefore, we chose 50% weight loss as the criterion and found that 420 °C to be the activation temperature.

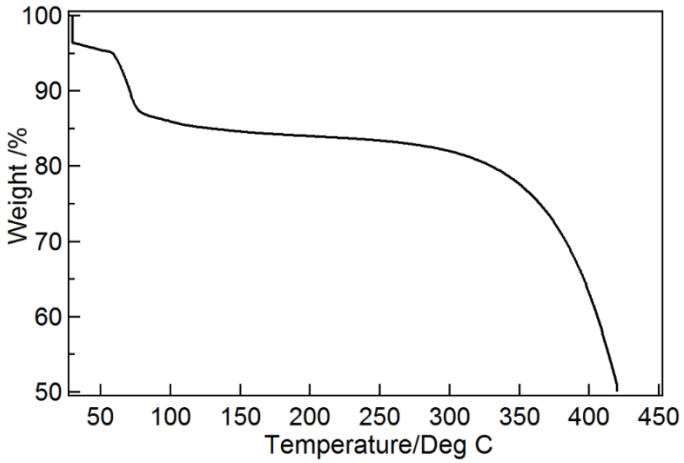

Figure 2.12 TGA measurement of CNF under air flow

In summary, the same electrospinning and three step heat treatment process as described in the previous session is still used to prepare the CNFs. Then those CNFs are heated to 420 °C in an oxidizing environment (constant air flow) with the ramp rate of 5 °C/min for activation,

followed by heat treated at 800 °C under nitrogen flow to remove some organic residuals formed during the activation process.

2.4.2 *Structural Characterization*

Morphology of the nanofibers before and after activation was examined using SEM, and the images are shown below. In general, the activated CNFs still maintain a good fibrous morphology and there is no obvious change of the fiber diameter. However, there are more exposed pores on the surface of the activated CNFs compared to the CNFs, as can be seen in figure 2.12 (C) and (D).

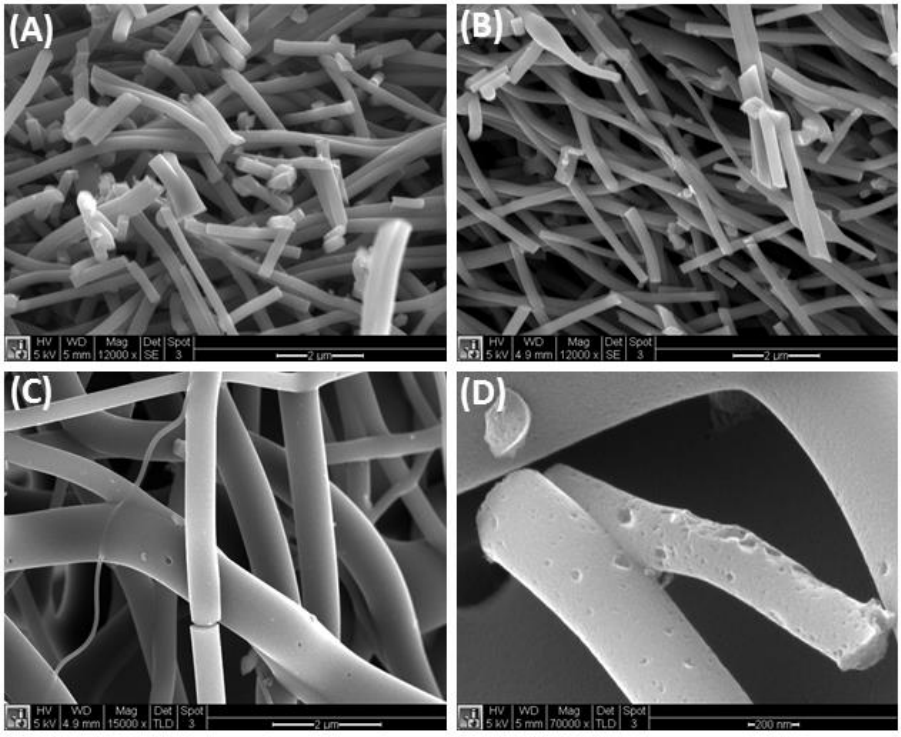

Figure 2.13 SEM images of (A) CNF, and (B,C,D) activated CNF

To further study how well the activation process works to improve the porous structure, physical adsorption of nitrogen at 77 K were measured on those nanofibers before and after activation for direct comparison. The nitrogen adsorption/desorption isotherm of activated CNFs,

as shown in figure 2.14 (B), displays a more obvious plateau, suggesting a more microporous behavior compared to the CNFs. The calculated BET surface area and statistics of the micropores and mesopores are summarized in table 2.2. Not only the total specific surface area gets increased by about 50% after the activation, but also the micropore size and volume gets much bigger. However, there are less mesopores present in the activated CNFs, which is not quite understood yet. This all together leads to a more microporous and less mesopours behavior of the activated CNF, which is consistent with what the isotherm suggests.

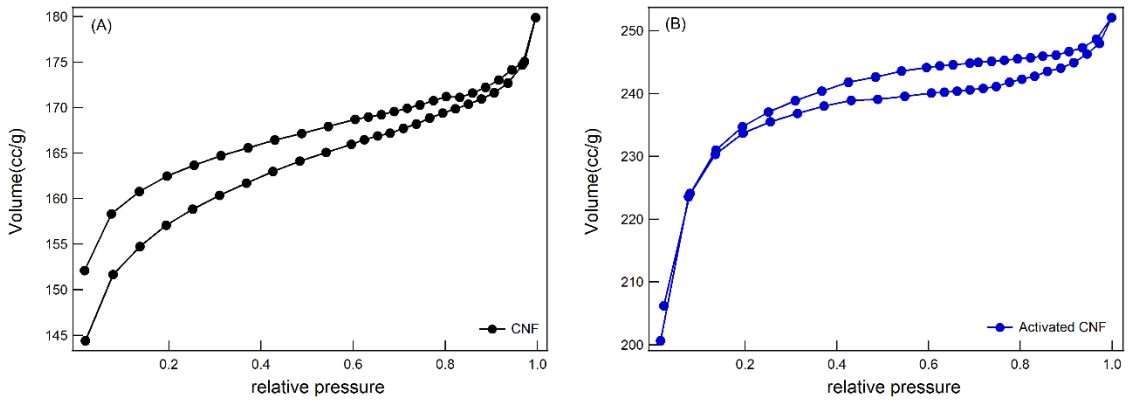

Figure 2.14 Nitrogen adsorption/desorption isotherm of (A) CNFs and (B) activated CNFs

Table 2.2 Summary of the porous property before and after activation

	CNF	**Activated CNF**
BET surface area	462.5 m^2/g	672.3 m^2/g
Micropore size	0.9 nm	1.62 nm
Micropore volume	0.238 cc/g	0.361 cc/g
Mesopore size	3.208 nm	3.658 nm
Mesopore volume	0.0368 cc/g	0.028 cc/g

2.4.3 *Performance of ACNF as Li-ion Battery Anode*

The BET results have shown that after activation, the nanofibers possess about 50% more micropores with larger average pore size, which in theory should favor the storage of lithium

ions. Thus, following the exactly same electrode preparation process and coin cell assembly process described in session 2.3.4, galvanostatic charge/discharge test was performed to measure the electrochemical performance of activated CNFs as lithium ion anode. Measurements of CNFs were also performed as control and comparison. In the cycling charge/discharge experiments, the rate was fixed at C/5 and the voltage window was chosen in between 0.01 V and 3.0 V. There exists an obvious irreversible capacity loss after the first discharge process for both CNF and activated CNF and the reason for that has been discussed previously. It is clear that activated CNFs demonstrates about 50% higher capacity than CNFs throughout the fifty cycles measurement, consistent with the 50% higher specific surface area and 50% larger micropore volume as well, and thus confirms our hypothesis that more micropores would favor the storage of lithium ions. The advantages of activated CNFs are: firstly, the one dimensional nanostructure provides a short path for electrolyte diffusion, and more importantly, the large amount of micropores with a large diameter (1.62 nm) can function as lithium ion reservoirs and thus improve the capacity.

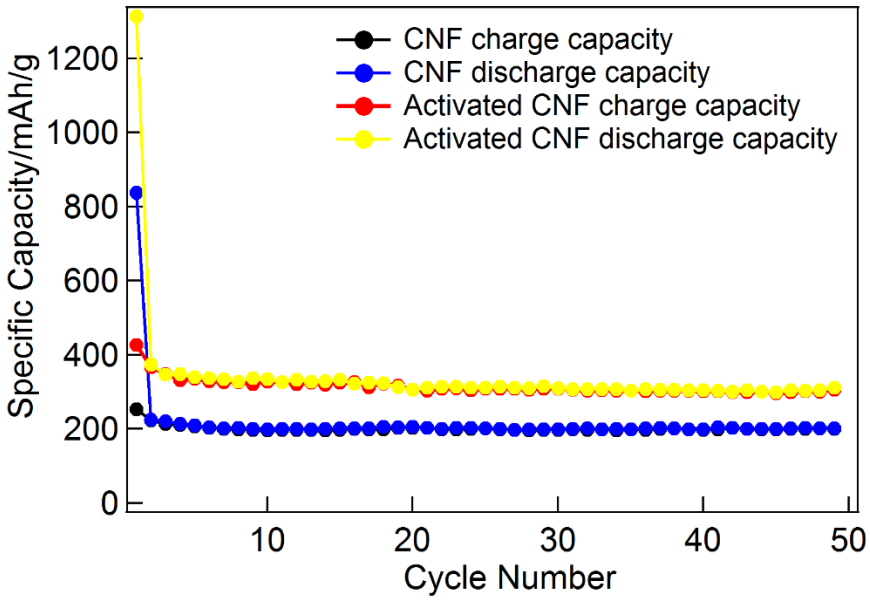

Figure 2.15 Battery performance of CNFs and activated CNFs

2.5 Summary

Electrospinning has been proved to be a versatile technique in the synthesis of functional materials for energy storage systems such as lithium ion batteries. In this chapter, synthesis of carbon nanofibers with moderate porous structures using electrospinning technique has been demonstrated. And efforts have been made to replace the mostly used carbon precursor PAN and NMP solvent, which is fairly expensive and toxic, with environmentally friendly and low cost PVP and ethanol solvent. A new three step heat treatment process has been identified to ensure the fibrous structure well maintained after substantial carbonization and different heat treatment parameters have been investigated to achieve a moderate porous structure of the final product: carbon nanofiber. Structural characterization has confirmed the amorphous nature of the low temperature pyrolyzed carbon.

With the help of substantial physical activation in an oxidizing environment, the activated carbon nanofibers possess a larger amount of micropores with a larger average diameter compared to the as-synthesized carbon nanofibers. Both the carbon nanofibers and activated carbon nanofibers have demonstrated promising capabilities as lithium ion battery anode, particularly the activated carbon nanofibers show much enhanced performance. However, there is still much room for improvement, not to mention that the specific capacity is still lower than the commercialized graphite anode. One important drawback of the carbon nanofibers is the large irreversible capacity loss during the first cycle. A method to reduce the capacity loss would have to be developed in order for this carbon nanofiber to be feasible for practical applications. Furthermore, those carbon nanofibers are also promising candidates for making composites with for example, silicon and tin, improving the electrical conductivity while also providing structural

support to help release the large mechanical stress produced during the lithiation process due to the large volume expansion.

Chapter 3. NANOIMPRINTED CARBON ANODES FOR LITHIUM ION BATTERIES

3.1 Motivation

3.1.1 *Introduction of Lithography Technologies*

Nanopatterning technology has attracted increasing attention since it demonstrated the high potential in improving the performance of many devices such as microelectromechanical systems (MEMS) [122, 123], LEDs [124], solar cells [125, 126] by creating the patterned structure. Various emerging techniques have demonstrated their capabilities in fabricating patterned nanostructure successfully on a large scale. Among those, the growth of soft lithography, photolithography and imprint lithography has exploded since the early 1990s.

Photolithography is mostly used in microelectronics industry, particularly all integrated circuits are fabricated using this technique. The process starts first with spin-coating a layer of photoresist on a silicon wafer and then transferring the pattern to a photoresist layer by exposing it to intense light. Then a liquid or plasma chemical agent removes the uppermost layer of the wafer in the areas that are not protected by the photoresist, followed by the final removal of the photoresist layer.

In contrast, soft lithography [123], a non-photolithographic method, uses an elastomeric material typically polydimethylsiloxane (PDMS), which patterned with relief structures, for patterning two- and three-dimensional structures with minimum feature size down to the region of 50-100 nm. This rather new lower-cost technique is more compatible with a broad range of materials and has been widely used in biotechnology [127]. One form of soft lithography, the microcontact printing (μCP) involves the application of "ink" onto the elastomeric stamp and the

molecular/atomic-level contact between the stamp and the substrate for transferring the ink onto the substrate. The ink molecules form self-assembled molecules during the process such that μCP can be used to pattern organic groups useful in cell biology [128].

Nanoimprint lithography [129, 130], first developed by Prof. S. Y. Chou and his team in 1995, is a nanopatterning technique based on external force and has demonstrated the capability of patterning sub-25nm structures over a large area. The process contains two major steps. The first is the imprint step in which a stamp with surface relief nanostructures is pressed onto a thin resist cast on a substrate during which a combination of heat and force is applied. Then the pattern transfer is finished with an anisotropic etching process to fully remove the residual resist in the compressed area. The temperature during the imprint step is typically higher than the glass transition temperature of the resist so that the resist becomes a viscous liquid and can be readily deformed into the shape of the stamp.

3.1.2 *Nanoimprint Lithography*

As mentioned above, photolithography is an optical method for transferring the pattern, therefore it cannot surmount the so-called “100 nm barrier” despite its wide application in microelectronics industry. The “100 nm barrier” is a critical value in reducing the feature size, determined by a combination of optical diffraction and short-wavelength cutoff to the transparency of the optical materials used as lenses [123]. Therefore, the resolution of photolithography is strongly limited. While nanoimprint lithography is based on direct mechanical deformation, therefore, it does not subject to the “100 nm” limitations. Researchers have successfully reported uniform large-scale patterning of structures down to 5 nm using nanoimprint lithography. Besides, nanoimprint lithography is a versatile, low-cost and high-

throughput alternative technique for industry applications. Considering all those advantages, nanoimprint lithography is chosen as the patterning method in this part of study.

3.1.3 *Advantages of Patterned Structure for Li-ion Batteries*

Even though lithium ion battery has achieved great success in commercial portable electronics, the conventional two-dimensional battery electrode structure limits the power and energy density. Several strategies have been developed to overcome those limitations, including nanostructuring the electrode [131, 132] and reconfiguration of the electrode structure [133-135]. By appropriate nanostructuring, the kinetics of the electrode/electrolyte reaction can be well improved, resulting in faster reaction and diffusion and thus better electrochemical performances [92]. For the other strategy, changing the conventional two-dimensional electrode design to three-dimensional can provide efficient ion and electron transport to potentially double the energy density by fully utilizing the space. The three-dimensional patterned architecture could also help accommodate the volume expansion during lithiation as well as reducing the mechanical stress [136], which can help maintain good cyclability and long lifetime.

In this research project, we combine nanoimprint lithography with the three-step heat treatment process we identified which can successfully carbonize PVP while maintaining the structure integrity, to fabricate carbon electrodes with three-dimensional patterned structure. The electrochemical performance of the patterned carbons is studied and scanning probe microscopy technique is applied to understand the nanoscale electrochemistry.

3.2 Synthesis of Imprinted Carbon

3.2.1 *Synthesis*

The process of fabricating three-dimensional patterned carbon consists of three major steps, as illustrated in figure 3.1. Firstly, PVP, the same carbon precursor as used in previous chapters, is dissolved in ethanol to form a homogeneous solution with moderate viscosity for spin-coating. Titanium foil with 0.25 mm thickness is used as both substrate for spin-coating and current collector for lithium ion battery assembly. The film thickness is adjusted to about 3 μm by controlling the solution concentration and spin rate. One step spinning at 1500 revolution per minute (rpm) for 20 s is used to get uniform deposition. After spin-coating, the as-deposited PVP film is dried at 55 °C for half an hour. Then, a hard Si stamp containing surface relief features is pressed into the PVP film under a controlled pressure, at a temperature above its glass transition temperature (150 °C). The stamp we use is a one-dimensional line grating with a period of 3 μm, line width of 2 μm and feature depth of 120 nm. The imprint process takes less than three minutes to fully transfer the pattern. After cooling down to room temperature and releasing the pressure, the stamp can be easily separated from the film, transferring the patterned feature of the stamp in a reverse fashion. Finally, the same three step heat treatment process is applied to carbonize the imprinted PVP film.

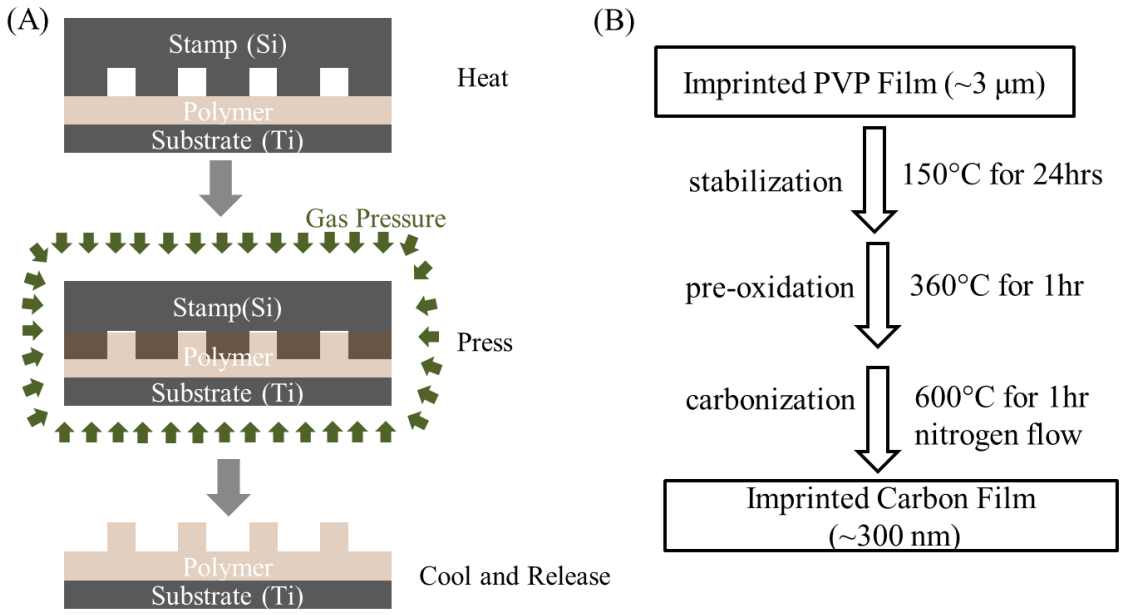

Figure 3.1 Synthesis process: (A) schematic of patterning the PVP film using nanoimprint lithography, (B) flow chart of the heat treatment process after imprint

To verify the complete transfer of the pattern structure, the imprinted PVP film is examined using atomic force microscope (AFM) and also scanning electron microscope (SEM), as shown in figure 3.2. The AFM topography scanning shows that the structure of the imprinted PVP film consists of 1 μm line gratings with depth of 120 nm, which exactly corresponds to the structure of the stamp. Moreover, SEM image under low magnification suggests that the pattern transfer can be accomplished on a large scale, as can been seen in figure 3.2 (B) where a large area of the film is patterned uniformly with minimal defects present.

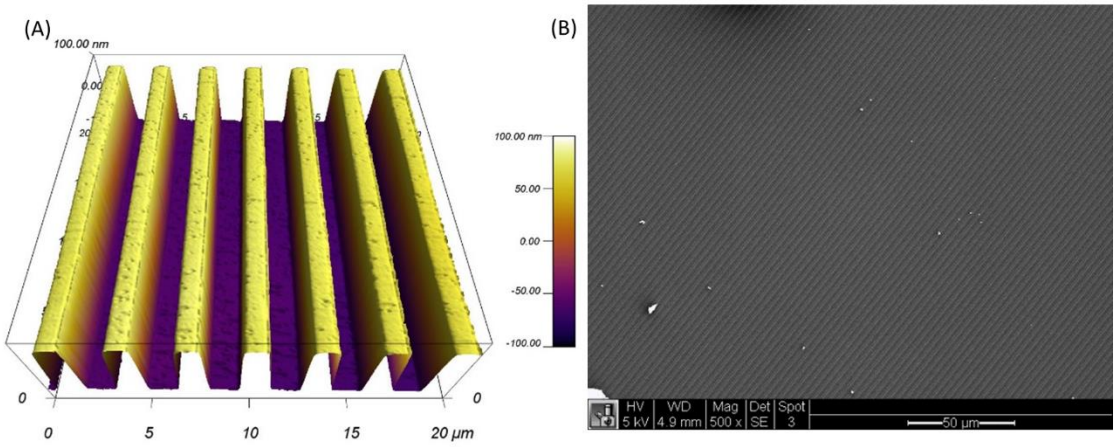

Figure 3.2 Microstructure of imprinted PVP film, (A) AFM 3D topography over an area of 20*20 um2, (B) SEM image at 500× magnification

In the meantime, AFM topography mappings of the imprinted PVP film and the film after each heat treatment step allows us to track the change of the pattern structure profile across the surface, as shown in figure 3.3. The mappings confirm that the three-step heat treatment process successfully maintains the patterned structure, though the pattern feature depth shrinks from 120 nm to about 45 nm after pre-oxidation and further reduces to about 15 nm after carbonization, while on the other hand, the shrinkage of pattern width is much smaller. The shape of the feature edge also turns to more rounded after the carbonization process instead of the initial square shape, as shown in figure 4.4. Furthermore, the film thickness measured by a profilometer also decreases from about 3 μm for the imprinted PVP film to about 300 nm for the imprinted carbon film, and similar vertical shrinkage has also been reported in previous work on photoresist-derived carbon films [137].

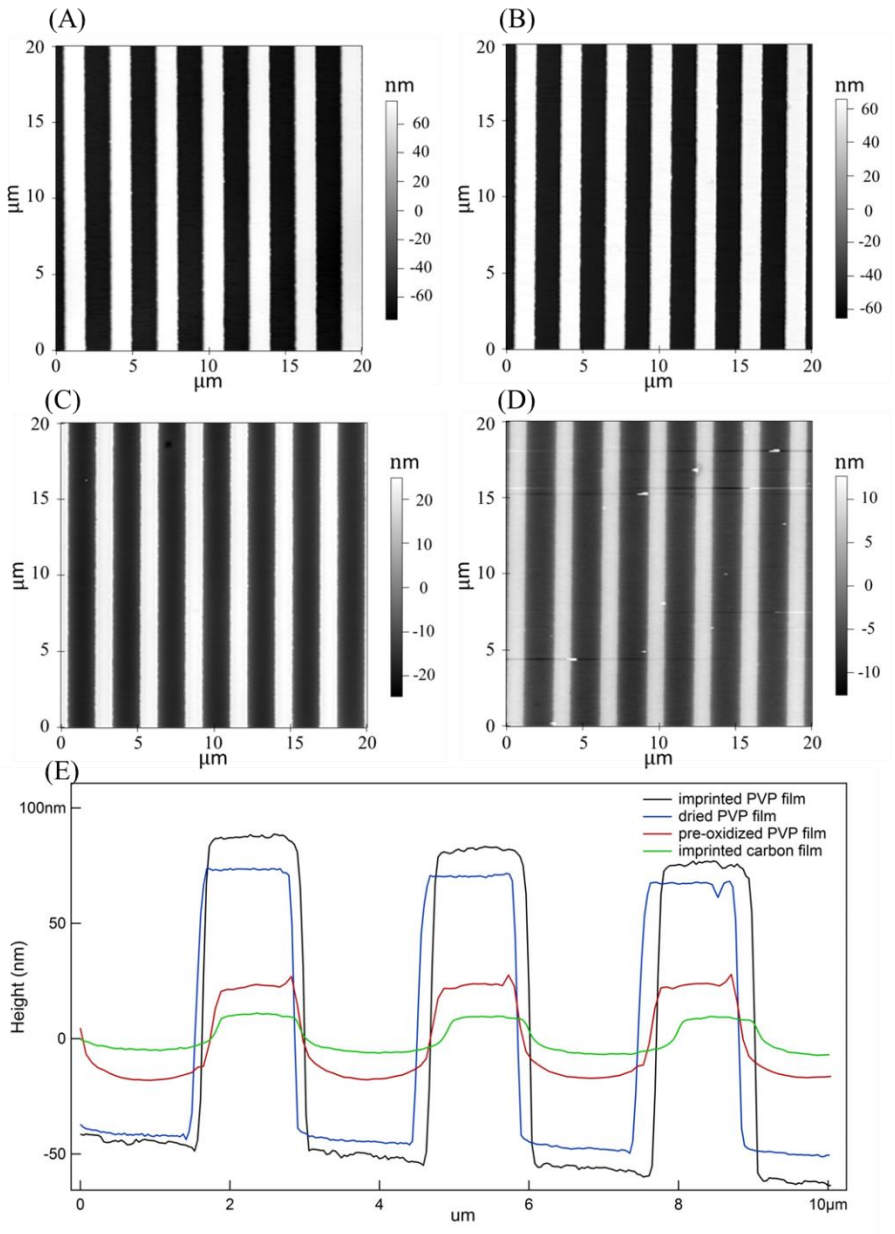

Figure 3.3 AFM topography mappings of (A) imprinted PVP film, (B) stabilized PVP film, (C) pre-oxidized PVP film, and (D) carbonized film; and (E) AFM height profile across the surface of four samples

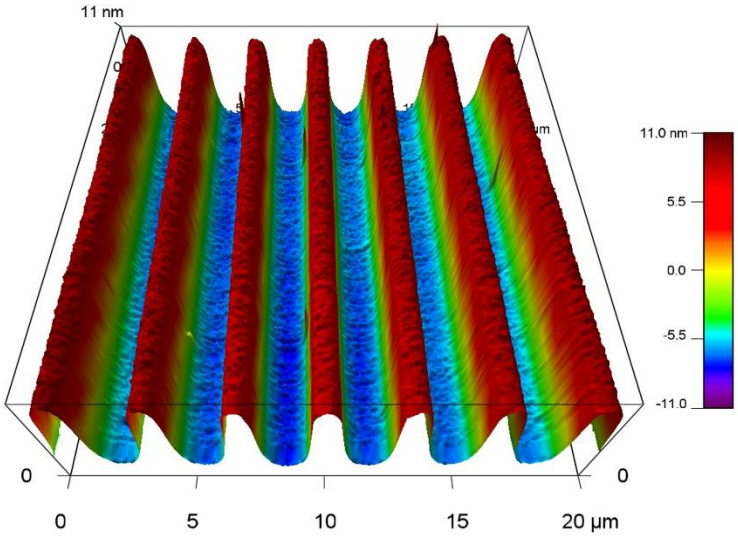

Figure 3.4 AFM 3D topography of the imprinted carbon film

3.2.2 *Structural Characterization*

The chemical structure and elemental composition of the imprinted carbon film was then investigated with X-ray photoelectron spectroscopy (XPS) and Raman spectroscopy. XPS can help quantitatively analyze the elemental composition while Raman can help understand the carbon atomic bonding. In the XPS spectrum shown in figure 3.5 (A), carbon, nitrogen and oxygen peaks are clearly identified and labeled. Quantitative analysis was carried out based on the area under each corresponding characteristic peak and the calculated results are listed in table 3.1. Compared with the precursor PVP, a relatively large amount of oxygen and nitrogen atoms were present in the carbon film, which is possibly due to the low carbonization temperature, 600 °C in this case. Previous reports claim that nitrogen and oxygen atoms in the organic polymers will be completely burnt off only when the heat treatment temperature is higher than 1500 °C [138, 139].

Then we also performed Raman measurement using a green laser with the wavelength of 514 nm as the excitation source. The Raman spectrum as shown in figure 3.5 (B) exhibits

characteristic features of graphitic materials, with two broad overlapping peaks, among which the D peak centers around 1365 cm^{-1} and the G peak centers around 1580 cm^{-1}. The G band is associated with the in-plane vibration of sp^2-bonded carbon atoms in graphite lattice and has E_{2g} symmetry. The presence of G band suggests that the sample is graphitic carbon, containing sp^2 carbon network. The D band is a breathing mode of A_{1g} symmetry and only becomes active in the presence of disorder. This D band does not exist in perfect graphite, therefore, the peak intensity ratio of D band over G band is always used to determine the degree of graphitization. With a higher value of *I(D)/I(G)*, the degree of graphitization becomes lower and the degree of disorder and defects in the material becomes higher [140, 141]. Fitted using Gaussian-Lorentzian mixed shape [142, 143], the intensity ratio of the D band to G band was found to be 3.27. Then the in-plane graphitic crystallite size L_a is estimated to be 1.35 nm with the relationship $L_a(nm) = 4.4 * (\frac{I_D}{I_G})^{-1}$ [144]. The relatively large value of *I(D)/I(G)* along with the widening of the peaks suggests the existence of a large amount of disordered carbon or structural defects.

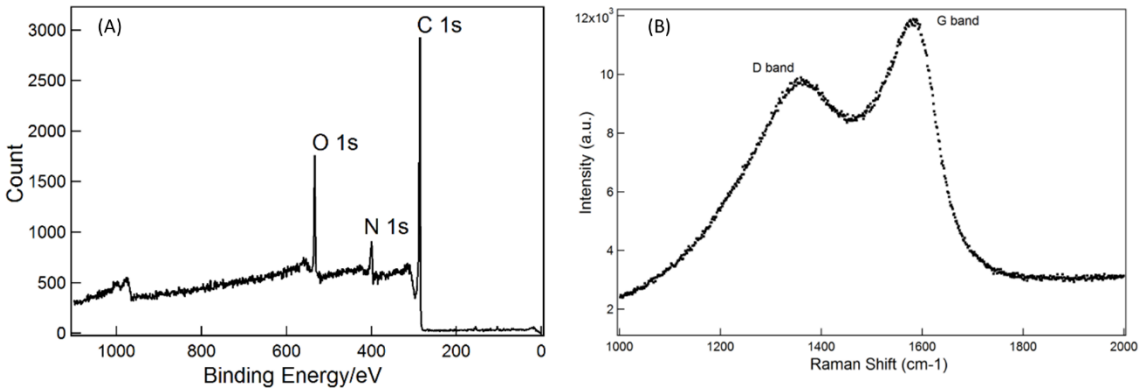

Figure 3.5 Structural characterization of the imprinted carbon film: (A) XPS spectrum and (B) Raman spectrum

Table 3.1 Table 3.1 Element composition of PVP and the imprinted carbon film calculated from XPS

Atomic percent %	**PVP $(C_6H_9NO)_n$**	**Imprinted Carbon**
Carbon	75	84.50±0.94
Oxygen	12.5	9.84±0.62
Nitrogen	12.5	5.66±0.33

The imprinted carbon film is designed to be used as lithium ion battery anode directly without any additional conductive filler. Therefore, to make sure it can provide an efficient pathway for electron flow, we also carried out conductive-AFM (c-AFM) experiments, where current was measured with a conductive SPM probe in contact with the sample surface when a known direct current (DC) bias is applied to the sample. Combining the current measurement with contact mode AFM imaging, c-AFM can simultaneously map the topography and current distribution. Figure 3.6 (A) shows the current mapping overlaid on 3D topography of the imprinted carbon film in a 5.5×5.5 μm^2 area under a 3 V DC bias, showing a nice contrast between the trench and top part. Furthermore, I-V curves were measured using a linear voltage sweep from -500 mV to +500 mV on six randomly chosen locations on both the trench and top parts, also suggesting higher current response from the trench parts. The measured current contrast between the top and trench part is due to the height difference which contributes to the length of the electric conduction L in the equation $R = \rho \frac{L}{A}$. Besides, the measured current response of I-V curves is higher than that of current mapping, due to different electrical contact. Basically, I-V curve is a static measurement done point by point where the probe sits on top of the point during the measurement, compared to the dynamic measurement of the current mapping where the probe sweeps across the sample surface. Therefore, I-V curve measurement has better electrical contact between the probe and the sample surface, resulting in higher current

response. The averaged current response shown in figure 3.6 (B) was on the same order of magnitude of that of multi-wall carbon nanotubes reported by Hietschold's group [145], suggesting a good electrical conductivity of the imprinted carbon film. Ideally, the I-V curve should be linear following Ohm's law as a conductor; however, experimental I-V curve is the superposition of majority Ohmic behavior and minor non-Ohmic behavior due to the residual organic components as a result of low heat treatment temperature.

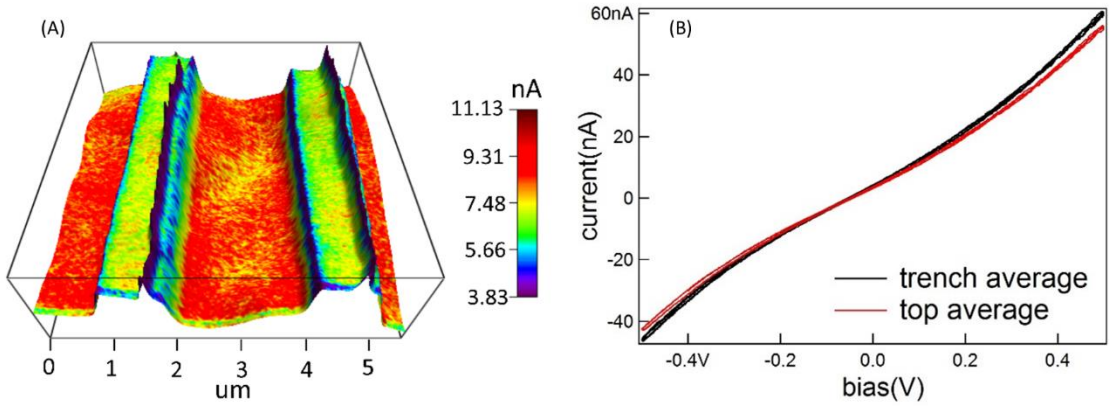

Figure 3.6 Conductive-AFM characterization of the imprinted carbon film: (A) current mapping overlaid on 3D topography under a 3 V DC bias, and (B) the averaged I-V curves recorded at six random locations of the top and trench parts

3.3 Performance of Imprinted Carbon

To evaluate the electrochemical performance of the imprinted carbon film, half-cell configuration is used with lithium metal as counter electrode and 1 M $LiPF_6$ in EC/DMC as electrolyte. Figure 3.7 shows the galvanostatic cyclic performance evaluated at a current density of about 20 μA cm^{-2} with the potential window of 0.01-2.8 V (vs. Li^+/Li). The high irreversible capacity loss and low Coulombic efficiency of the first cycle is the same as the performance of carbon nanofiber discussed in Chapter 2. After the first cycle, the coin cells maintained a relatively high Coulombic efficiency of about 96%. The specific capacity of the imprinted

carbon after charge/discharge for 98 cycles is 1.53±0.06 Ah cm^{-3} averaged over 8 samples, more than 100% higher than the theoretical capacity of graphite (0.75 Ah cm^{-3}). To further investigate what contributes to the enhanced capacity performance, the same galvanostatic cycling measurements are performed with two types of control samples. One control is prepared using the same spin-coating and three step heat treatment process without the nanoimprint step, referred to as "unpatterned carbon". The other control is prepared using the same spin-coating and nanoimprint process but without the stamp involved, referred to as "pressured carbon". As shown in figure 3.8, under the same cycling conditions, the imprinted carbon possesses the highest capacity, while the pressured carbon demonstrates slightly higher capacity than the unpatterned carbon. The result thus suggests that both the patterned structure and the pressurizing process improves the capacity, with most of the improvement coming from the patterned structure.

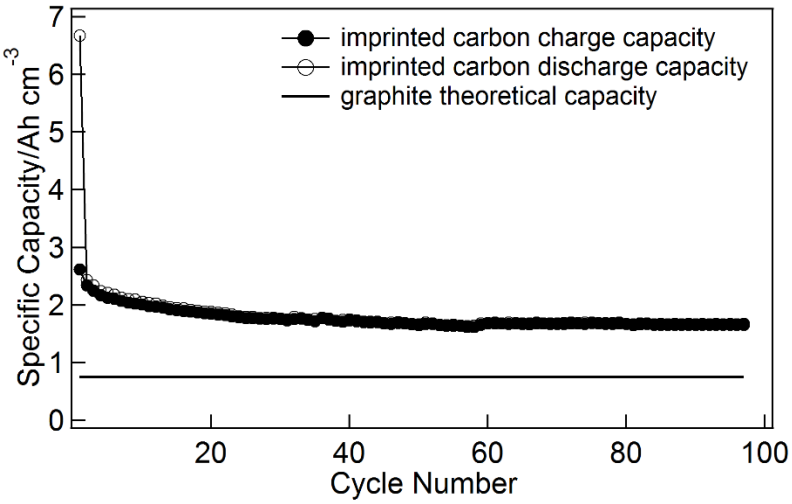

Figure 3.7 Galvanostatic cycling performance of the imprinted carbon

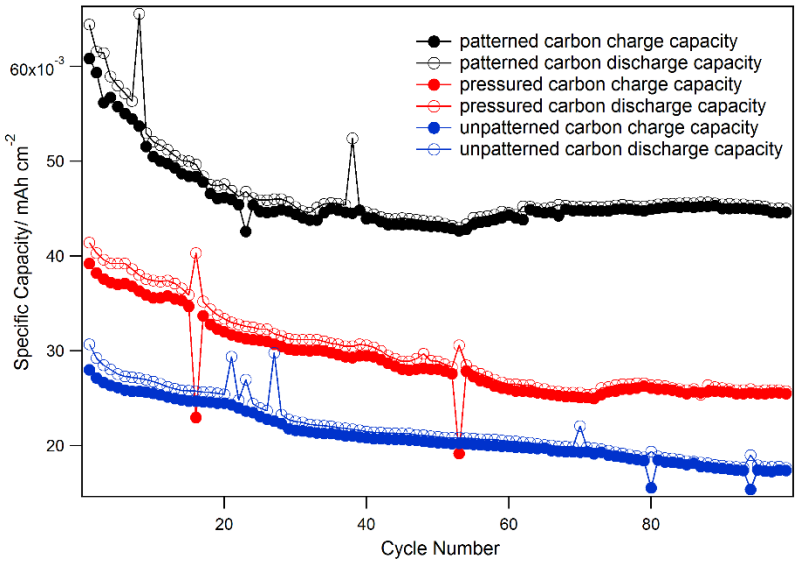

Figure 3.8 Galvanostatic cycling performance of the imprinted carbon and two control samples as comparison

To shed light on the possible mechanisms, the carbon samples were further studied microscopically with a novel scanning probe microscopy technique, electrochemical strain microscopy (ESM) [12, 146]. ESM has been widely used to study the localized electrochemistry of systems like battery electrodes and fuel cell electrolytes on the nanoscale. In principle, after a full discharge process during which the insertion of lithium ions into carbon anode occurs, Li_xC_6 compound is formed, enabling the probing of localized lithium ion redistribution by applying an external AC bias. The change of local lithium ion concentration will result in volume change and a surface displacement under the tip, which can be probed and referred to as ESM response. As intrinsic ESM response is very small, typically on the orders of several picometers, AC bias is always applied near the cantilever-sample resonance to magnify the response by orders of magnitude, as shown in figure 3.10 (A). The amplitude-frequency responses can be fitted with the damped driven harmonic oscillator model[147], allowing us to determine both the intrinsic ESM response and quality factor. With this technique, a series of experiments were performed on a fully lithiated imprinted carbon sample. The size of the sample is about 1×1 cm^2 while the size

of the patterned part, determined by the size of the Si stamp used during the imprint process, is about 0.3×0.3 cm^2. Therefore, only the middle part of the sample is patterned, while the rest is flat and featureless, as shown in figure 3.9. With such a sample, we were able to compare the difference between the patterned and unpatterned parts in a single specimen. Nine locations were randomly chosen on both parts, followed by measuring the amplitude response as a function of applied frequency at each location under an AC bias of 2-6 V with an increment of 1 V. Then with all the extracted resonance peak amplitudes and quality factors, averaged intrinsic amplitudes and energy dissipation, which is the reciprocal of qualify factor, are plotted versus the corresponding AC bias, as shown in figure 3.10 (B) and (C). In our previous work [148], we have shown that the ESM response, is proportional to the electric field φ generated by the AC bias, the local concentration n_0 of lithium ions, as well as the diffusion coefficient D, governed by the equation (3.1) below.

$$\frac{\partial n}{\partial t} = n_0 D \frac{zF}{RT} \nabla^2 \varphi \quad (3.1)$$

In figure 3.10 (B), an increase of the amplitude with the increase of the AC bias is observed, as expected. More importantly, the amplitude response of the patterned part is significantly larger than that of the unpatterned part at all biases, suggesting a larger local lithium ion concentration in the patterned part. To confirm this, quantitative analyses using XPS were also performed on the sample with five random locations selected on both the patterned and unpatterned part. The averaged elemental composition results calculated with XPS spectra are displayed in table 3.2, showing a higher Li/C atomic ratio of the patterned part (1.288) than the unpatterned part (1.121). With such observation, we can conclude that the patterned structure demonstrates the ability of storing more lithium ions than the unpatterned part.

Furthermore, energy dissipation of the patterned part is significantly lower, as plotted in figure 3.10 (C), indicating a smaller energy barrier for lithium ion diffusion, which favors the lithium ion insertion and extraction during cycling. ESM and XPS experiments thus reveal that due to the patterned structure, the imprinted carbon possesses higher lithium ion concentration with smaller energy barrier for diffusion, explaining its higher capacity at macroscopic scale. Even though we are not sure about the exact mechanism responsible for such enhancement, it may arise from the open architecture created by nanoimprint lithography, which helps relieving the internal stress during lithium insertion and extraction.

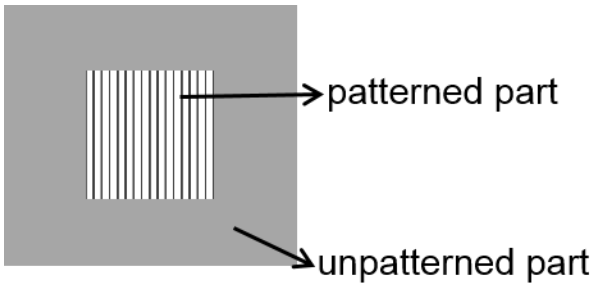

Figure 3.9 Illustration of the structure difference in an imprinted carbon sample

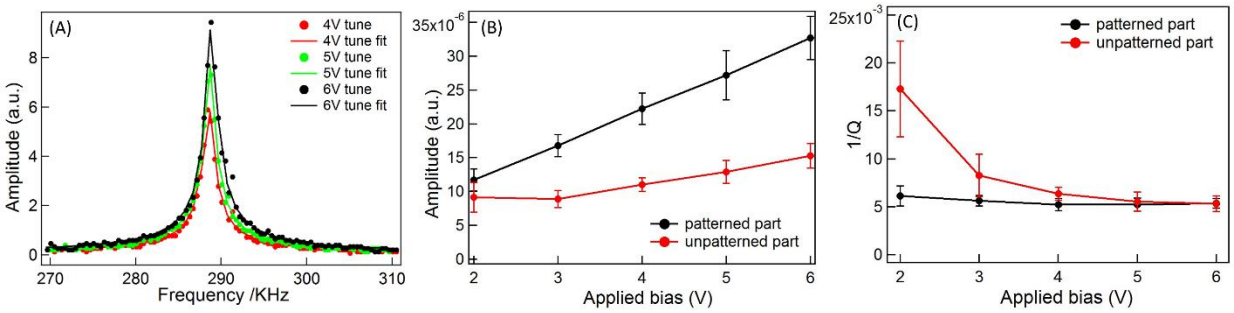

Figure 3.10 ESM of a lithiated carbon: (A) Amplitude-frequency responses, dots are experimental data and lines are fitting curve; (B) averaged intrinsic amplitude and (C) averaged energy dissipation versus applied AC bias of the patterned and unpatterned part

Table 3.2 Elemental composition of a fully lithiated imprinted carbon sample calculated using XPS spectra

Atomic percent %	patterned part	unpatterned part
Carbon	23.05±0.58	23.85±0.98
Lithium	29.70±0.83	26.71±1.07
Li/C ratio	1.288	1.121

3.4 Summary

In this chapter, nanoimprint lithography has proven to be an efficient technique to fabricate disordered carbons with patterned structure when combining with the three step heat treatment process developed in previous chapters. Different from using photolithography technique which most of the literature articles reported, we have replaced photoresist typically SU-8 with a more environment friendly and lower cost polymer precursor PVP as the carbon precursor while achieving the same nicely patterned structure. Due to the limitation of the low carbonization temperature, there are a relatively large amount of nitrogen and oxygen atoms left in the obtained carbons. Besides, the carbons display characteristic Raman peaks of graphitic carbon with lots of disorder and defects present. But the obtained carbons still exhibit good electrical conductivity, and thus can be used as battery anode without any additional conductive fillers. When directly used as lithium ion battery anode, the imprinted carbons exhibit 100% higher specific capacity than that of graphite over 100 cycles. Microscopic experiments study on a fully lithiated carbon sample with ESM and XPS reveal the enhanced lithium ion activity in the patterned part, which is responsible for the observed capacity enhancement.

However, we believe there is much room for improvement since the pattern structure is on the order of micrometer and yet can be further pushed down to nanometer. Toward this end, we use another stamp with smaller features to repeat the synthesis process. The stamp we used is a

two-dimensional grating with the hole diameter of around 250 nm. Our preliminary results have shown that this two-dimensional structure can also be successfully transferred onto the PVP film and well maintained after the carbonization process, leaving a two-dimensional array of pillars with a diameter of around 250 nm and depth of around 20 nm, as shown in figure 3.11. Furthermore, the aspect ratio of the pattern can also be tuned in order to achieve the optimal performance.

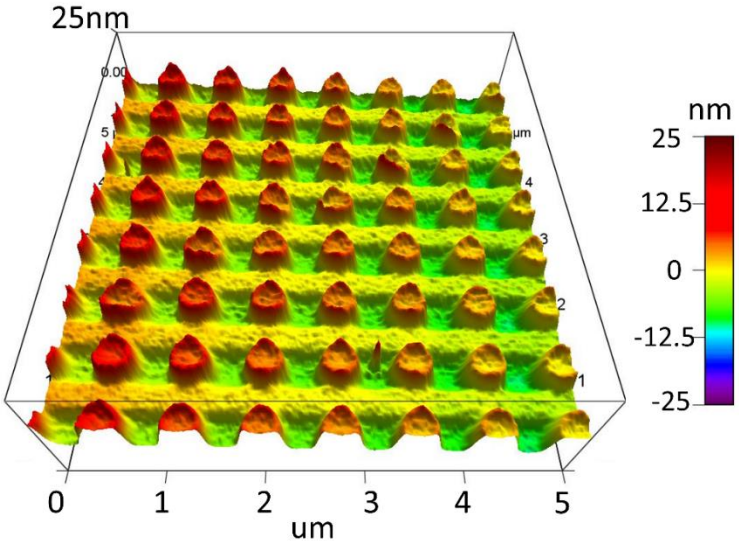

Figure 3.11 3D AFM topography mapping of the carbon film imprinted with the 2D grating with hole structure

Chapter 4. FERROELECTRICITY AND PHOTO-INDUCED FERROELECTRIC SWITCHING IN PEROVSKITE $CH_3NH_3PBI_3$ FILMS

4.1 Motivation

In the last a few years, solar cells based on a layer of halide perovskite as the active material undergo very rapid development. The photovoltaic conversion efficiencies of those solar cells rise to over 20% from 3.8% in less than ten years [24, 149, 150], revealing the huge potential of the next generation organometal trihalide perovskite (OTP) solar cell. The family of organometal trihalide perovskites, for example, methyl ammonium lead halides ($CH_3NH_3PbX_3$, X = Cl, Br, I) has attracted lots of attention as the light absorber layer in solar cells due to its favorable band structure, large absorption coefficient, high dielectric constant and long carrier diffusion length [151-153]. Additional advantage is that solution-processing is most commonly used fabrication method to deposit the perovskite layer, which is low cost, low temperature, easy to integrate and scale up.

However, there are still problems to be addressed first, among which the hysteresis effect often observed in the current-voltage (JV) curves is a critical one. The hysteresis effect has been reported to depend on the scan rate, the contact material and also the lighting history, which is not desirable for solar cell devices. Multiple theories have been proposed and experimentally proven to explain the effect, including ferroelectric nature; ion transport and charge trapping. Researchers have been trying so hard to understand the hysteresis effect; nevertheless, there is no conclusion yet.

Among the entire family of organometal trihalide perovskites, $CH_3NH_3PbI_3$ is the first one reported for solar cell application and also the most studied one so far. Therefore, we chose this

material as our model system to study using various SPM techniques. At room temperature, $CH_3NH_3PbI_3$ possesses a tetragonal crystal structure, consisting of the polarizable organic cation $CH_3NH_3^+$ in 12-fold cuboctahedral coordination [154]. The tetragonal $CH_3NH_3PbI_3$ belongs to the 4*mm* point group and I4*cm* space group, suggesting that in theory, this material should be ferroelectric by nature, which is also predicted by the Ab initio calculations using density functional theories [41]. There are also literature reports showing some clear images of ferroelectric domains in the material measured with PFM [39, 45], yet many other similar studies were inconclusive [38], and some leading PFM experts reported observation of neither ferroelectric domain nor polarization switching [46]. As a result, there is still lack of conclusive evidence of the intrinsic ferroelectric properties of this material. To complicate the situation even more, it is now well understood that ionic motions, electrostatic interactions, and also induced electrochemical dipoles could all result in ferroelectric-like behaviors in the PFM experiments, and all these effects are expected to exist in our material. As a result, there has been lots of arguing about its intrinsic ferroelectricity, making reliable measurements and data interpretation extremely challenging.

In this work, we want to first address the remaining question of whether $CH_3NH_3PbI_3$ is a ferroelectric material or not, using a set of carefully designed PFM measurements to exclude other possible electromechanical coupling mechanisms as the dominant sources of the piezoresponse observed in the material. Then, by combining surface potential measurement using KPFM and ferroelectric characterization with PFM, we try to understand the interactions between the ferroelectricity and the light illumination, which could potentially help design better material and device structures for solar cell applications.

4.2 Experiment Setup and Characterization of $CH_3NH_3PbI_3$ Films

4.2.1 *Experiment Setup*

To study the piezoelectric and ferroelectric properties of the sample, piezoresponse force microscopy is the main tool that we used, which excites the local electromechanical vibration through an AC voltage applied at sample-tip contact resonance frequency. In most cases, PFM measurements are performed at room temperature, under ambient conditions, meaning exposed to air and room light. However, the $CH_3NH_3PbI_3$ perovskite films degrade very fast in ambient condition, especially when exposed to water and oxygen. As a result, when doing PFM and KPFM measurements, there is constant nitrogen (N_2) flow over the sample surface to create an inert environment for sample protection. Besides, once the material is exposed to light illumination, there is more ionic activity involved in the system. Therefore, to directly compare the measured response under different light illumination conditions became critical, which could in turn help understand the interactions. Here, we customized the commercially available AFM system (Cypher ES, Asylum Research), to have (1) constant N2 flow through the sample surface and (2) have a blue laser with the wavelength of 488 nm that shines on top of the tip cantilever and also the probed area on the sample surface. Figure 4.1 below shows briefly how the modified AFM system looks like, where the blue laser is connected to the AFM head through the orange wire, as can be seen on the left corner. Shown on the right is the entire optics system hooked up with the 488nm blue laser, enabling the focus of the laser spot and tuning of the laser intensity. As can be seen in figure 4.2, the laser spot can be well focused on the sample surface underneath the AFM tip, and the laser intensity can be adjusted accordingly as well.

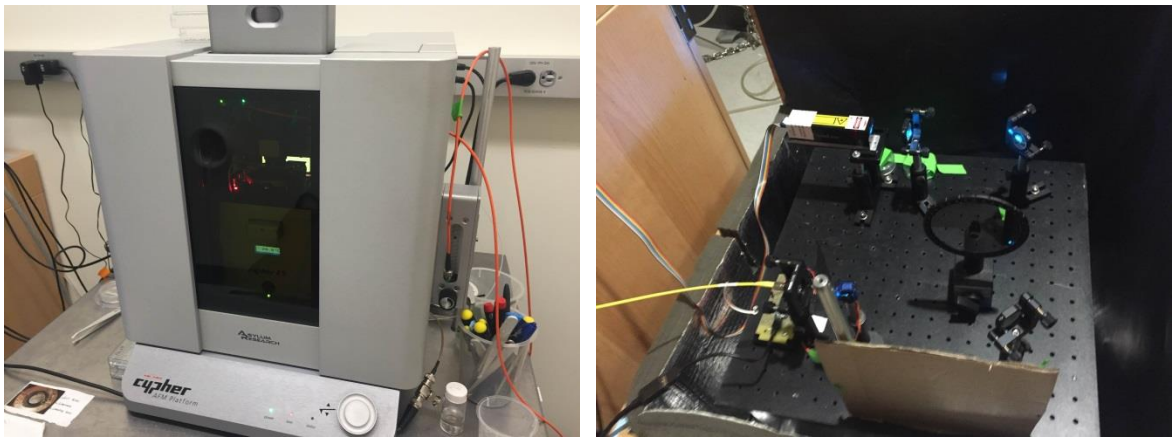

Figure 4.1 Pictures of the modified AFM system with the 488nm blue laser

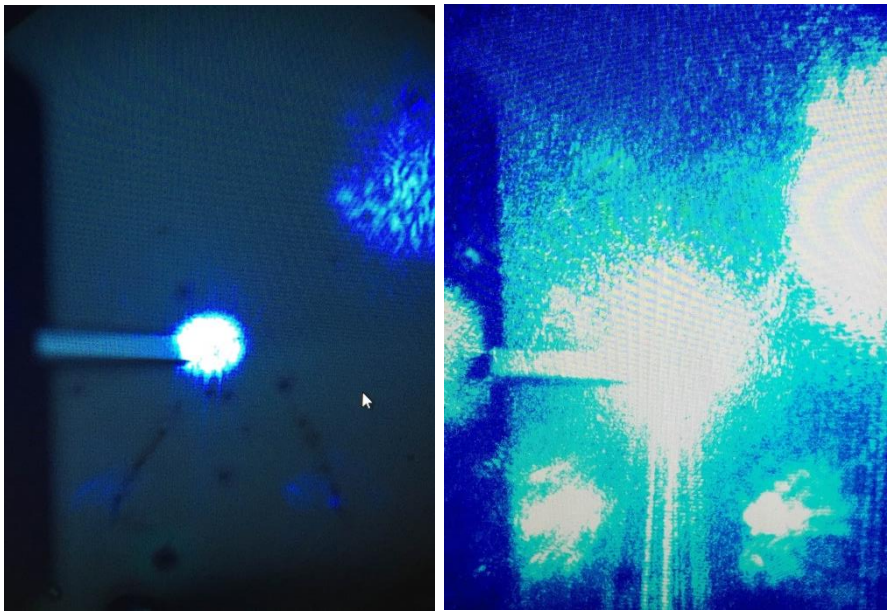

Figure 4.2 Pictures of the 488nm laser illumination on the sample

The material we studied is $CH_3NH_3PbI_3$, synthesized via one-step solution processing [155], provided by our collaborator Jinjin. As shown in figure 4.3, the crystalline structure is confirmed with X-ray diffraction (XRD) pattern and scanning electron microscope (SEM) images show the dense granular structure of the film. In the following experiments, we use 488nm blue laser as the light source, and the reason why we chose this wavelength is because UV-Vis spectra of

$CH_3NH_3PbI_3$ film exhibits a broad absorption spectrum ranging from 400 nm to 800 nm, as shown in figure 4.4.

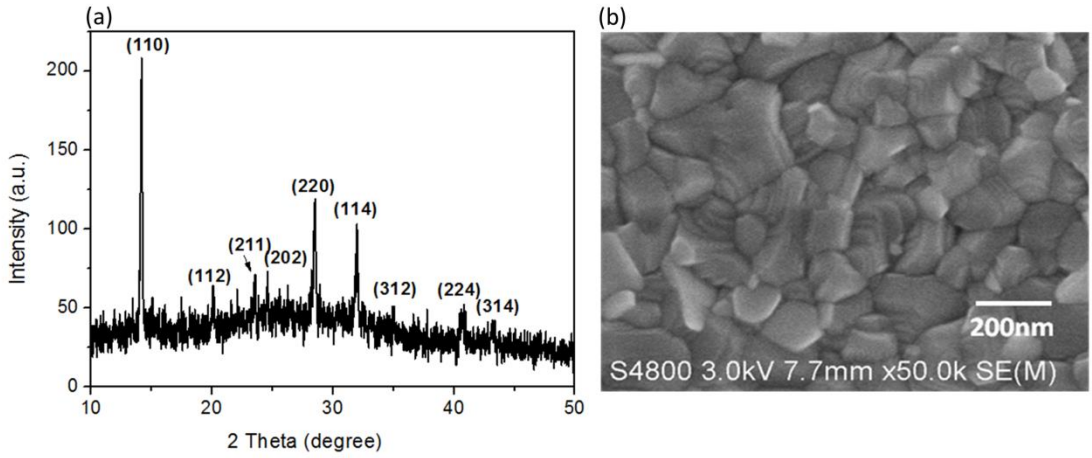

Figure 4.3 (a) XRD spectra of $CH_3NH_3PbI_3$ deposited on glass slide; (b) SEM image of $CH_3NH_3PbI_3$ on FTO substrate

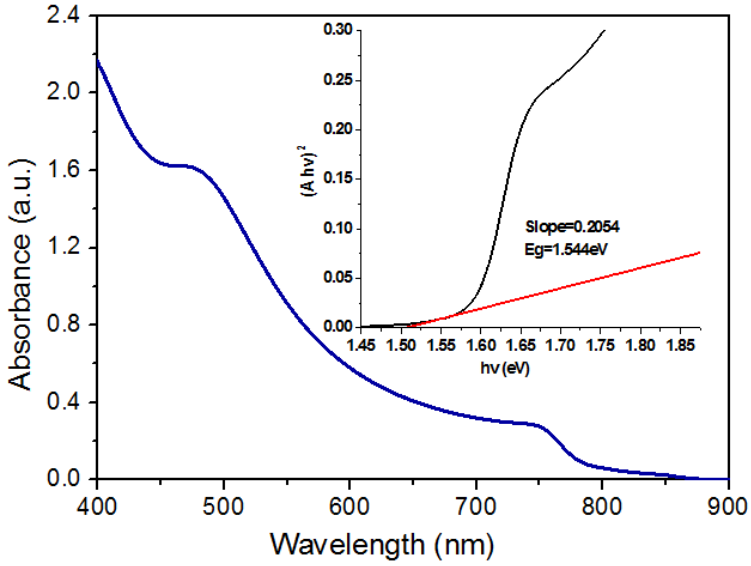

Figure 4.4 UV-vis spcetra of $CH_3NH_3PbI_3$ film, and the insert is plots of $(Ah\nu)^2$ against the photon energy($h\nu$) for $CH_3NH_3PbI_3$ film

For subsequent measurements using AFM, $CH_3NH_3PbI_3$ films are deposited on two different substrates, one is hole-collecting Poly(3,4-ethylenedioxythiophene):poly(p-styrene sulfonate)

(PEDOT:PSS) deposited on fluorine-doped tin oxide (FTO) glass substrates (FTO/PEDOT:PSS), and the other is the electron-collecting compact TiO_2 deposited on FTO glass substrates (FTO/TiO_2).

4.2.2 *Ferroelectricity Measurement*

To make sure we can draw conclusion from the ferroelectricity measurement, both microscopic and macroscopic measurements were performed carefully, both in dark environment and under light illumination.

Microscopically, we first examine its microscopic piezoelectric response using carefully designed PFM experiment, a powerful technique that excites the local electromechanical vibration of the sample through an AC voltage applied via a conducting scanning probe at the tip-sample contact resonance ω_0, as schematically shown in figure 4.4. However, we need to be extremely careful here with the response measured with PFM even though it was originally developed for piezoelectric and ferroelectric materials. And the reason is that PFM excites and probes all the electromechanical responses, which can arise from electrostatic interaction, capacitive effect, electrochemical dipoles, and ionic motion [80-82]. These effects are often nonlinear with the applied electric field, leading to prominent second harmonic response [156], while the linear piezoelectricity, on the other hand, should exhibit itself by predominantly first harmonic response, and this gives us a technique to assess different electromechanical coupling mechanisms.

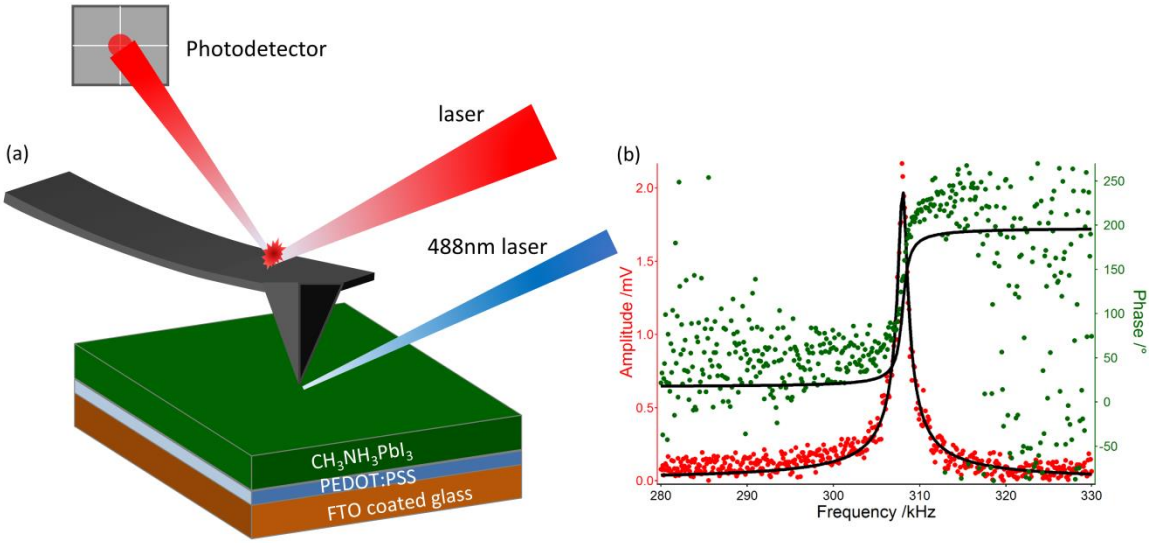

Figure 4.5 (a) Schematic of PFM experiment under light illumination, (b) piezoresponse as function of applied frequency, showing resonance frequency

Thus, to better understand the origin of the electromechanical coupling in $CH_3NH_3PbI_3$, we probe first (by exciting and measuring near ω_0) and second (by exciting at $\omega_0/2$ and measuring near ω_0) harmonic responses under an AC excitation of 1V, as schematically shown in figure 4.5, and the resulting responses at three representative locations are compared in figure 4.6. The sample used here is $CH_3NH_3PbI_3$ deposited on FTO/PEDOT:PSS substrates. The first point shows predominantly linear response and negligible quadratic one, while the second point has much smaller magnitude of first harmonic response, which is comparable to its second harmonic response. The third point, on the other hand, has larger first harmonic response, yet non-negligible second harmonic one. After repeating the measurement at multiple locations, we found that 62.5% of the data fall into case (a) and another 30% fall into case (c), while only 7.5% of the data are like case (b). We further explored the first vs second harmonic response under different AC excitation voltages, with the results plotted in figure 4.8 below. With increasing AC voltage, both linear and quadratic response increases. In particular, quadratic response increases

more dramatically, which is governed by mathematical equation. In addition, the first harmonic response is linear to the applied AC voltage by definition, as plotted in figure 4.8(e), which further validates the harmonic response measurement. These results suggest the piezoresponse in $CH_3NH_3PbI_3$ is predominantly linear, though they could be smeared by nonlinear electromechanical response when linear piezoelectric effect is small, for example due to the misaligned polar orientation. Also, another important learning is that it is better to use smaller AC excitation voltage to help eliminate the contribution from nonlinear electromechanical response.

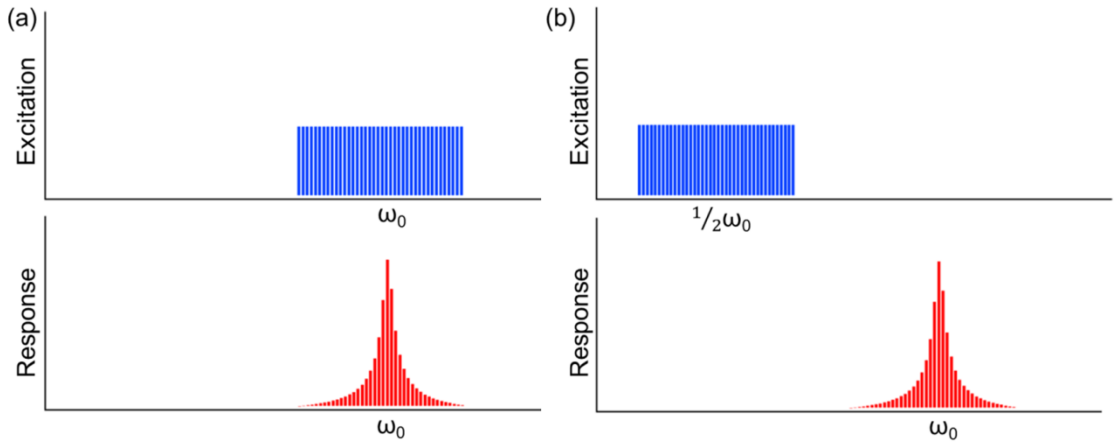

Figure 4.6 Schematic of (a) first and (b) second harmonic response measurement

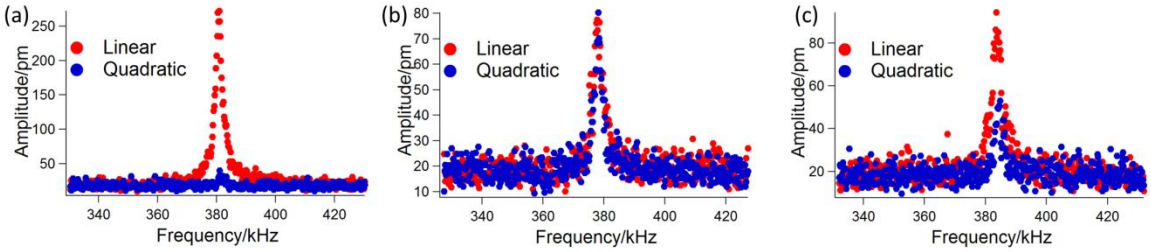

Figure 4.7 Measured first (linear) vs second (quadratic) harmonic response at different locations

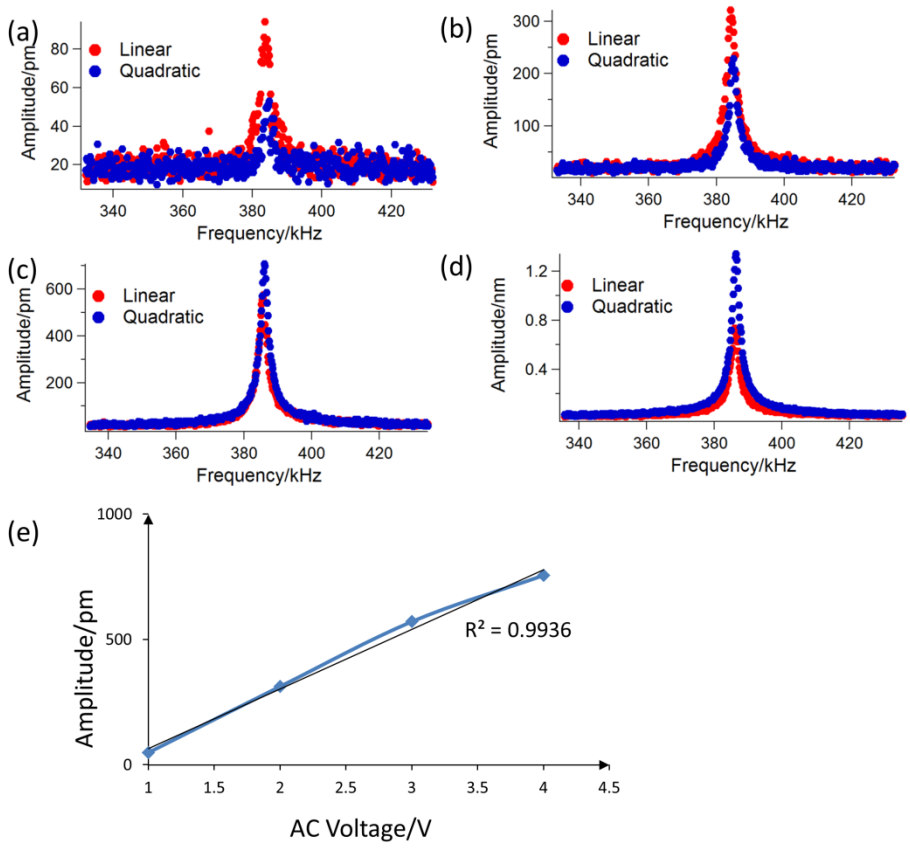

Figure 4.8 Meausrement of 1st vs 2nd harmonic response under (a) 1V AC, (b) 2V AC, (c) 3V AC, (d) 4V AC; (e) plot of linear response with respect to AC voltage, showing that the first harmonic response is linear with respect to the AC voltage applied, even when there is prominent nonlinear effect as demonstrated by the non-negligible second harmonic response

To further verify that the probed linear response arises from the spontaneous polarization of $CH_3NH_3PbI_3$, I also did PFM mappings on the sample surface with an application of 1V AC voltage excitation. Shown in figure 4.9 are a set of representative mapping of topography, PFM amplitude and also phase response. It is obvious that a clear domain pattern is observed in amplitude and phase mappings, uncorrelated with topography. This can be seen more clearly in the zoomed-in images of figure 4.9(d-f), where a wall separating two domains can be identified. Across a classical 180^o ferroelectric domain wall, it is expected that the phase of piezoresponse is

reversed, giving 180° phase contrast, while the amplitude drops at the domain wall and then bounces back, and this is exactly what we observe, as shown clearly by the line scan in figure 4.9(e-g). As such, the electromechanical response observed here cannot arise from ionic motion, for which the phase is not supposed to be reversed, and it cannot arise from nonlinear effects when the first harmonic response dominates. To further support our argument that the response is not due to ionic motion, we also carried out PFM mapping comparison between room temperature (RT) and high temperature (50 ˚C). Here, we chose to study at 50 ˚C for the reason that the CH3NH3PbI3 film is not stable at above 70 ˚C. The PFM mapping comparison is summarized in figure 4.10, showing a direct comparison of PFM response under same AC excitation voltage (1V). What we observed here is that PFM amplitude at 50 ˚C is smaller compared to room temperature data. This is consistent with typical ferroelectrics that exhibit reduced piezoelectric effect under increase temperature. If the response arises from ionic motion, then higher amplitude would be expected at higher temperature, due to increased mobility of ions. This set of data, in combination, establishes the linear piezoelectricity of $CH_3NH_3PbI_3$, and the 180° PFM phase contrast presumably arises from the spontaneous polarization of $CH_3NH_3PbI_3$ that is aligned antiparallel to each other.

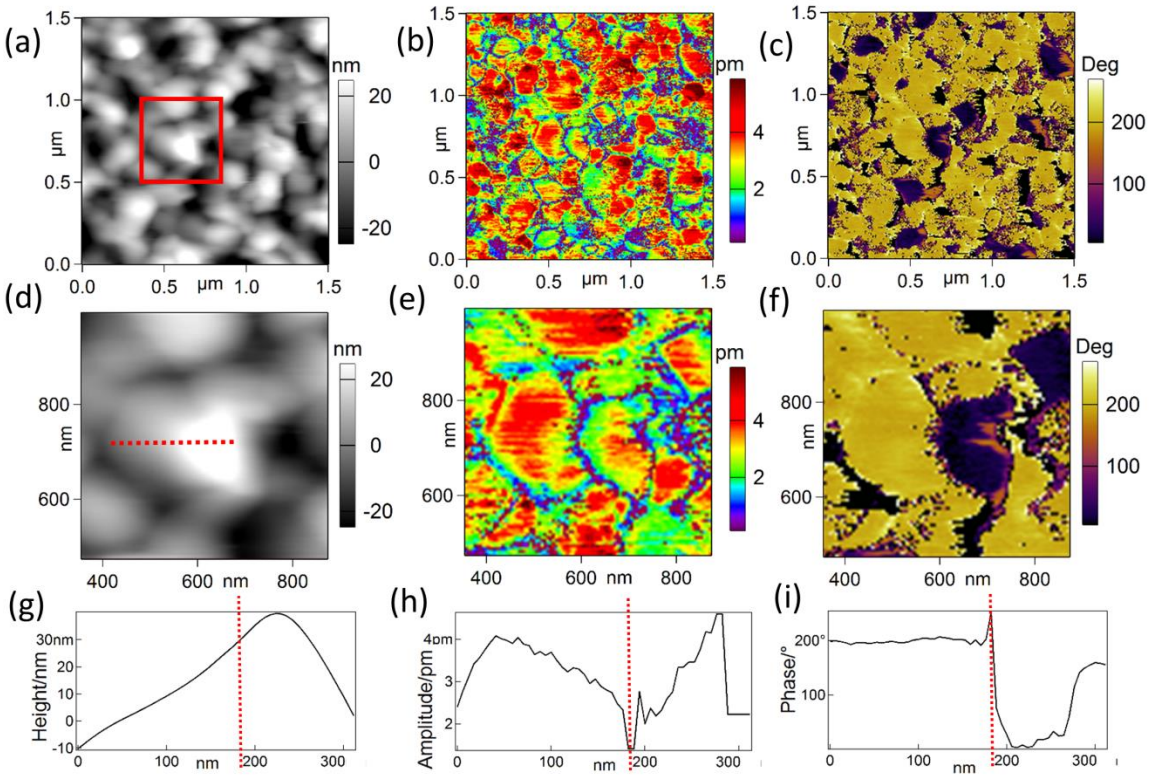

Figure 4.9 PFM mapping of $CH_3NH_3PbI_3$: (a,d,g) topography (b,e,h) PFM amplitude and (c,f,i) phase

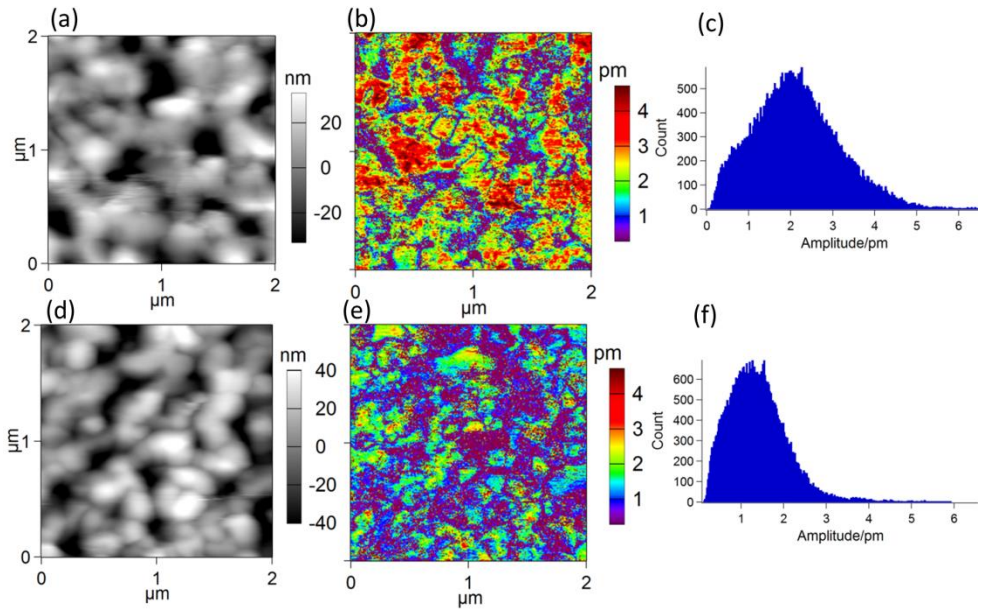

Figure 4.10 High temperature PFM mapping of CH3NH3PbI3: topography mapping at RT (a) and 50 ˚C (b); corrected amplitude mapping at RT (b) and 50 ˚C (d), amplitude histogram at RT (c) and 50 ˚C (f)

So far all the measurement results confirm that the spontaneous polarization with different orientation do exist in $CH_3NH_3PbI_3$, which is one proof of ferroelectricity. To further investigate on the ferroelectricity of $CH_3NH_3PbI_3$, I continued to study whether the spontaneous polarization can be switched or not, both microscopically and macroscopically.

Microscopic measurement of the switching behavior was performed with switching spectroscopy piezoresponse force microscopy (SSPFM). In SSPFM, a sweep of DC voltages with a triangular-square waveform is used, along with AC voltages always applying on top of DC voltages, as drawn in figure 4.11. DC voltages will induce a local change in the material, while AC voltages are used to measure the resulted amplitude and phase change. Here, only the measured response during the "DC off" stage is taken into consideration, for the reason that electrostatic response will dominate and cover up any other true responses during the "DC on" stage. Here, all the SSPFM measurements were carried out in dark environment to exclude the

contribution from photo-induced ionic motion. One example of resulted PFM amplitude-voltage butterfly loops and phase-voltage hysteresis loops are presented in figure 4.12, and such loops are generally interpreted as signatures for ferroelectric switching. However, it has recently been realized that electrochemical dipoles due to ionic motion can lead to apparent hysteresis and butterfly loops under PFM measurement as well[157, 158]. One method to distinguish these two different microscopic mechanisms is examining whether such loops would expand with the increased maximum DC voltage, an indication of longer range ionic redistribution and thus larger electrochemical dipole [157, 158]. This is not what we see here – the coercive voltages virtually overlap among three loops under different maximum DC voltages. Additional data in figure 4.13 also show that the loops are insensitive to the rate of DC voltage applied, while electrochemical dipoles induced by ionic motion is rate dependent [157, 158]. The hysteresis and butterfly loops we see in figure 4.12 thus cannot arise from ionic motion. Combined with the predominant first harmonic piezoresponse that indicates linear piezoelectric nature of electromechanical coupling, we can conclude with confidence that the switching behavior observed in $CH_3NH_3PbI_3$ is indeed due to the intrinsic ferroelectric properties.

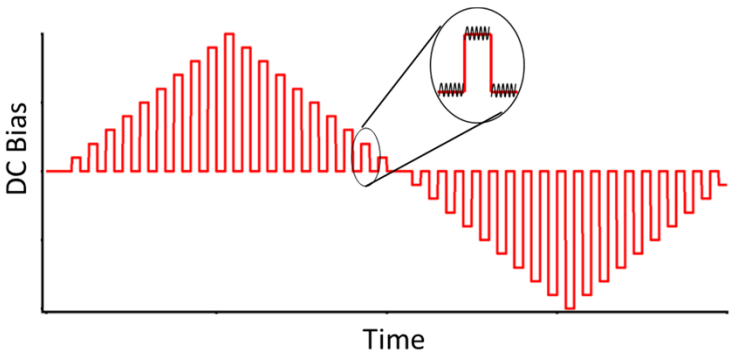

Figure 4.11 Triangular-square waveform of the applied DC+AC voltages in SSPFM measurement

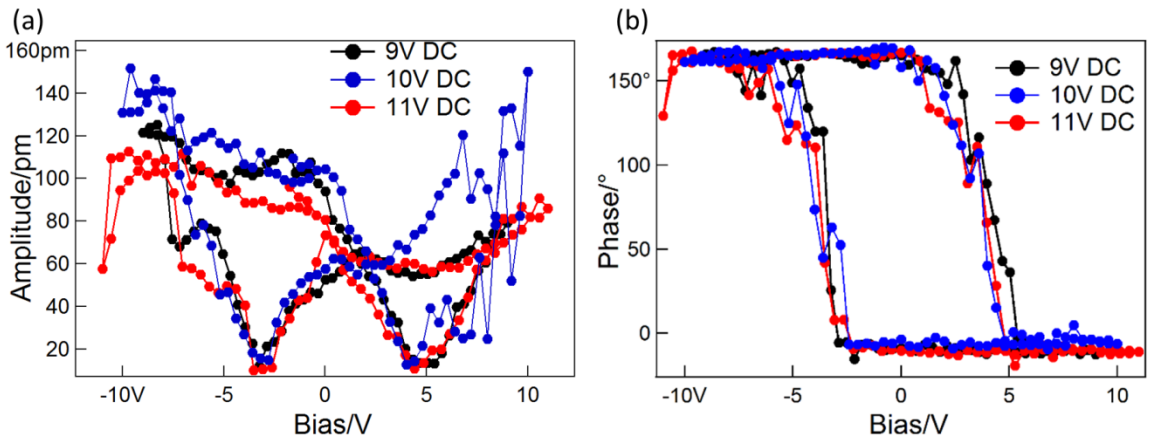

Figure 4.12 Ferroelectric switching of $CH_3NH_3PbI_3$ deposited on FTO/PEDOT:PSS substrate, (a) amplitude butterfly and (b) phase hysteresis loops under different max DC voltages

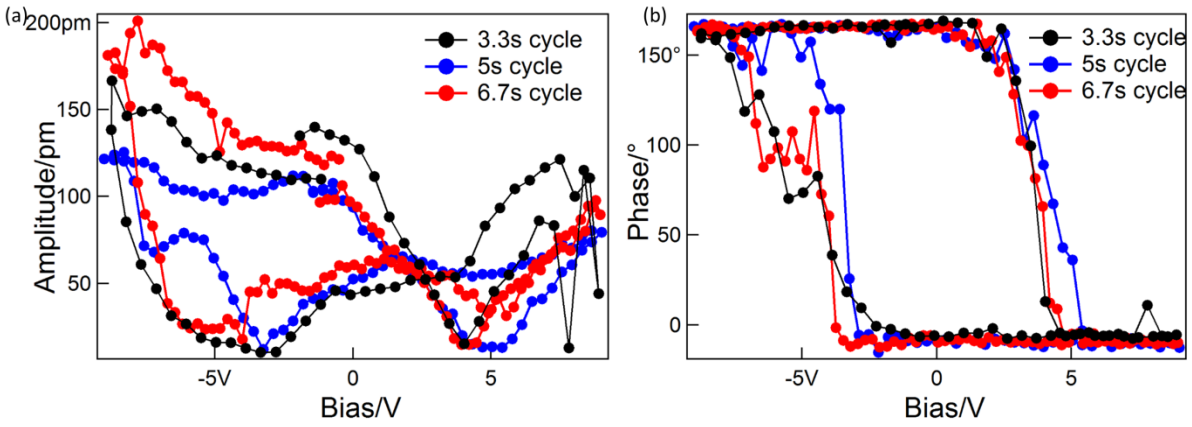

Figure 4.13Ferroelectric switching of $CH_3NH_3PbI_3$ deposited on FTO/PEDOT:PSS substrate, (a) amplitude butterfly and (b) phase hysteresis loops under different scan frequencies

Macroscopically, the polarization-electric field (PE) hysteresis loops were measured on the $CH_3NH_3PbI_3$ films deposited on FTO/PEDOT:PSS substrates using the Lake Shore TTPX Probe Station combined with the Radiant Precision LC Ferroelectric Tester. To apply the electric field to the perovskite films, a top electrode of 100nm thick Al layer was thermally evaporated onto $CH_3NH_3PbI_3$ films. The measurement was carried out at 1kHz at room temperature under

vacuum with controlled pressure of around 2.7×10^{-3} Pa. To better compare the macroscopic hysteresis behavior, the PE loops were measured with light on and off in sequence, using a laser source (LP450-SF15, THORLABS) with a wavelength of 450 nm and power of 0.5 mW. The measurements were performed at different starting conditions: for figure 4.14(a), the sample was initially exposed to light illumination and the PE loop was measured and recorded, followed by subsequent cyclic measurements of PE loops in dark and under light illumination. Same cyclic measurements of PE loops in dark and under light illumination were carried out, with the exception that the sample was initially kept in dark for the first PE loop measurement, which is shown in figure 4.14(b).

As seen from the polarization loops in figure 4.14(a), the first cycle under light illumination has high apparent remnant polarization of 19.42 $\mu C/cm^2$, and with the increased number of cycles, the remnant polarization gradually reduces, and then stabilizes at the 5^{th} cycles, with remnant polarization estimated around 6 $\mu C/cm^2$. If we start in dark, and then turn the light on, then the initial remnant polarization of 2.44 $\mu C/cm^2$ jumps to 4.86 $\mu C/cm^2$, and gradually reduces back to 2.52 $\mu C/cm^2$ after repeated testing with light on and off, as seen in figure 4.14(b). This set of data indicates that apparent polarization can be resulted from light illumination that arise from both photo-induced electronic and ionic currents, and then gradually dies down with repeated cycles. Since relatively high frequency of 1 kHz is used, the stabilized values should represent the intrinsic polarization, as ionic current is minimized, and leakage current appears to be small. Macroscopic ferroelectric measurement shows that the perovskite films possess intrinsic polarization of about 2 $\mu C/cm^2$, despite the apparent contributions from the photo-induced electronic and ionic currents under light illumination. Keeping the measurement

condition in dark could help eliminate the crosstalk efficiently, and examine the real intrinsic polarization.

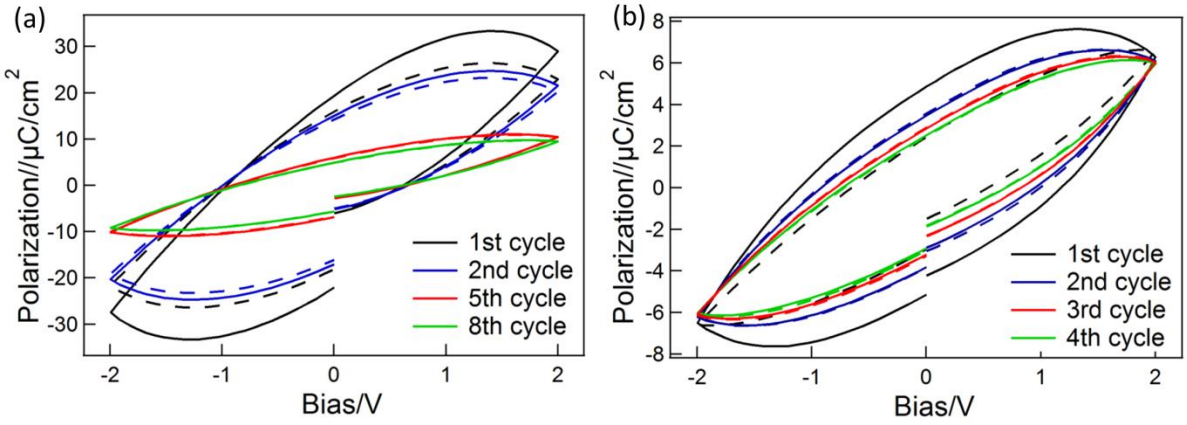

Figure 4.14 Macroscopic hysteresis loops measured at different cycles switched between dark (broken line) and light (solid line)

4.2.3 *Photo-induced Surface Potential Shifting*

Now that we have established evidence that $CH_3NH_3PbI_3$ is a ferroelectric material by nature, we are interested in how the ferroelectricity will affect the surface potential distribution. In theory, electric field would be induced inside a ferroelectric material, and compensated charges will be attracted to the surface, affecting the distribution of its surface potential. Since the polarization can be aligned upward, parallel, or downward with respect to the surface, the surface potential can be negative, zero, or positive value correspondingly. A simplified illustration is shown in figure 4.15 below.

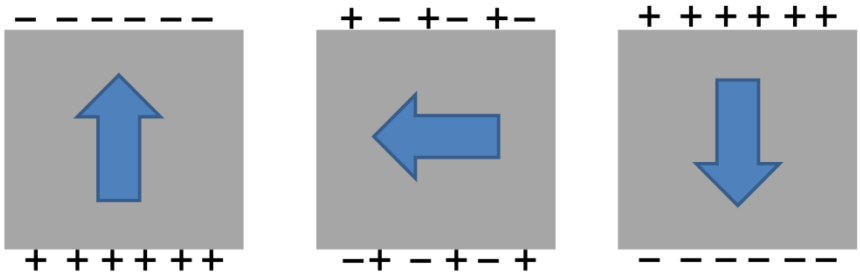

Figure 4.15 Polarization direction and corresponding surface compensation charge distribution

To examine whether experimentally this is true or not, I used Kelvin probe force microscopy (KPFM) to measure the surface potential distribution at different locations across different samples, in dark environment. In this set of experiment, $CH_3NH_3PbI_3$ deposited on both FTO/PEDOT:PSS substrate and FTO/TiO_2 substrate were studied. Displayed below in figure 4.16 are representative surface potential mappings across different locations in one sample deposited on FTO/PEDOT:PSS substrate, showing negative, near zero and positive values. In general, the surface potential is a measurement of the work function, reflecting the band structure and should be the same unless the band is bent upward or downward by the spontaneous polarization. This explains why the surface potential distributions across one sample differ about 100mV, as can be seen in the histogram of figure 4.16(d). Similarly, we also observed different surface potential distribution in the $CH_3NH_3PbI_3$ deposited on FTO/TiO_2 substrate sample, as shown in figure 4.17.

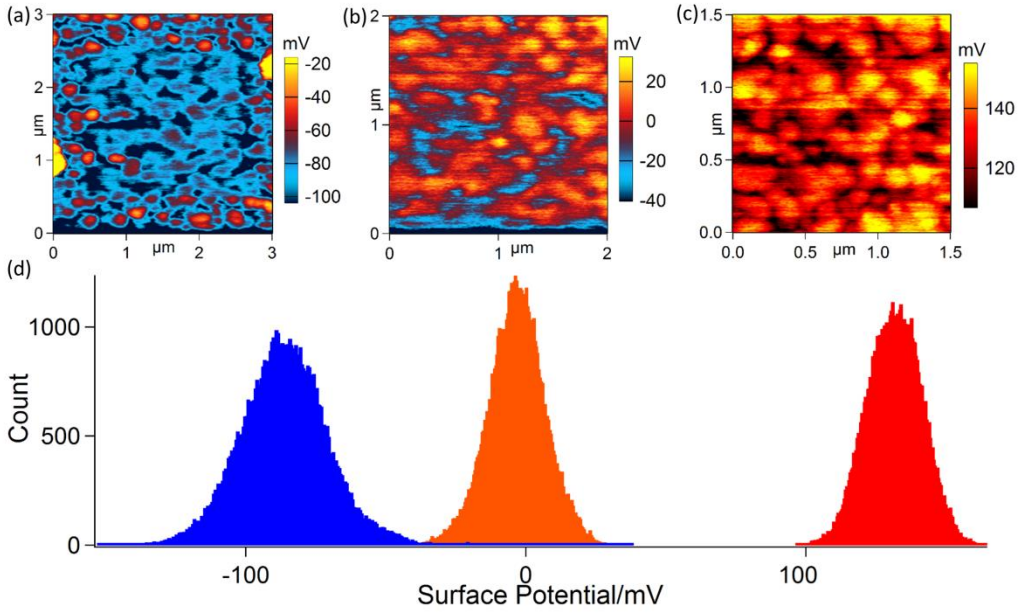

Figure 4.16 (a-c) Surface potential mappings of $CH_3NH_3PbI_3$ deposited on FTO/PEDOT:PSS substrate, (d) histogram distribution of the three mappings

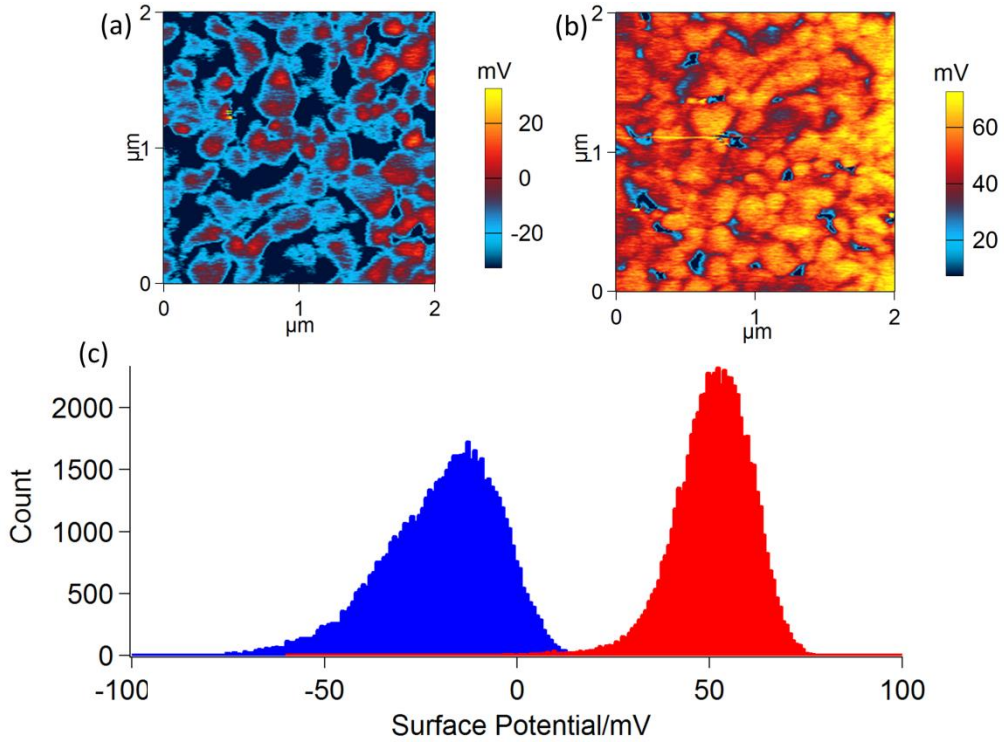

Figure 4.17 (a-b) surface potential mappings of CH3NH3PbI3 deposited on FTO/TiO2 substrate, (c) histrogram distributions

So far, all the surface potential measurements were performed in dark condition, to establish the baseline. Then, we use the same blue laser setup as used in the PFM experiment to illuminate the sample and then generate mobile charges (both electrons and holes) in the sample. Depending on the substrate composition, the flow of the charge could vary. For example, if the substrate is FTO/PEDOT:PSS, a hole collector, then the photo-generated holes will move downward to the PEDOT:PSS substrate, while electrons will move upward to the surface of the $CH_3NH_3PbI_3$ film, resulting in the surface potential shifting towards more negative value. The top row of figure 4.18 shows the surface potential mapping in dark environment and the bottom row refers to the result after 488nm laser illumination, from which a clear shift of surface potential toward more negative value can be observed. The topography mappings are to make sure the comparison of surface potential mapping in dark and under illumination is at the same location.

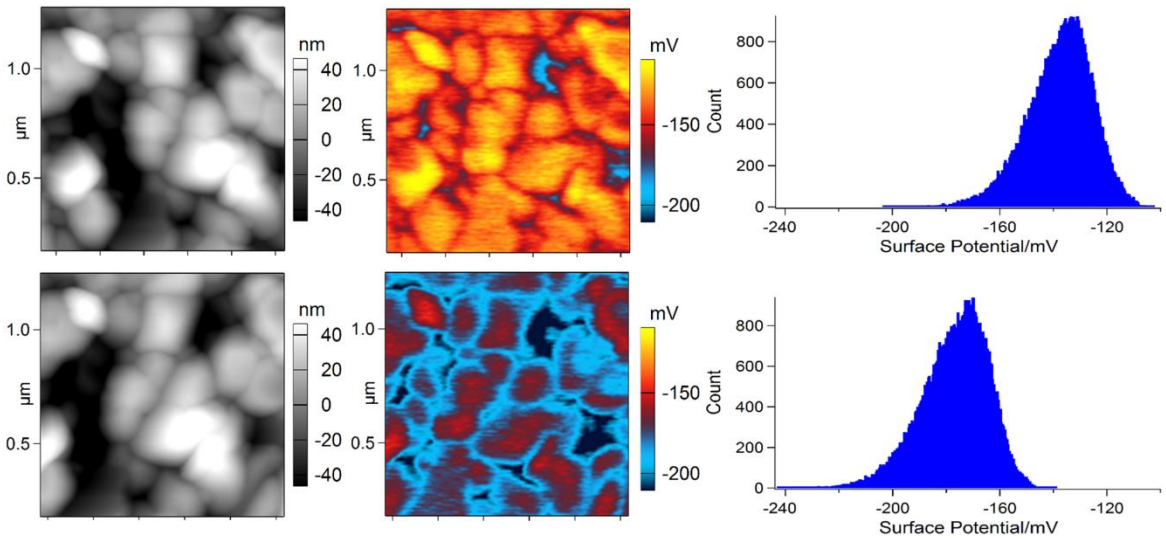

Figure 4.18 Surface potential change of $CH_3NH_3PbI_3$ on FTO/PEDOT:PSS substrate induced by 488nm laser illumination

When the same study was performed on another type of sample, $CH_3NH_3PbI_3$ on FTO/TiO_2 substrate, an electron collecting substrate, the electrons will migrate downward while holes will migrate upward to the surface, causing a positive shift of the surface potential. This is indeed what we observe during the measurement, as can be seen from figure 4.19. After laser illumination, the surface potential of the same scanned area increased by about 35 mV.

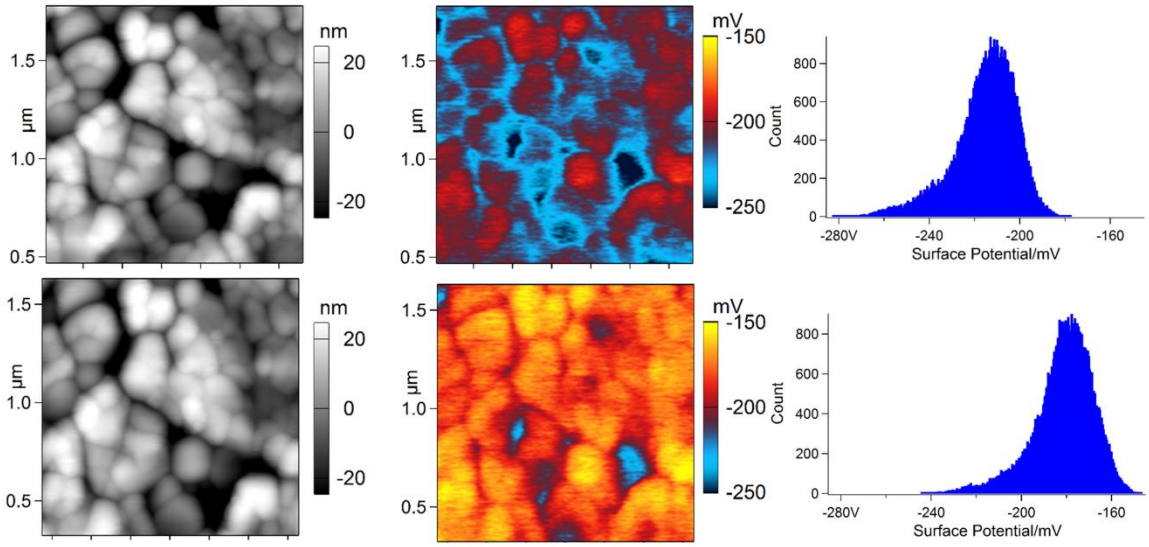

Figure 4.19 Surface potential change of $CH_3NH_3PbI_3$ on FTO/TiO_2 substrate induced by 488nm laser illumination

To further verify that the observed surface potential shift is indeed due to the photo-induced charges, I also measured the variation of surface potential distribution during multiple cycles between light on and off, and the result is shown in figure 4.20. As can be clearly seen for $CH_3NH_3PbI_3$ deposited on FTO/TiO_2, when the light is turned on, surface potential shifts toward more positive value, and falls back when the light is turned off, and the trend continues if the cycle is repeated. Similar observation of photo-induced surface potential shift is confirmed with different samples, regardless of light intensities. In all the experiments, topography mappings are

used to make sure that we compare surface potential distribution of the same area before and after light illumination.

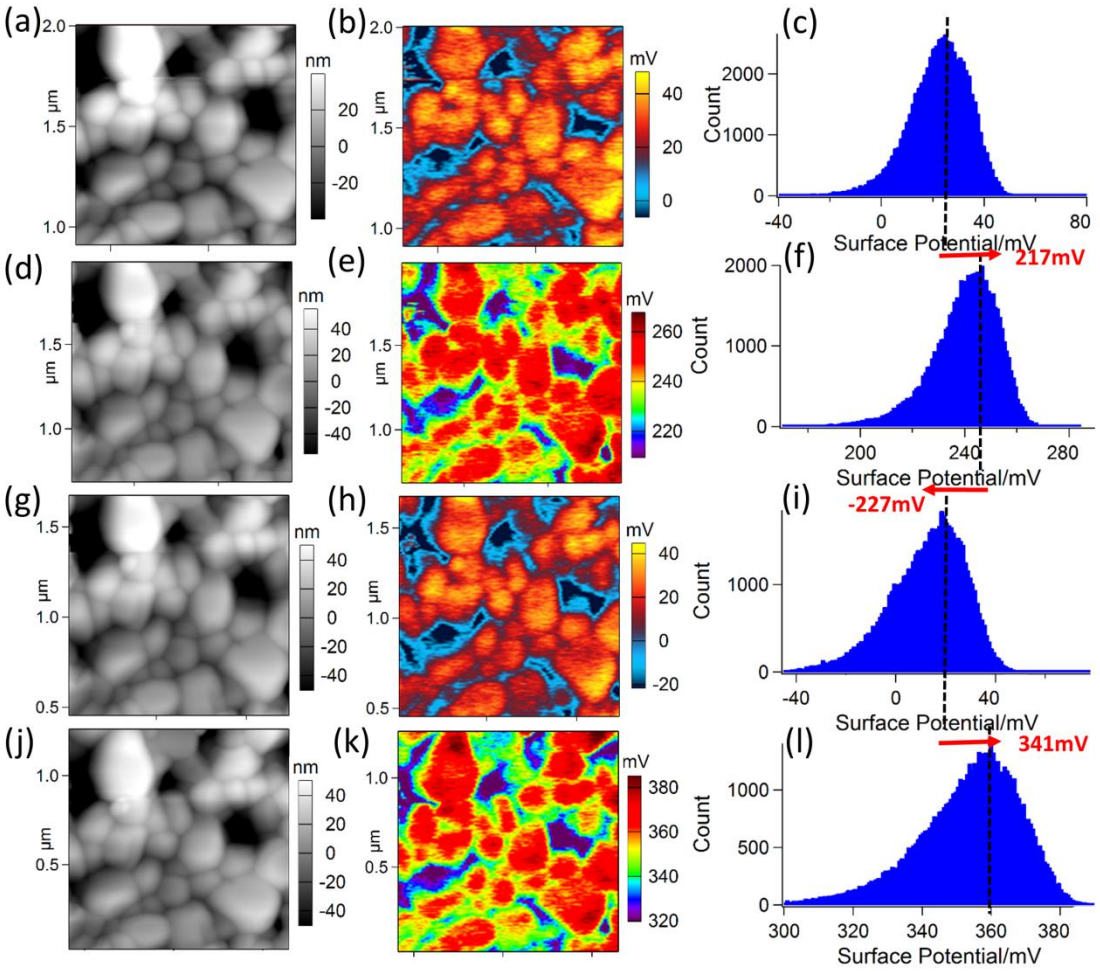

Figure 4.20 Surface potential shift of the $CH_3NH_3PbI_3$ film deposited on FTO/TiO_2, 1st and 3rd row in dark, 2nd and 4th row under laser

We also took one more step to measure the surface potential distribution evolution with the 488nm laser source on. And we found that with continuous light illumination for 15 minutes, the surface potential increases by 40 mV, as shown in figure 4.21, suggesting that more electrons and holes can be generated with continuous light illumination.

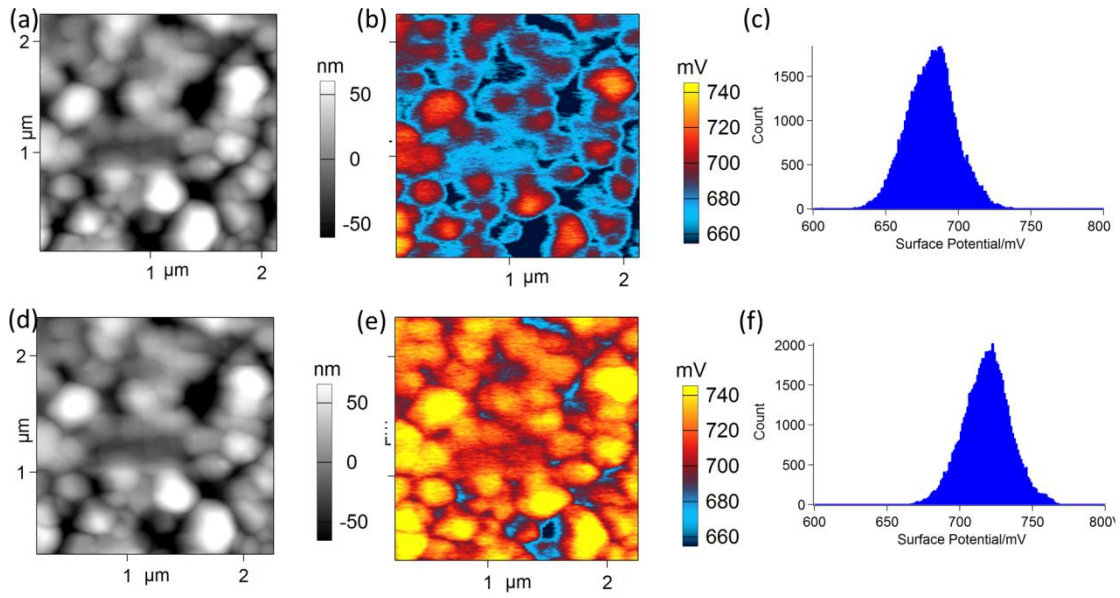

Figure 4.21 Change of surface potential distribution of CH3NH3PbI3 deposited on FTO/TiO2 substrate under continuous light illumination for 15mins, top row is first scan and bottom row is the scan after 15mins, showing the positive shift of surface potential distribution

4.2.4 *Photo-induced Ferroelectric Switching*

Now that I have individually studied the ferroelectric behavior of the films and how the light illumination changes the charge distribution in the system, it is worthwhile looking at how the light illumination interacts with the ferroelectric behavior.

Basically, we started with running a scan in dark environment, to map out the topography, PFM amplitude and phase response. Then, the 488nm blue laser is turned on for a few minutes to reach equilibrium before running another scan with the laser on. To make sure the results are not artifacts, multiple scans with laser on off sequence at different locations were recorded and compared. Interestingly, we found two contrasting behaviors when the light illuminates on the surface of the sample, summarized in figure 4.22-24. In all three figures, top row shows the mappings of topography, PFM amplitude, and phase in dark environment and the bottom row

shows corresponding mappings under 488nm laser illumination. The histogram comparison of PFM amplitude is also included. As can be seen in figure 4.22, when the 488nm blue laser is turned on, the phase mapping of the $CH_3NH_3PbI_3$ deposited on FTO/PEDOT:PSS substrate evolves, while the comparison of topography indicates that the probed region remains to be the same as in dark. Black domains (highlighted in white borderline) remain to be the same after light illumination, but many light brown domains switch to black ones, as indicated in figure 4.22(g), suggesting a 180˚ phase reversal. Due to different polarities of piezoresponse observed in the mapping, this phenomenon cannot be caused by the ionic motion and thus can be concluded to be caused by the polarization direction switching due to the light illumination. Associated with this switching, piezoresponse is also reduced, as indicated by comparison of the amplitude histogram distributions in dark and under illumination shown in figure 4.22(d,h). This suggests that light prefers one set of polarization over the other, presumably biased by the internal electric field due to the photovoltaic effect, though not all the domains are switched completely. And we also observe this photo-induced ferroelectric switching behavior in the $CH_3NH_3PbI_3$ film deposited on FTO/TiO_2 substrate, suggesting that this phenomenon is independent of the substrate effect, as can be seen in figure 4.23. In contrast, it is also observed that light does not switch the ferroelectric domain pattern at all, as shown in one of the comparison in figure 4.24, for which the piezoresponse amplitude does not change either.

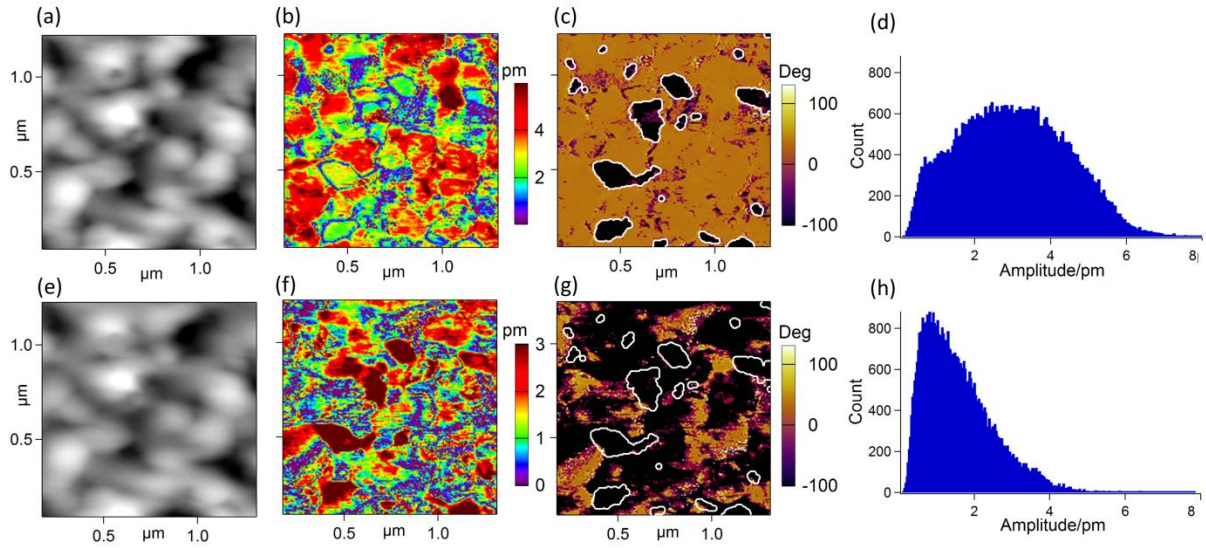

Figure 4.22 Photo-induced ferroelectric switching in $CH_3NH_3PbI_3$ film deposited on FTO/PEDOT:PSS substrate, top row is mapping under dark of (a) topography, (b) PFM amplitude, (c) phase, (d) amplitude histogram; and bottom row is corresponding mapping under laser illumination

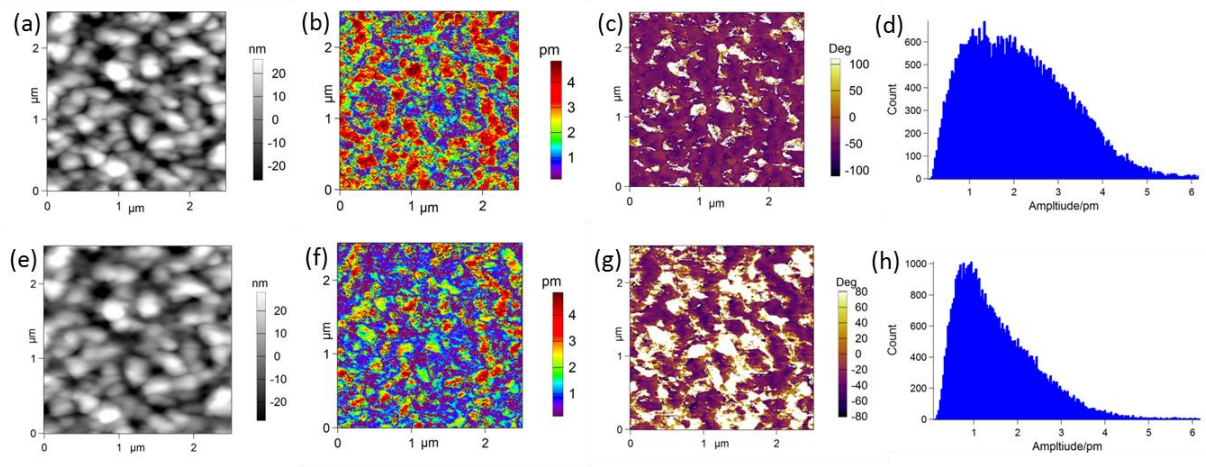

Figure 4.23 Photo-induced ferroelectric switching in CH3NH3PbI3 films deposited on FTO/TiO2 substrate, top row is mapping under dark of (a) topography, (b) PFM amplitude, (c) phase, (d) amplitude histogram; and bottom row is corresponding mapping under laser illumination

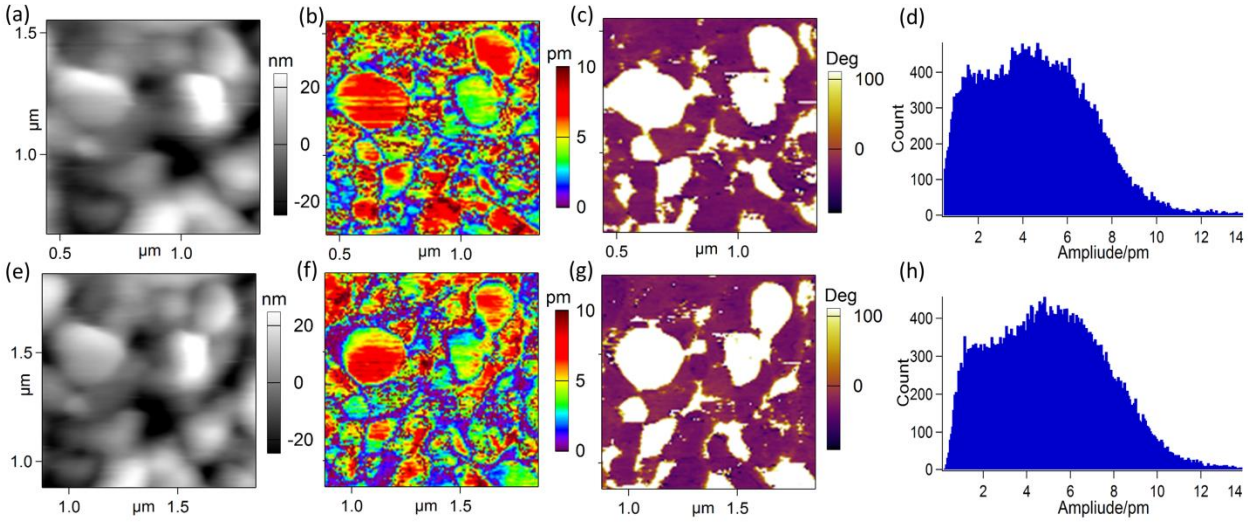

Figure 4.24 Photo-induced ferroelectric switching in $CH_3NH_3PbI_3$ film deposited on FTO/PEDOT:PSS substrate, top row is mapping under dark of (a) topography, (b) PFM amplitude, (c) phase, (d) amplitude histogram; and bottom row is corresponding mapping under laser illumination

4.3 Summary

In this chapter, we chose $CH_3NH_3PbI_3$, the first material system that exhibits excellent photovoltaic effect and decent ferroelectricity, to study its ferroelectric behavior and also the interplay between light illumination and the ferroelectric behavior.

With carefully designed PFM experiment and macroscopic ferroelectric testing, we are comfortable with the conclusion that the material is a decent ferroelectric material, though ionic motion also plays an important role in the microscopic measurement. The charge generation and separation process induced by light illumination is also clearly observed with KPFM measurement. Most importantly, the interactions between polarization and photo-induced charges are evident from our studies, that light illumination can switch ferroelectric polarization, and that polarization can affect surface charge and potential, which is in turn shifted by light

illumination. We believe that the underlying mechanisms of the interplay lie in the interaction between polarization and photovoltaic induced internal field, and the interaction between depolarization field and photo-induced charges. It's worth mentioning that the depolarization field can promote or impede the charge transport, which would enhance or reduce the photovoltaic performance. Though we are not able to provide any direct evidence that the ferroelectric behavior influences the photovoltaic conversion efficiency, we believe it plays an important role, based on the above discussions. However, the highly complicated interactions between ionic motion and polarization make it challenging to fully investigate this material using conventional AFM techniques. The recently developed scanning thermo-ionic microscopy [159] would be more suitable for studying more in depth the correlation of those two phenomena, wherein the Vegard strain from ionic motion can be separated from electromechanical piezoresponse.

Another important portion is to be able to combine the microscopic characterization using SPM and the macroscopic JV curve measurement, so that we can get better correlation between the device level performance and the microstructure level characterization and understanding. A simplified schematic is shown below in figure 4.25, where we have a think top electrode (Au layer) on top of the CH3NH3PbI3 surface, so that we have a complete perovskite solar cell structure to study. Besides, this structure also enables us to do a poling of the perovskite to align the ferroelectric polarization with externally applied large DC electric field, and then measure and correlate the device level performance and the microscopic ferroelectric domain structure, which will allow us determine whether or not the ferroelectricity contributes to the superior photovoltaic performance.

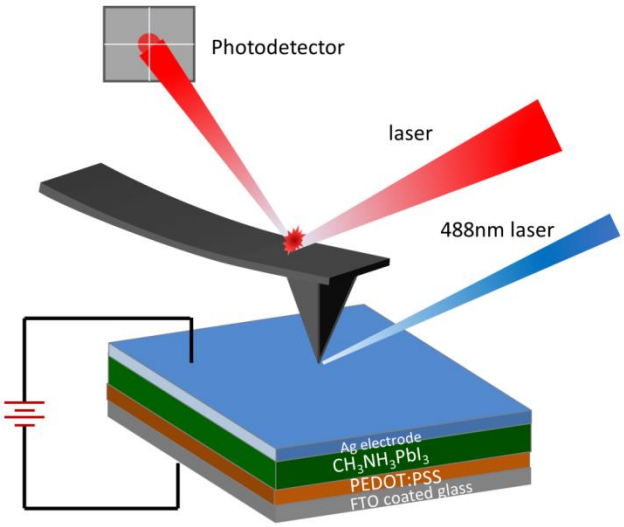

Figure 4.25 Simplified schematic of combining SPM characterization with device level macroscopic measurement

Chapter 5. RESISTIVE SWITCHING IN BIO-FERROELECTRICS

5.1 Motivation

It is mentioned in earlier chapter that we need to build lithium ion batteries with smaller volume and size but still provide more energy and power, in order to be suitable for the advanced portable consumer electronics. On the other hand, with the recent evolution in consumer electronics and the increasing need for more dense data storage, different types of non-volatile memories have been developed. In particular, resistive random access memory (ReRAM) is considered quite promising due to its high speed, long retention time, good endurance, low operating voltage, and high scalability [160-162]. This advanced ReRAM functions based on reliable resistive switching behaviors, which have been found in various materials including the well-studied transition metal oxides such as titanium oxide [163] and vanadium oxide [164], and also in more recent discovery ferroelectric perovskites such as lead zirconate titanate (PZT) [165]. The basic characteristic of RRAM is its two different resistance states, i.e. high resistance state (HRS) and low resistance state (LRS), which can be switched from one to the other by an external electric stimulus, as illustrated schematically in figure 5.1.

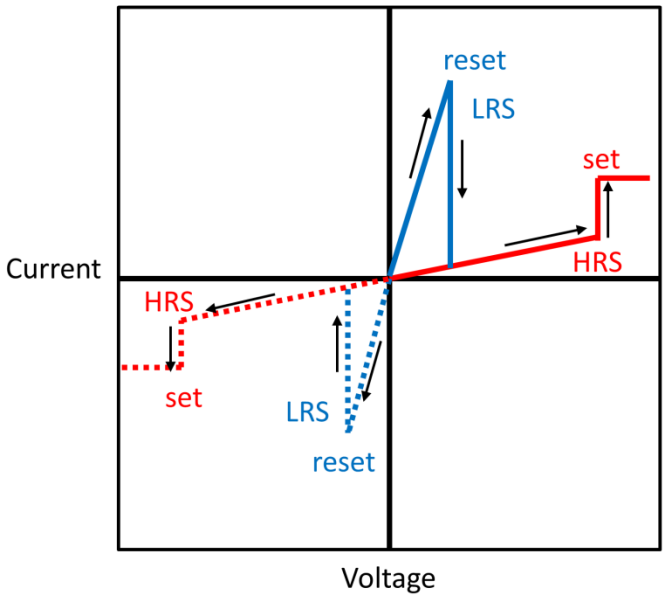

Figure 5.1 Simplified current-voltage characteristics of resistive switching behavior

In transition metal oxides, recent studies suggest that there are two different underlying mechanisms to form the conducting filament [166], which are redox reaction induced metallic filament and oxygen vacancy electro-migration induced filament, as shown in figure 5.2. The first mechanism involves a process where electrochemically active metal gets oxidized to mobile metal ions, migrate to the other electrode, and gets reduced back. This redox reaction process leads to a continuous growth of the metal protrusion and the formation of conducting metallic filament eventually. For the later mechanism, oxygen ions migrate to one electrode while the charged oxygen vacancies migrate to the other electrode, and the accumulation of oxygen vacancies form the conducting filament. Despite the fact that there has been lots of effort on improving both the understanding and the performance of transition metal oxides in ReRAM application, there is always concern for the memory reliability because the resistive switching process induces chemical alternation of the materials. While on the other hand, since the polarization reversal resistive switching process of ferroelectrics is intrinsically fast and does not

involve any chemical composition or phase change, ferroelectric resistive switching is thus promising and attracts lots of attention.

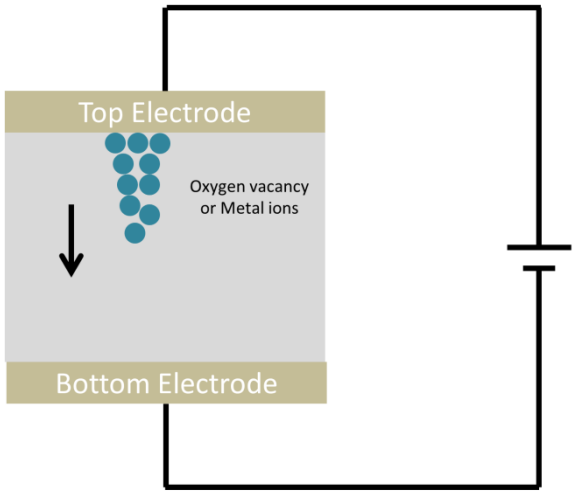

Figure 5.2 Schematic of the conducting filament in transition metal oxide

Here, instead of studying the inorganic ferroelectric ceramics, we are more interested in biological ferroelectric tissue elastin and also its nanostructured component tropoelastin, whose ferroelectricity has recently been revealed by our group's previous work [167-169]. Compared to those bulk ferroelectric perovskite oxides, these biological molecular ferroelectrics are typically soft, lightweight, environmentally friendly and more importantly biocompatible. In addition, they can be processed at relatively lower temperatures and fabricated onto soft substrates for a wide range of applications [170].

5.2 Sample Preparation and Ferroelectricity

5.2.1 *Sample Preparation*

There are two different samples that we studied in this work: elastin and tropoelastin. Elastin is an intriguing extracellular matrix protein that can be found in connective tissues of vertebrates [171], and all mammals rely on elastin to convey elasticity to their tissues [172]. Elastin is

constructed by the hierarchical assembly and cross-linking of many tropoelastin monomers which accumulate on a microfibrillar skeleton [173]. Tropoelastin is a water-soluble molecule with a molecular weight of about 72,000 daltons. It serves as a component of rigidly organized assemblies, and enables the formation of dynamically distensible elastic tissues.

In our experiment, elastin samples were provided by our collaborator Yunjie and Prof.Zhang and obtained using cyanogen bromide treatment to remove cells, collagen, and other ECM components of the porcine thoracic aortas which were harvested from a local abattoir. Details of the elastin sample preparation process can be found in previous work [167]. To prepare for substantial PFM experiments, the elastin samples were cut into 1*1 mm^2 size pieces and embedded in epoxy/resin, which was then dried at 60 ˚C overnight for a full polymerization process to occur. Then the embedded elastin sample was mounted on a microtome cutting stage and trimmed using a fresh glass knife into slices of different thicknesses (100 nm and 1 μm) which were then picked up and fixed onto Au coated Si substrate. Shown below are the optical microscope images of the elastin slices with different thickness.

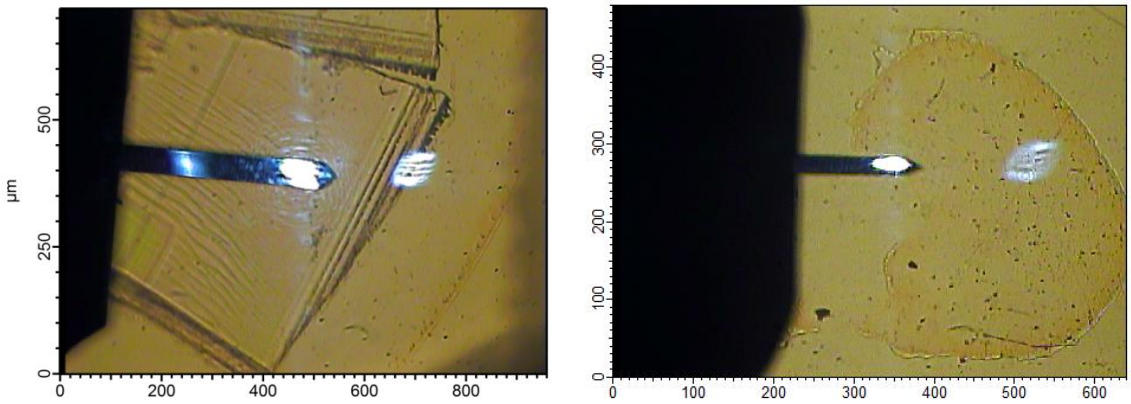

Figure 5.3 Optical microscope images of 1 μm (left) and 100 nm (right) elastin slice

For tropoelastin sample preparation, the tropoelastin monomers were purchased from Advanced BioMatrix in the form of sterile, lyophilized powder. The powder was mixed with

0.25vol% glacial acetic acid diluted with deionized water, to form a desired concentration of 50 μg/ml. Then the homogeneous solution was drop casted onto a piece of Au coated Si substrate, followed by an overnight drying process, which concludes the sample prep process for following measurement.

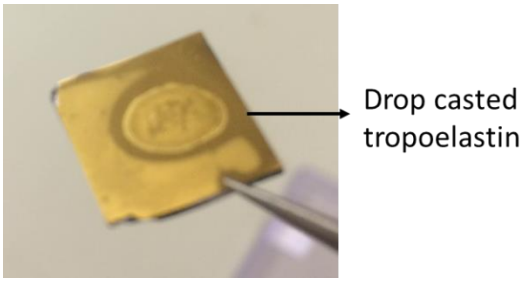

Figure 5.4 Photo of the drop-casted tropoelastin sample

5.2.2 *Ferroelectricity Measurement*

Before doing the electrical conductivity measurement, the ferroelectricity characterization was first conducted on the elastin slices to check whether the sample preparation process has any influences on its ferroelectric properties. The sample measured here is 1 μm elastin slice deposited on Au coated Si substrate using dual amplitude resonance tracking piezoresponse force microscopy (DART-PFM) and also switching spectroscopy piezoresponse force microscopy (SSPFM). Shown on the left part of figure 5.5 is the scan of surface topography over an area of 2*2 μm^2, and on the right is the amplitude of piezoresponse, caused by the 5V external AC voltage excitation. The amplitude shown here is corrected using the damped driven harmonic oscillator model, leading to an estimate of piezoelectric coefficient on the order of about 1 pm/V, which is comparable with reported values on the pristine elastin samples [169] and other tissues [174].

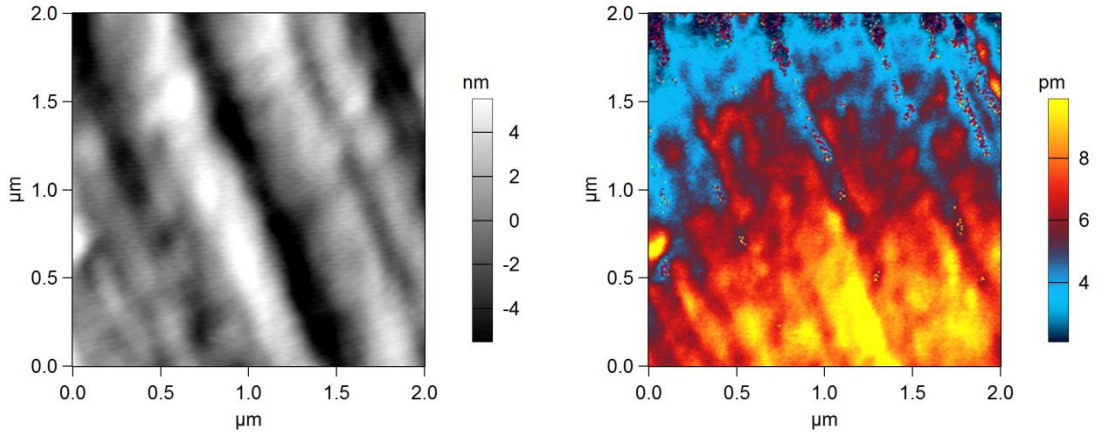

Figure 5.5 DART-PFM mapping of elastin, topography on the left and piezoresponse amplitude on the right

The PFM mapping confirms that there is spontaneous polarization in the elastin slice that responds to the external applied electric field. Then the remaining question is whether this spontaneous polarization can be manipulated or switched by a large external electric field, which leads to the SSPFM experiment. As can be seen from the results below, when the DC voltage exceeds 100V, the phase response alters by 180 ˚, indicating that the polarization reversal occurs. Associated with the 180 ˚ phase contrast, amplitude-voltage butterfly loop is also observed. This set of measurement suggests that the prepared elastin slices still possess ferroelectricity. The asymmetry in the loops especially in the amplitude-voltage butterfly loop is possibly a result of the internal electric field due to the ferroelectricity. Only one set of data is shown in figure 4.5 but I do obtained similar behaviors across different locations in one sample and also among multiple samples.

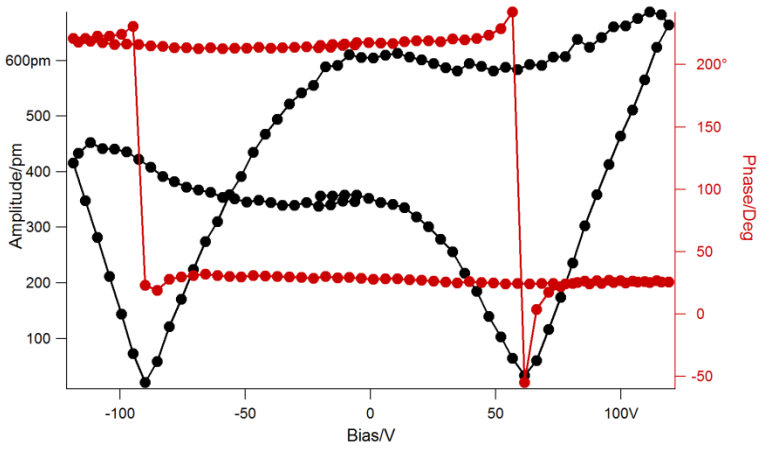

Figure 5.6 SSPFM ferroelectric hysteresis loop of elastin

5.3 Resistive Switching Measurement

Before diving into the electrical conductivity measurement of the elastin and tropoelastin samples, I measured the electrical conductivity of the substrates to exclude any possible crosstalk for future data analysis.

Using conductive-AFM, we can measure the current response when applying a DC bias onto the sample surface. Below in figure 5.7 shows the collected current response when applying a DC bias sweep from -500mV to 500mV onto the Au coated Si substrate. As can be clearly, the current response is larger than 100nA, which exceeds the conductive-AFM detection range. This high electrical conductivity is due to the Au layer on top with a thickness of about 100nm.

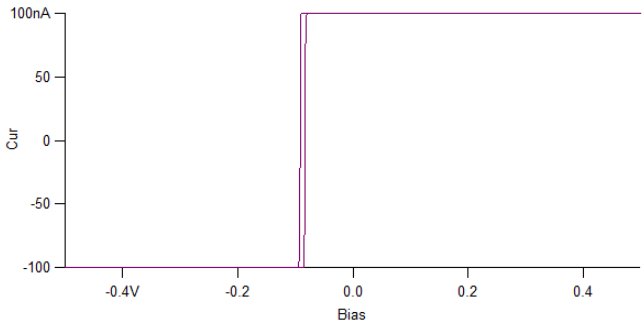

Figure 5.7 Current-voltage characteristics of Au coated Si substrate

Using the same setup, I also measured the current response of another control sample, as displayed below in figure 5.8. The control sample is fabricated by drop casting the diluted glacial acetic acid onto the Au coated Si substrate and then drying overnight. This is to exclude any possible crosstalk caused by this chemical. The DC voltage is increased to 8V but the system is still not able to pick up any current response signal. Also, since the measurement system limits the max applied DC voltage to 10V, I am confident that the acetic acid won't contribute to any current response in future measurement on tropoelastin.

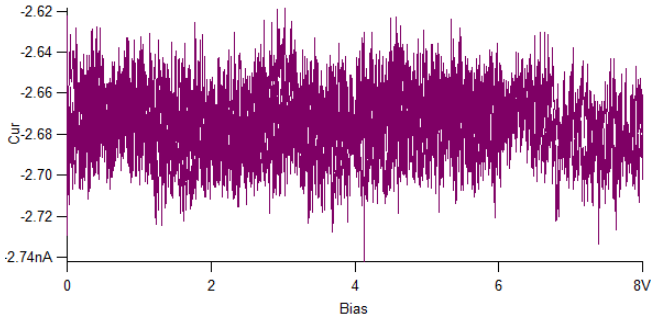

Figure 5.8 Current-voltage characteristics of glacial acetic acid drop casted on Au coated Si substrate

5.3.1 *Current Mapping*

We first examined the current mapping of the elastin slices using conductive AFM, which allows simultaneous mapping of surface topography and current distribution when subjected to external DC voltages. Both 1 μm thick and 100 nm thick elastin slices are measured using the same configuration. However, due to the hardware limitation of the 10 V maximum DC voltage, we were not able to get any current response on the 1 μm thick elastin slice. For the 100 nm thick sample, under a positive sample bias of 5V, relatively large current response on the order of 10 nA is observed over a 1*1 μm^2 area, as can be seen figure 5.9a below. When the sample bias is reversed to negative 5V, the current is reduced by orders of magnitude, to the background noise

level of pA (shown in the right image below), making it essentially non-conducting. Histogram statistics of the current response under positive 5V surface bias as shown in figure 5.10, suggests that approximately 43.3% area exhibiting relatively large current around 20 nA, and the remaining ones showing much smaller current value of lower than 100 pA. In addition, the few hot spots with slightly higher current response in figure 5.9b fall into the low conductance region of figure 5.9a. This strong asymmetry observed in current mapping under positive and negative surface biases suggests a diode-like conducting behavior of elastin. Therefore, I continued the study with measuring local current-voltage characteristics (IV curves) by sweeping the DC bias using c-AFM.

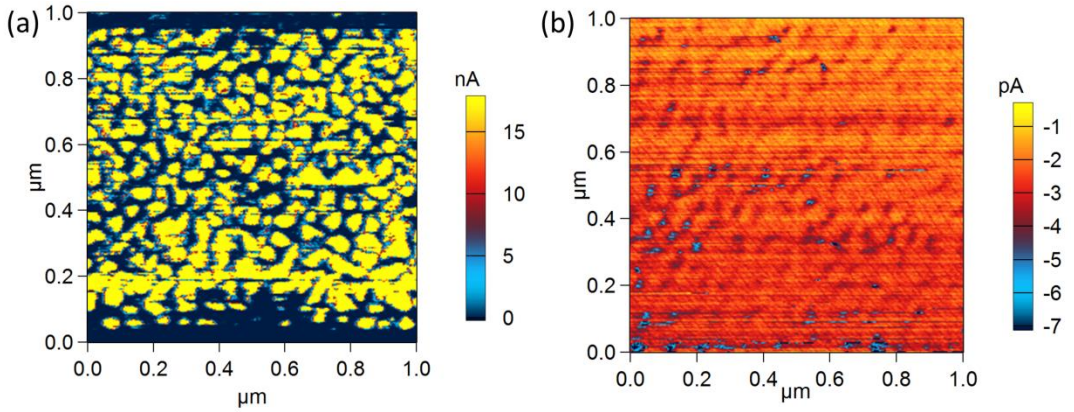

Figure 5.9 Current mappings of elastin under positive (a) and negative (b) surface bias

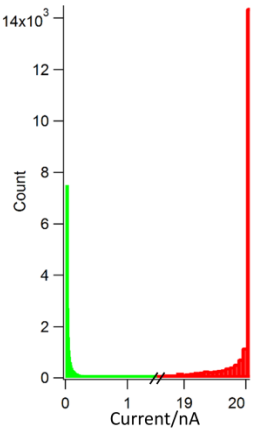

Figure 5.10 Histogram statistics of the current mapping of elastin under 5V surface bias

5.3.2 *Current-voltage Characteristics*

To further verify this diode-like conducting behavior, local current voltage characteristics measurement was carried out on the 100nm thick elastin samples as well. Typically, DC voltage in triangular waveform is applied to the sample surface and the corresponding current response is collected. We found two distinct current-voltage behaviors measured at different locations across the sample, as summarized in figure 5.11. Statistically, more probed locations behave similar to what is summarized in figure 5.11a, showing a positive current polarity. There are some locations, however, exhibit the opposite current polarity, with forward current under negative sample bias, as displayed in figure 5.11b. For the data reliability, the IV curve measurement was repeated on multiple locations and also on different samples. Statistical analysis of all the measurement is summarized in figure 5.12, and the density color bar reflects the total count. It is clear that more data points (about 64%) exhibit positive current polarity; though the critical bias to set the current varies from location to location.

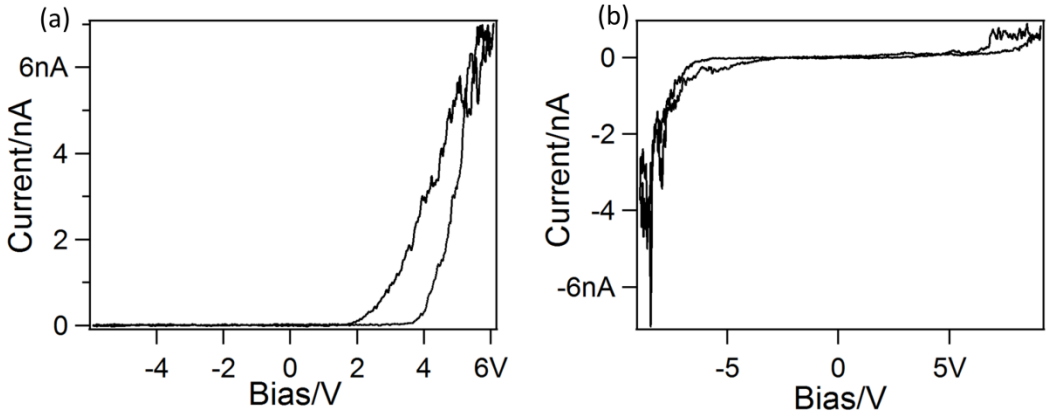

Figure 5.11 Local IV curves of elastin showing diode behavior

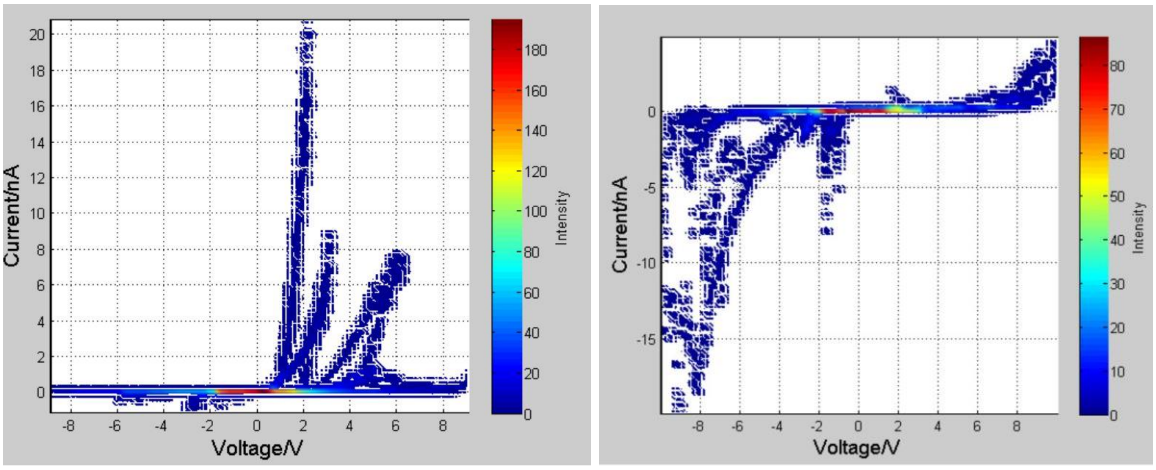

Figure 5.12 Density mapping of the IV curve statistics of elastin

After confirming the diode-like conducting behavior in elastin, we also studied tropoelastin, using the same experiment setup. Not to our surprise, such diode-like behavior of elastin is well preserved at the monomer level. As can be seen in figure 5.13, both positive and negative current polarities are observed in tropoelastin samples. Similarly, the data reliability is checked by repeating the measurement on multiple random locations and also on different samples. The relative proportions of positive and negative current polarities observed in tropoelastin are revealed by the intensity mapping in figure 5.14, with approximately 88% of total points probed in tropoelastin showing positive current polarity.

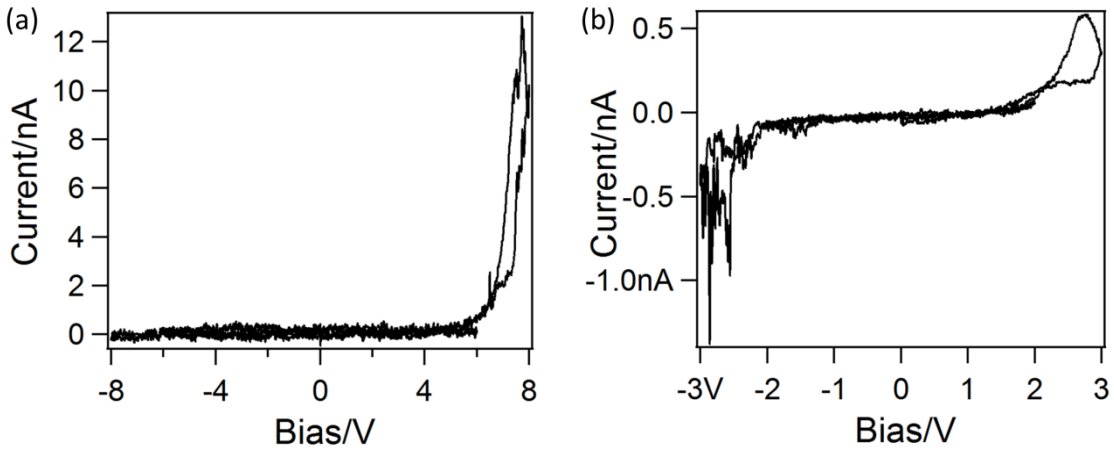

Figure 5.13 Local IV curves of tropoelastin showing diode behavior

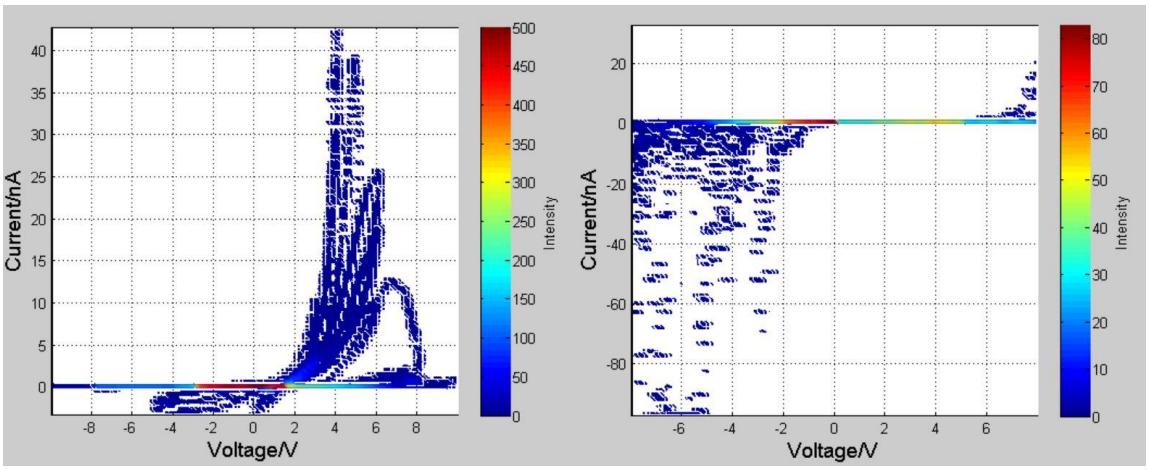

Figure 5.14 Density mapping of the IV curve statistics of tropoelastin

5.3.3 *Ferroelectric Resistive Switching*

Based on the observation of diode-like conducting behaviors in both tropoelastin and elastin samples, and also our previous observation of the intrinsic ferroelectricity, we hypothesize that this conducting behavior is related to the sample's spontaneous polarization, which can be manipulated with either mechanical force or large external electrical field.

To validate this hypothesis, we first examined whether or not large external electrical field can alter the current polarity. With the 100nm thick elastin samples, as shown in figure 5.16a, it shows typical positive current polarity under relatively smaller bias up to ±8V. However, once the applied bias is increased to ±10V, the current polarity is switched, showing forward current under negative surface bias. Similar polarity switching phenomenon is also observed in tropoelastin samples when the applied bias is increased from ±6V to ±8V, as shown in figure 5.16b. While we do not have direct experimental evidence, the critical voltage to switch the current polarity is on the same order of magnitude of the coercive threshold for polarization reversal in elastin and tropoelastin as previously reported [167-169], suggesting that the switching of conductance is indeed associated with polarization reversal.

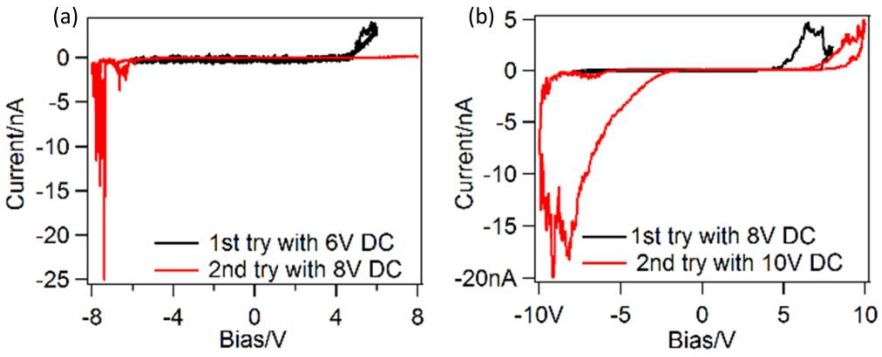

Figure 5.15 Switchable diode behavior of (a) elastin and (b) tropoelastin by external electric field

As mentioned earlier, it is well known that the ferroelectric polarization can also be switched by stress. Thus we may manipulate the current polarity by applying large mechanical force as well. Toward this end, we measured the IV curves of the same location subjecting to different contact forces imposed by the c-AFM probe. In order to first quantify the mechanical force that the c-AFM probe imposes on the sample surface, a set of calibration was performed described as follows. Firstly, the optical lever sensitivity was characterized by bringing the probe in contact with a rigid surface, which was clean glass slide in our case, and then moving a certain distance. The AFM system will record the corresponding force curve plotting the cantilever deflection with respect to the distance, whose slope yields the optical lever sensitivity with the value of 89.89 pm/V averaged over multiple calibration cycles. Then, the spring constant of the probe needs to be calibrated. This calibration step was realized by capturing thermal data, which is a built-in function of the Asylum Research software. By fitting the captured data, the spring constant can be calculated to be 2.27 nN/nm based on the simplified damped driven harmonic oscillator model. Finally, with calibrated optical lever sensitivity and spring constant, the mechanical force applied can be calculated by multiplying those two with the difference between

the set point and initial deflection value, which is the knob parameter that we change during the measurement. It is worth mentioning that each probe could vary slightly, therefore, I performed the same calibration procedure every time a new probe was used.

It is always observed in both elastin and tropoelastin samples that the current response will initially increase with the increasing mechanical force applied on the sample, shown in figure 5.16, benefitting from better physical contact between the tiny probe and the sample surface and thus less contact resistance. A representative data set of how the mechanical force changes the conductance behavior of both samples is shown in figure 5.17. For example, in the 100nm thick elastin sample with an initial state of positive current polarity, the current initially increases when the mechanical force is increased from 100 nN to 1 μN, due to better electric contact under larger force. Then, when the mechanical force is increased further to 2.1 μN, the IV curve changes and the current polarity is switched, with current response under negative bias substantially higher. Even more interesting is that when the mechanical force is reduced to 170 nN, the current polarity is restored back to its initial state, suggesting a reversible ferroelectric resistive switching process under large mechanical force. Similar phenomenon is observed in tropoelastin as well, as plotted in figure 5.17b.

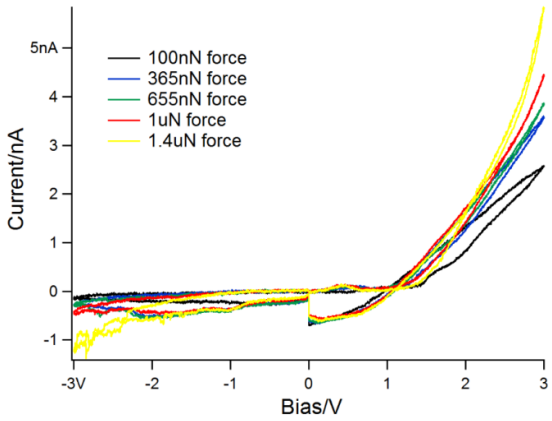

Figure 5.16 IV curves under increasing mechanical force, showing increasing current response

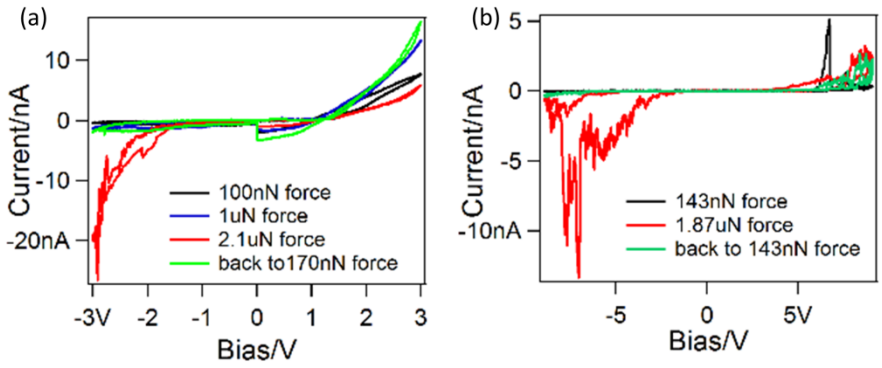

Figure 5.17 Switchable diode behavior of (a) elastin and (b) tropoelastin by mechanical force

5.4 Summary

Conductive-AFM has been demonstrated as a powerful tool, capable of characterizing both local conductance behavior on the nanoscale and correlating the material structure with the electrical conductivity. In this chapter, we first studied thoroughly the electrical conductance characteristics of both elastin and tropoelastin using c-AFM and revealed its diode-like conductance behavior. Besides, the diode-like conductance behavior is not uniform across the sample and varies from location to location. The ferroelectric property of the biological tissue samples is also investigated using PFM, and solid proof of spontaneous polarization that can be

reversed by external electric field has been established. Combining the results of the electrical conductance behavior and the ferroelectric property together, we came up with the hypothesis that the diode-like conductance behavior is strongly related to the spontaneous polarization direction of the material. The best way to validate such hypothesis is to carry out simultaneous PFM ferroelectric domain mapping and c-AFM current mapping on the same location, which cannot be realized at current stage due to hardware limitations. Therefore, in order to validate this hypothesis, we came up with alternative way, that is to investigate the influence of large external electric field and large mechanical force applied by the probe on the conductance behavior. What we found is that both large external applied electric field and large mechanical force interaction can switch the current polarity direction. In particular, the current polarity switching induced by mechanical force interaction is a reversible and nondestructive process, meaning the current polarity can restore once the mechanical force is reduced, which could benefit potential application. Based on those findings together, we believe this diode-like conductance behavior is an intrinsic property of bio-ferroelectrics elastin and tropoelastin, and the switchable current polarity belongs to ferroelectric resistive switching, suggesting promising application of those biological tissues in soft, bio-compatible ReRAMs and other field as well.

Chapter 6. CONCLUSIONS AND FUTURE WORK

6.1 Conclusions

The work discussed in this dissertation includes the synthesis and thorough characterization of nanostructured carbon materials and synthetic and biological ferroelectrics for various applications.

In chapter 2, the work on fabricating carbon nanofibers with optimized porous structures via electrospinning and post thermal treatment process for the application of lithium ion battery anode is presented. In this work, an environmentally friendly and easier to process thermal plastic polymer is used as carbon precursor, which requires the identification of appropriate thermal treatment process to carbonize the polymer while maintaining the morphology. With the help of thermal analysis tools and structure characterization tools, an optimized heat treatment process is identified, to carbonize the polymer fiber as well as generate a great amount of micropores and mesopores. Those porous carbon nanofibers are tested as anode materials in a lithium ion battery cell, showing that the micropores and mesopores can function as lithium ion reservoirs, and thus can help enhance the capacity performance. Chapter 3 is a continuation of the research presented in chapter 2, focuses more on developing alternative and better structure for lithium ion battery application, while still keeping the same polymer precursor and same heat treatment conditions. Here, nanoimprint lithography, a technique capable of creating patterned structure with the feature size down to a few nanometers, is used to pattern the PVP polymer films. Using the same heat treatment process identified in chapter 2, the patterned structure was well maintained in the final carbon film. When testing in a lithium ion battery cell, the patterned carbon film shows much improved volumetric capacity performance, compared to control samples without patterned structure and also to graphite.

The characterization part of synthetic and biological ferroelectrics starts is covered in chapter 4 and 5. In chapter 4, the main topic is the characterization of synthetic ferroelectrics, which is considered the most promising light absorber material for the next generation solar cells. Mainly the focus is to first establish solid proof of the intrinsic ferroelectric property of the organic-inorganic halide perovskite $CH_3NH_3PbI_3$, and also study the interactions between the ferroelectricity and the light illumination. With carefully designed experiments both microscopically using PFM and macroscopically using ferroelectric tester, we show that $CH_3NH_3PbI_3$ is indeed a ferroelectrics, despite its structure instability. Then, we also investigated how the light illumination changes the behavior of the perovskite. In addition to the charge generation and separation process that we observed using KPFM, we also found an interest phenomenon that under certain circumstances, light illumination could alter the ferroelectric domain pattern of the material, preferring one orientation over the other. This set of findings has raised more questions about the perovskite material to help further improve its application capability.

The last chapter talks about the work done on biological ferroelectric tissues elastin and tropoelastin. We have experimentally demonstrated that the diode-like electrical conductance behavior exists in both samples, and that such behavior is strongly related to the ferroelectric polarization. It is also proved that the diode-like conductance behavior and the current polarity can be switched by either large external applied electric field or by large mechanical force applied onto the sample surface. Besides, it is worth mentioning that the ferroelectric polarization can also be switched by those two parameters above, thus suggesting the electrical conductance behavior is closely related to the ferroelectric polarization. Combining PFM and c-

AFM measurement together, we are able to provide experimental evidence of the reversible and non-destructive ferroelectric resistive switching behavior of the biological tissues.

6.2 The Future Work

It is certain that the nanostructured carbon is a promising material candidate for energy storage applications including lithium ion battery, lithium sulfur battery, and so on. However, the two different material structures that I synthesized need to be further improved for practical applications. One drawback of the nanostructured carbon is that even though it contains micropores and mesopores, those pores are not homogeneous. Therefore, to further improve the quality of the nanostructured carbon, certain actions need to be taken for a better control over the pore distribution, for example, the template synthesis route using silica nanospheres as the sacrificial template. Also, the current carbon yield is around 10%, which is relatively low and needs to be improved by fine tuning the heat treatment process to reduce the carbon loss.

For the characterization part, even though scanning probe microscopy has been demonstrated as a powerful tool to probe the localized response to different stimuli, such as electric field, and magnetic field, the SPM system still needs some modification to make it more robust and powerful. For example, it has been demonstrated electrochemical strain microscopy is capable of probing the localized ion motion in battery electrodes and electrolytes. However, it is really difficult to quantitate the ESM characterization and one major reason is that the probed volume is too small. Also, there have been arguments around PFM and ESM for years on how to differentiate multiple electromechanical coupling mechanisms to better analyze the data. Some preliminary work has been done to show a few ways to help distinguish. However, there are more factors affecting the results to be considered.

On the other hand, in order to better characterize and understand material properties, certain modules of the SPM system should be combined together, enabling a simultaneous measurement. For example, in chapter 4, it would be really beneficial if PFM and c-AFM can run together to map out both the current distribution and the ferroelectric domain pattern in the biological tissues, which could provide a direct proof of the correlation between the ferroelectricity and the resistive switching behavior.

REFERENCES

1. Arico, A.S., et al., *Nanostructured materials for advanced energy conversion and storage devices.* Nature Materials, 2005. **4**(5): p. 366-377.
2. Su, D.S. and R. Schlogl, *Nanostructured Carbon and Carbon Nanocomposites for Electrochemical Energy Storage Applications.* Chemsuschem, 2010. **3**(2): p. 136-168.
3. Zou, M., et al., *Synthesis of High-Voltage (4.5 V) Cycling Doped LiCoO2 for Use in Lithium Rechargeable Cells.* Chemistry of Materials, 2003. **15**(25): p. 4699-4702.
4. Chan, C.K., et al., *High-performance lithium battery anodes using silicon nanowires.* Nature Nanotechnology, 2008. **3**(1): p. 31-35.
5. Zhang, W.M., et al., *Tin-nanoparticles encapsulated in elastic hollow carbon spheres for high-performance anode material in lithium-ion batteries.* Advanced Materials, 2008. **20**(6): p. 1160-+.
6. Wang, J., et al., *Three-Dimensionally Mesostructured Fe2O3 Electrodes with Good Rate Performance and Reduced Voltage Hysteresis.* Chemistry of Materials, 2015. **27**(8): p. 2803-2811.
7. Wang, D.H., et al., *Self-Assembled TiO2-Graphene Hybrid Nanostructures for Enhanced Li-Ion Insertion.* Acs Nano, 2009. **3**(4): p. 907-914.
8. Rui, X.H., et al., *Olivine-Type Nanosheets for Lithium Ion Battery Cathodes.* Acs Nano, 2013. **7**(6): p. 5637-5646.
9. Li, X.X., et al., *Template-synthesized LiCoO2, LiMn2O4, and LiNi0.8Co0.2O2 nanotubes as the cathode materials of lithium ion batteries.* Journal of Physical Chemistry B, 2005. **109**(29): p. 14017-14024.
10. Gu, M., et al., *In Situ TEM Study of Lithiation Behavior of Silicon Nanoparticles Attached to and Embedded in a Carbon Matrix.* Acs Nano, 2012. **6**(9): p. 8439-8447.
11. Balke, N., et al., *Real Space Mapping of Li-Ion Transport in Amorphous Si Anodes with Nanometer Resolution.* Nano Letters, 2010. **10**(9): p. 3420-3425.
12. Balke, N., et al., *Nanoscale mapping of ion diffusion in a lithium-ion battery cathode.* Nature Nanotechnology, 2010. **5**(10): p. 749-754.

13. Balke, N., et al., *Imaging Li-Ion Dynamics in Energy Storage Materials on the Nanometer Scales.* Microscopy and Microanalysis, 2010. **16**(Supplement S2): p. 1814-1815.
14. Bruce, P.G., B. Scrosati, and J.M. Tarascon, *Nanomaterials for rechargeable lithium batteries.* Angewandte Chemie-International Edition, 2008. **47**(16): p. 2930-2946.
15. Whittingham, M.S., *Electrical Energy-Storage and Intercalation Chemistry.* Science, 1976. **192**(4244): p. 1126-1127.
16. Liu, C., et al., *Advanced Materials for Energy Storage.* Advanced Materials, 2010. **22**(8): p. E28-E62.
17. Besenhard, J.O. and M. Winter, *Advances in battery technology: rechargeable magnesium batteries and novel negative-electrode materials for lithium ion batteries.* Chemphyschem, 2002. **3**(2): p. 155-9.
18. Walter van Schalkwijk, B.S., *Advances in Lithium-Ion Batteries*2002: Springer.
19. Sato, K., et al., *A Mechanism of Lithium Storage in Disordered Carbons.* Science, 1994. **264**(5158): p. 556-558.
20. Imanishi, N., Y. Takeda, and O. Yamamoto, *Development of the Carbon Anode in Lithium Ion Batteries*, in *Lithium Ion Batteries*2007, Wiley-VCH Verlag GmbH. p. 98-126.
21. Zheng, T., W. Xing, and J.R. Dahn, *Carbons prepared from coals for anodes of lithium-ion cells.* Carbon, 1996. **34**(12): p. 1501-1507.
22. Dai, L.M., et al., *Carbon Nanomaterials for Advanced Energy Conversion and Storage.* Small, 2012. **8**(8): p. 1130-1166.
23. Becquerel, A., *Recherches sur les effets de la radiation chimique de la lumiere solaire au moyen des courants electriques.* Comptes rendus de lÁcademie des sciences, 1839. **9**: p. 145-149.
24. Kojima, A., et al., *Organometal Halide Perovskites as Visible-Light Sensitizers for Photovoltaic Cells.* Journal of the American Chemical Society, 2009. **131**(17): p. 6050-6051.
25. *Best Research Cell Efficiencies*. 2016.
26. Green, M.A., et al., *Solar cell efficiency tables (version 47).* Progress in Photovoltaics: Research and Applications, 2016. **24**(1): p. 3-11.

27. Stranks, S.D. and H.J. Snaith, *Metal-halide perovskites for photovoltaic and light-emitting devices.* Nat Nano, 2015. **10**(5): p. 391-402.
28. Bai, S., Y. Jin, and F. Gao, *Organometal Halide Perovskites for Photovoltaic Applications*, in *Advanced Functional Materials*2015, John Wiley & Sons, Inc. p. 535-566.
29. Eperon, G.E., et al., *Formamidinium lead trihalide: a broadly tunable perovskite for efficient planar heterojunction solar cells.* Energy & Environmental Science, 2014. **7**(3): p. 982-988.
30. Jeon, N.J., et al., *Compositional engineering of perovskite materials for high-performance solar cells.* Nature, 2015. **517**(7535): p. 476-+.
31. Meng, L., et al., *Recent Advances in the Inverted Planar Structure of Perovskite Solar Cells.* Accounts of Chemical Research, 2016. **49**(1): p. 155-165.
32. Seo, J., J.H. Noh, and S.I. Seok, *Rational Strategies for Efficient Perovskite Solar Cells.* Accounts of Chemical Research, 2016. **49**(3): p. 562-572.
33. Unger, E.L., et al., *Hysteresis and transient behavior in current-voltage measurements of hybrid-perovskite absorber solar cells.* Energy & Environmental Science, 2014. **7**(11): p. 3690-3698.
34. Tress, W., et al., *Understanding the rate-dependent J-V hysteresis, slow time component, and aging in CH3NH3PbI3 perovskite solar cells: the role of a compensated electric field.* Energy & Environmental Science, 2015. **8**(3): p. 995-1004.
35. Xiong, J., et al., *Interface degradation of perovskite solar cells and its modification using an annealing-free TiO2 NPs layer.* Organic Electronics, 2016. **30**: p. 30-35.
36. Berhe, T.A., et al., *Organometal halide perovskite solar cells: degradation and stability.* Energy & Environmental Science, 2016. **9**(2): p. 323-356.
37. Tohge, N., S. Takahashi, and T. Minami, *Preparation of PbZrO3–PbTiO3 Ferroelectric Thin Films by the Sol–Gel Process.* Journal of the American Ceramic Society, 1991. **74**(1): p. 67-71.
38. Fan, Z., et al., *Ferroelectricity of CH3NH3PbI3 Perovskite.* The Journal of Physical Chemistry Letters, 2015. **6**(7): p. 1155-1161.

39. Kutes, Y., et al., *Direct Observation of Ferroelectric Domains in Solution-Processed CH3NH3PbI3 Perovskite Thin Films.* Journal of Physical Chemistry Letters, 2014. **5**(19): p. 3335-3339.
40. Beilsten-Edmands, J., et al., *Non-ferroelectric nature of the conductance hysteresis in CH3NH3PbI3 perovskite-based photovoltaic devices.* Applied Physics Letters, 2015. **106**(17): p. 173502.
41. Frost, J.M., et al., *Atomistic origins of high-performance in hybrid halide perovskite solar cells.* NanoLetters, 2014. **14**(5): p. 2584-90.
42. Zheng, F., et al., *First-Principles Calculation of the Bulk Photovoltaic Effect in CH3NH3PbI3 and CH3NH3PbI3-xClx.* Journal of Physical Chemistry Letters, 2015. **6**(1): p. 31-37.
43. Liao, W.Q., et al., *A lead-halide perovskite molecular ferroelectric semiconductor.* Nature Communications, 2015. **6**: p. 7338.
44. Zhao, P.J., et al., *Spontaneous polarization behaviors in hybrid halide perovskite film.* Scripta Materialia, 2015. **102**: p. 51-54.
45. Seol, D., et al., *Screening effect on photovoltaic performance in ferroelectric CH3NH3PbI3 perovskite thin films.* Journal of Materials Chemistry A, 2015. **3**(40): p. 20352-20358.
46. Xiao, Z.G., et al., *Giant switchable photovoltaic effect in organometal trihalide perovskite devices.* Nature Materials, 2015. **14**(2): p. 193-198.
47. Wei, J., et al., *Hysteresis Analysis Based on the Ferroelectric Effect in Hybrid Perovskite Solar Cells.* Journal of Physical Chemistry Letters, 2014. **5**(21): p. 3937-3945.
48. Frost, J.M., K.T. Butler, and A. Walsh, *Molecular ferroelectric contributions to anomalous hysteresis in hybrid perovskite solar cells.* APL Materials, 2014. **2**(8): p. 081506.
49. Liu, S., et al., *Ferroelectric Domain Wall Induced Band Gap Reduction and Charge Separation in Organometal Halide Perovskites.* Journal of Physical Chemistry Letters, 2015. **6**(4): p. 693-699.
50. Dawber, M., K.M. Rabe, and J.F. Scott, *Physics of thin-film ferroelectric oxides.* Reviews of Modern Physics, 2005. **77**(4): p. 1083-1130.

51. Setter, N., et al., *Ferroelectric thin films: Review of materials, properties, and applications.* Journal of Applied Physics, 2006. **100**(5): p. 051606.
52. Moazzami, R., C. Hu, and W.H. Shepherd, *Electrical characteristics of ferroelectric PZT thin films for DRAM applications.* Ieee Transactions on Electron Devices, 1992. **39**(9): p. 2044-2049.
53. Lovinger, A.J., *Ferroelectric Polymers.* Science, 1983. **220**(4602): p. 1115-1121.
54. Choi, T., et al., *Switchable Ferroelectric Diode and Photovoltaic Effect in BiFeO3.* Science, 2009. **324**(5923): p. 63-66.
55. Yang, J.J., et al., *Memristive switching mechanism for metal//oxide//metal nanodevices.* Nat Nano, 2008. **3**(7): p. 429-433.
56. Lee, J.S., S. Lee, and T.W. Noh, *Resistive switching phenomena: A review of statistical physics approaches.* Applied Physics Reviews, 2015. **2**(3): p. 031303.
57. Doo Seok, J., et al., *Emerging memories: resistive switching mechanisms and current status.* Reports on Progress in Physics, 2012. **75**(7): p. 076502.
58. Binnig, G., C.F. Quate, and C. Gerber, *ATOMIC FORCE MICROSCOPE.* Physical Review Letters, 1986. **56**(9): p. 930-933.
59. Butt, H.-J., B. Cappella, and M. Kappl, *Force measurements with the atomic force microscope: Technique, interpretation and applications.* Surface Science Reports, 2005. **59**(1–6): p. 1-152.
60. García, R. and R. Pérez, *Dynamic atomic force microscopy methods.* Surface Science Reports, 2002. **47**(6–8): p. 197-301.
61. Xu, S.H. and M.F. Arnsdorf, *Electrostatic Force Microscope for Probing Surface-Charges in Aqueous-Solutions.* Proceedings of the National Academy of Sciences of the United States of America, 1995. **92**(22): p. 10384-10388.
62. Nonnenmacher, M., M.P. Oboyle, and H.K. Wickramasinghe, *Kelvin Probe Force Microscopy.* Applied Physics Letters, 1991. **58**(25): p. 2921-2923.
63. Hartmann, U., *Magnetic force microscopy.* Annual Review of Materials Science, 1999. **29**: p. 53-87.
64. Zhang, L., et al., *Nanostructural conductivity and surface-potential study of low-field-emission carbon films with conductive scanning probe microscopy.* Applied Physics Letters, 1999. **75**(22): p. 3527-3529.

65. Gruverman, A., et al., *Domain-Structure and Polarization Reversal in Ferroelectrics Studied by Atomic-Force Microscopy.* Journal of Vacuum Science & Technology B, 1995. **13**(3): p. 1095-1099.
66. Melitz, W., et al., *Kelvin probe force microscopy and its application.* Surface Science Reports, 2011. **66**(1): p. 1-27.
67. Lu, J., et al., *Kelvin probe force microscopy on surfaces: Investigation of the surface potential of self-assembled monolayers on gold.* Langmuir, 1999. **15**(23): p. 8184-8188.
68. Saraf, S. and Y. Rosenwaks, *Local measurement of semiconductor band bending and surface charge using Kelvin probe force microscopy.* Surface Science, 2005. **574**(2-3): p. L35-L39.
69. Kokawa, R., et al., *Kelvin Probe Force Microscopy Study of a Pt/TiO2 Catalyst Model Placed in an Atmospheric Pressure of N2 Environment.* Chemistry-an Asian Journal, 2012. **7**(6): p. 1251-1255.
70. Borowik, L., et al., *Measuring the lifetime of silicon nanocrystal solar cell photo-carriers by using Kelvin probe force microscopy and x-ray photoelectron spectroscopy.* Nanotechnology, 2014. **25**(26).
71. Sengupta, E., et al., *Photoinduced Degradation Studies of Organic Solar Cell Materials Using Kelvin Probe Force and Conductive Scanning Force Microscopy.* Journal of Physical Chemistry C, 2011. **115**(40): p. 19994-20001.
72. Franke, K., et al., *Modification and detection of domains on ferroelectric PZT films by scanning force microscopy.* Surface Science, 1994. **302**(1): p. L283-L288.
73. Jesse, S., B. Mirman, and S.V. Kalinin, *Resonance enhancement in piezoresponse force microscopy: Mapping electromechanical activity, contact stiffness, and Q factor.* Applied Physics Letters, 2006. **89**(2).
74. Sader, J.E., *Frequency response of cantilever beams immersed in viscous fluids with applications to the atomic force microscope.* Journal of Applied Physics, 1998. **84**(1): p. 64-76.
75. Rodriguez, B.J., et al., *Dual-frequency resonance-tracking atomic force microscopy.* Nanotechnology, 2007. **18**(47).
76. Jesse, S., A.P. Baddorf, and S.V. Kalinin, *Switching spectroscopy piezoresponse force microscopy of ferroelectric materials.* Applied Physics Letters, 2006. **88**(6): p. 062908.

77. Stephen, J., et al., *The band excitation method in scanning probe microscopy for rapid mapping of energy dissipation on the nanoscale.* Nanotechnology, 2007. **18**(43): p. 435503.
78. Chen, Q.N., et al., *Delineating local electromigration for nanoscale probing of lithium ion intercalation and extraction by electrochemical strain microscopy.* Applied Physics Letters, 2012. **101**(6).
79. Chen, Q.N., S.B. Adler, and J.Y. Li, *Imaging space charge regions in Sm-doped ceria using electrochemical strain microscopy.* Applied Physics Letters, 2014. **105**(20).
80. Sekhon, J.S., L. Aggarwal, and G. Sheet, *Voltage induced local hysteretic phase switching in silicon.* Applied Physics Letters, 2014. **104**(16).
81. Proksch, R., *Electrochemical strain microscopy of silica glasses.* Journal of Applied Physics, 2014. **116**(6).
82. Chen, Q.N., et al., *Mechanisms of electromechanical coupling in strain based scanning probe microscopy.* Applied Physics Letters, 2014. **104**(24).
83. Porti, M., M. Nafria, and X. Aymerich, *Current limited stresses of SiO2 gate oxides with conductive atomic force microscope.* Ieee Transactions on Electron Devices, 2003. **50**(4): p. 933-940.
84. Pantel, D., et al., *Room-Temperature Ferroelectric Resistive Switching in Ultrathin Pb(Zr0.2Ti0.8)O-3 Films.* Acs Nano, 2011. **5**(7): p. 6032-6038.
85. Nguyen, C.V., et al., *Carbon nanotube tip probes: stability and lateral resolution in scanning probe microscopy and application to surface science in semiconductors.* Nanotechnology, 2001. **12**(3): p. 363-367.
86. Lee, H.J. and S.M. Park, *Electrochemistry of conductive polymers. 30. Nanoscale measurements of doping distributions and current-voltage characteristics of electrochemically deposited polypyrrole films.* Journal of Physical Chemistry B, 2004. **108**(5): p. 1590-1595.
87. Nazri, G.A. and G. Pistoia, eds. *Lithium Batteries Science and Technology*. 2004, Kluwer Academic Publishers.
88. Maier, J., *Nanoionics: ion transport and electrochemical storage in confined systems.* Nature Materials, 2005. **4**(11): p. 805-815.

89. Ji, L.W., et al., *Recent developments in nanostructured anode materials for rechargeable lithium-ion batteries.* Energy & Environmental Science, 2011. **4**(8): p. 2682-2699.
90. Kim, M.G. and J. Cho, *Reversible and High-Capacity Nanostructured Electrode Materials for Li-Ion Batteries.* Advanced Functional Materials, 2009. **19**(10): p. 1497-1514.
91. Liu, J. and D.F. Xue, *Hollow Nanostructured Anode Materials for Li-Ion Batteries.* Nanoscale Res Lett, 2010. **5**(10): p. 1525-1534.
92. Manthiram, A., et al., *Nanostructured electrode materials for electrochemical energy storage and conversion.* Energy & Environmental Science, 2008. **1**(6): p. 621-638.
93. Lee, S.W., et al., *High-power lithium batteries from functionalized carbon-nanotube electrodes.* Nature Nanotechnology, 2010. **5**(7): p. 531-537.
94. Kim, C., et al., *Fabrication of electrospinning-derived carbon nanofiber webs for the anode material of lithium-ion secondary batteries.* Advanced Functional Materials, 2006. **16**(18): p. 2393-2397.
95. Lytle, J.C., et al., *The right kind of interior for multifunctional electrode architectures: carbon nanofoam papers with aperiodic submicrometre pore networks interconnected in 3D.* Energy & Environmental Science, 2011. **4**(5): p. 1913-1925.
96. Yoo, E., et al., *Large reversible Li storage of graphene nanosheet families for use in rechargeable lithium ion batteries.* Nano Letters, 2008. **8**(8): p. 2277-2282.
97. Derrien, G., et al., *Nanostructured Sn-C composite as an advanced anode material in high-performance lithium-ion batteries.* Advanced Materials, 2007. **19**(17): p. 2336-2340.
98. Huang, X., et al., *Graphene-based composites.* Chemical Society Reviews, 2012. **41**(2): p. 666-686.
99. Qie, L., et al., *Nitrogen-Doped Porous Carbon Nanofiber Webs as Anodes for Lithium Ion Batteries with a Superhigh Capacity and Rate Capability.* Advanced Materials, 2012. **24**(15): p. 2047-2050.
100. Wangxi, Z., L. Jie, and W. Gang, *Evolution of structure and properties of PAN precursors during their conversion to carbon fibers.* Carbon, 2003. **41**(14): p. 2805-2812.
101. Bahl, O.P. and L.M. Manocha, *Characterization of oxidised pan fibres.* Carbon, 1974. **12**(4): p. 417-423.

102. Doshi, J. and D.H. Reneker, *Electrospinning process and applications of electrospun fibers.* Journal of Electrostatics, 1995. **35**(2–3): p. 151-160.
103. Reneker, D.H. and I. Chun, *Nanometre diameter fibres of polymer, produced by electrospinning.* Nanotechnology, 1996. **7**(3): p. 216-223.
104. Li, D. and Y.N. Xia, *Electrospinning of nanofibers: Reinventing the wheel?* Advanced Materials, 2004. **16**(14): p. 1151-1170.
105. Greiner, A. and J.H. Wendorff, *Electrospinning: A fascinating method for the preparation of ultrathin fibres.* Angewandte Chemie-International Edition, 2007. **46**(30): p. 5670-5703.
106. Sun, Z.C., et al., *Compound core-shell polymer nanofibers by co-electrospinning.* Advanced Materials, 2003. **15**(22): p. 1929-1932.
107. Bazilevsky, A.V., A.L. Yarin, and C.M. Megaridis, *Co-electrospinning of core-shell fibers using a single-nozzle technique.* Langmuir, 2007. **23**(5): p. 2311-2314.
108. Li, D. and Y.N. Xia, *Direct fabrication of composite and ceramic hollow nanofibers by electrospinning.* Nano Letters, 2004. **4**(5): p. 933-938.
109. Yu, Y., et al., *Encapsulation of Sn@carbon Nanoparticles in Bamboo-like Hollow Carbon Nanofibers as an Anode Material in Lithium-Based Batteries.* Angewandte Chemie-International Edition, 2009. **48**(35): p. 6485-6489.
110. Wang, X.Y., et al., *Electrospun nanofibrous membranes for highly sensitive optical sensors.* Nano Letters, 2002. **2**(11): p. 1273-1275.
111. Mai, L.Q., et al., *Electrospun Ultralong Hierarchical Vanadium Oxide Nanowires with High Performance for Lithium Ion Batteries.* Nano Letters, 2010. **10**(11): p. 4750-4755.
112. Gopal, R., et al., *Electrospun nanofibrous filtration membrane.* Journal of Membrane Science, 2006. **281**(1-2): p. 581-586.
113. Agarwal, S., J.H. Wendorff, and A. Greiner, *Use of electrospinning technique for biomedical applications.* Polymer, 2008. **49**(26): p. 5603-5621.
114. Ma, Z.W., et al., *Potential of nanofiber matrix as tissue-engineering scaffolds.* Tissue Engineering, 2005. **11**(1-2): p. 101-109.
115. Li, Z.Q., et al., *X-ray diffraction patterns of graphite and turbostratic carbon.* Carbon, 2007. **45**(8): p. 1686-1695.

116. Oberlin, A., *CARBONIZATION AND GRAPHITIZATION.* Carbon, 1984. **22**(6): p. 521-541.
117. Brunauer, S., et al., *On a Theory of the van der Waals Adsorption of Gases.* Journal of the American Chemical Society, 1940. **62**(7): p. 1723-1732.
118. Sing, K.S.W., *Reporting physisorption data for gas/solid systems with special reference to the determination of surface area and porosity (Provisional).* Pure and Applied Chemistry, 2009. **54**(11): p. 2201-2218.
119. Sing, K., *The use of nitrogen adsorption for the characterisation of porous materials.* Colloids and Surfaces A: Physicochemical and Engineering Aspects, 2001. **187–188**(0): p. 3-9.
120. Suhas, P.J.M. Carrott, and M.M.L. Ribeiro Carrott, *Lignin – from natural adsorbent to activated carbon: A review.* Bioresource Technology, 2007. **98**(12): p. 2301-2312.
121. Feaver, A. and G. Cao, *Activated carbon cryogels for low pressure methane storage.* Carbon, 2006. **44**(3): p. 590-593.
122. Brittain, S.T., et al., *The use of soft lithography for the fabrication of components for micro electromechanical systems (MEMS).* Abstracts of Papers of the American Chemical Society, 1998. **216**: p. U312-U312.
123. Xia, Y.N. and G.M. Whitesides, *Soft lithography.* Angewandte Chemie-International Edition, 1998. **37**(5): p. 550-575.
124. Orton, J.W. and C.T. Foxon, *Group III nitride semiconductors for short wavelength light-emitting devices.* Reports on Progress in Physics, 1998. **61**(1): p. 1-75.
125. Ferry, V.E., et al., *Light trapping in ultrathin plasmonic solar cells.* Optics Express, 2010. **18**(13): p. A237-A245.
126. Kang, M.G., et al., *Organic Solar Cells Using Nanoimprinted Transparent Metal Electrodes.* Advanced Materials, 2008. **20**(23): p. 4408-4413.
127. Whitesides, G.M., et al., *Soft lithography in biology and biochemistry.* Annual Review of Biomedical Engineering, 2001. **3**: p. 335-373.
128. Qin, D., Y.N. Xia, and G.M. Whitesides, *Soft lithography for micro- and nanoscale patterning.* Nature Protocols, 2010. **5**(3): p. 491-502.
129. Chou, S.Y., P.R. Krauss, and P.J. Renstrom, *IMPRINT OF SUB-25 NM VIAS AND TRENCHES IN POLYMERS.* Applied Physics Letters, 1995. **67**(21): p. 3114-3116.

130. Chou, S.Y., P.R. Krauss, and P.J. Renstrom, *Nanoimprint lithography*. Journal of Vacuum Science & Technology B, 1996. **14**(6): p. 4129-4133.
131. Jiang, J.A., et al., *Building one-dimensional oxide nanostructure arrays on conductive metal substrates for lithium-ion battery anodes.* Nanoscale, 2011. **3**(1): p. 45-58.
132. Lee, S.H., et al., *Graphene-Nanotube-Iron Hierarchical Nanostructure as Lithium Ion Battery Anode.* Acs Nano, 2013. **7**(5): p. 4242-4251.
133. Sun, K., et al., *3D Printing of Interdigitated Li-Ion Microbattery Architectures.* Advanced Materials, 2013. **25**(33): p. 4539-4543.
134. Choi, S., et al., *General Approach for High-Power Li-Ion Batteries: Multiscale Lithographic Patterning of Electrodes.* Chemsuschem, 2014. **7**(12): p. 3483-3490.
135. Taberna, L., et al., *High rate capabilities Fe3O4-based Cu nano-architectured electrodes for lithium-ion battery applications.* Nature Materials, 2006. **5**(7): p. 567-573.
136. Mills, E., et al., *Silicon nanopillar anodes for lithium-ion batteries using nanoimprint lithography with flexible molds.* Journal of Vacuum Science & Technology B, 2014. **32**(6).
137. Martinez-Duarte, R., P. Renaud, and M.J. Madou, *A novel approach to dielectrophoresis using carbon electrodes.* Electrophoresis, 2011. **32**(17): p. 2385-2392.
138. Curtis, B.J., *The precipitation of graphite from the hexaborides of some rare earth elements and yttrium.* Carbon, 1966. **4**(4): p. 483-488.
139. Guerin, K., et al., *On the irreversible capacities of disordered carbons in lithium-ion rechargeable batteries.* Electrochimica Acta, 2000. **45**(10): p. 1607-1615.
140. Reich, S. and C. Thomsen, *Raman spectroscopy of graphite.* Philosophical Transactions of the Royal Society a-Mathematical Physical and Engineering Sciences, 2004. **362**(1824): p. 2271-2288.
141. Cuesta, A., et al., *Raman Microprobe Studies on Carbon Materials.* Carbon, 1994. **32**(8): p. 1523-1532.
142. Olivier, J., S. Kilani, and R. Poirier, *Determination in Low-Energy Electron Loss Spectroscopy of the Gaussian and Lorentzian Content of Experimental Line-Shapes.* Applied Surface Science, 1981. **8**(3): p. 353-358.

143. Dillon, R.O., J.A. Woollam, and V. Katkanant, *Use of Raman-Scattering to Investigate Disorder and Crystallite Formation in as-Deposited and Annealed Carbon-Films.* Physical Review B, 1984. **29**(6): p. 3482-3489.
144. Knight, D.S. and W.B. White, *Characterization of Diamond Films by Raman-Spectroscopy.* Journal of Materials Research, 1989. **4**(2): p. 385-393.
145. Toader, M., et al., *Conductive AFM for CNT characterization.* Nanoscale Research Letters, 2013. **8**(24).
146. Balke, N., et al., *Decoupling Electrochemical Reaction and Diffusion Processes in Ionically-Conductive Solids on the Nanometer Scale.* Acs Nano, 2010. **4**(12): p. 7349-7357.
147. Jesse, S., B. Mirman, and S.V. Kalinin, *Resonance enhancement in piezoresponse force microscopy: Mapping electromechanical activity, contact stiffness, and Q factor.* Applied Physics Letters, 2006. **89**(2): p. 022906.
148. Chen, Q.N., et al., *Delineating local electromigration for nanoscale probing of lithium ion intercalation and extraction by electrochemical strain microscopy.* Applied Physics Letters, 2012. **101**(6): p. 063901.
149. Chen, W., et al., *Efficient and stable large-area perovskite solar cells with inorganic charge extraction layers.* Science, 2015. **350**(6263): p. 944-948.
150. Yang, W.S., et al., *High-performance photovoltaic perovskite layers fabricated through intramolecular exchange.* Science, 2015. **348**(6240): p. 1234-1237.
151. Xing, G., et al., *Long-Range Balanced Electron- and Hole-Transport Lengths in Organic-Inorganic CH3NH3PbI3.* Science, 2013. **342**(6156): p. 344-347.
152. Takahashi, Y., et al., *Hall mobility in tin iodide perovskite CH3NH3SnI3: Evidence for a doped semiconductor.* Journal of Solid State Chemistry, 2013. **205**: p. 39-43.
153. Wehrenfennig, C., et al., *High Charge Carrier Mobilities and Lifetimes in Organolead Trihalide Perovskites.* Advanced Materials, 2014. **26**(10): p. 1584-1589.
154. Stoumpos, C.C., C.D. Malliakas, and M.G. Kanatzidis, *Semiconducting Tin and Lead Iodide Perovskites with Organic Cations: Phase Transitions, High Mobilities, and Near-Infrared Photoluminescent Properties.* Inorganic Chemistry, 2013. **52**(15): p. 9019-9038.
155. Kim, H.S., et al., *Lead Iodide Perovskite Sensitized All-Solid-State Submicron Thin Film Mesoscopic Solar Cell with Efficiency Exceeding 9%.* Scientific Reports, 2012. **2**: p. 591.

156. Morozovska, A.N., et al., *Thermodynamics of electromechanically coupled mixed ionic-electronic conductors: Deformation potential, Vegard strains, and flexoelectric effect.* Physical Review B, 2011. **83**(19): p. 195313.
157. Chen, Q.N., et al., *Mechanisms of electromechanical coupling in strain based scanning probe microscopy.* Applied Physics Letters, 2014. **104**(24): p. 242907.
158. Proksch, R., *Electrochemical strain microscopy of silica glasses.* Journal of Applied Physics, 2014. **116**(6): p. 066804.
159. Eshghinejad, A., et al., *Scanning thermo-ionic microscopy for probing local electrochemistry at the nanoscale.* Journal of Applied Physics, 2016. **119**(20): p. 205110.
160. Lee, M.-J., et al., *A fast, high-endurance and scalable non-volatile memory device made from asymmetric Ta2O5−x/TaO2−x bilayer structures.* Nature Materials, 2011. **10**(8): p. 625-630.
161. Wen, Z., et al., *Ferroelectric-field-effect-enhanced electroresistance in metal/ferroelectric/semiconductor tunnel junctions.* Nature Materials, 2013. **12**(7): p. 617-621.
162. Di, W., et al., *Nonvolatile multibit Schottky memory based on single n-type Ga doped CdSe nanowires.* Nanotechnology, 2012. **23**(48): p. 485203.
163. Kwon, D.-H., et al., *Atomic structure of conducting nanofilaments in TiO2 resistive switching memory.* Nat Nano, 2010. **5**(2): p. 148-153.
164. Zhou, Y., et al., *Voltage-Triggered Ultrafast Phase Transition in Vanadium Dioxide Switches.* IEEE Electron Device Letters, 2013. **34**(2): p. 220-222.
165. Pantel, D., et al., *Room-Temperature Ferroelectric Resistive Switching in Ultrathin Pb(Zr0.2Ti0.8)O3 Films.* Acs Nano, 2011. **5**(7): p. 6032-6038.
166. Pan, F., et al., *Nonvolatile resistive switching memories-characteristics, mechanisms and challenges.* Progress in Natural Science: Materials International, 2010. **20**: p. 1-15.
167. Liu, Y., et al., *Ferroelectric switching of elastin.* Proceedings of the National Academy of Sciences, 2014. **111**(27): p. E2780-E2786.
168. Liu, Y., et al., *Glucose Suppresses Biological Ferroelectricity in Aortic Elastin.* Physical Review Letters, 2013. **110**(16): p. 168101.
169. Liu, Y., et al., *Biological Ferroelectricity Uncovered in Aortic Walls by Piezoresponse Force Microscopy.* Physical Review Letters, 2012. **108**(7): p. 078103.

170. Li, J., et al., *Molecular ferroelectrics: where electronics meet biology.* Physical Chemistry Chemical Physics, 2013. **15**(48): p. 20786-20796.
171. Pasquali-Ronchetti, I., et al., *Structure and composition of the elastin fibre in normal and pathological conditions.* Micron, 1993. **24**(1): p. 75-89.
172. Daamen, W.F., et al., *Elastin as a biomaterial for tissue engineering.* Biomaterials, 2007. **28**(30): p. 4378-4398.
173. Baldock, C., et al., *Shape of tropoelastin, the highly extensible protein that controls human tissue elasticity.* Proceedings of the National Academy of Sciences, 2011. **108**(11): p. 4322-4327.
174. Kalinin, S.V., et al., *Nanoscale Electromechanics of Ferroelectric and Biological Systems: A New Dimension in Scanning Probe Microscopy.* Annual Review of Materials Research, 2007. **37**(1): p. 189-238.

VITA

Education

University of Washington, Seattle

Ph.D. Mechanical Engineering/Nanotechnology & Molecular Engineering, 2016

University of Washington, Seattle

M.S. Applied Mathematics, 2016

Tsinghua University, Beijing, China

B.S. Materials Science & Engineering, 2011

Experience

University of Washington, Multifunctional Materials Laboratory 9/2011-8/2016

Graduate Student Researcher

- Electrospun carbon nanofibers using polyvinylpyrrolidone as polymer precursor for lithium ion battery anodes, fully characterized the microstructure and chemical component of the nanofibers, optimized the nanofiber porosity by post activation process, assembled coin cell batteries to evaluate the electrochemical performance.
- Fabricated carbon thin film electrodes with patterned periodic structure using nanoimprint lithography to improve the specific volumetric capacity when used as anode for lithium ion batteries, and investigated on the cause of the improved capacity using electrochemical strain microscopy.
- Established strong proof of ferroelectricity in organic-inorganic perovskite $CH_3NH_3PbI_3$ films using piezoresponse force microscopy in combination with macroscopic ferroelectric property measurement, directly observed the photo-induced charge generation process through measuring the surface potential distribution, and observed the photo-induced ferroelectric switching behavior.
- Developed experimental procedures to study the resistivity switching behaviors in bio-ferroelectric tissues elastin and also in oxides.

Applied Materials, Office of the CTO **6/2015-9/2015**

Associate Intern

- Participated in the optimization of polymer based ink formulation, focusing on the formulation component tuning and rheology properties characterization, including the surface tension, viscosity and dynamic contact angle.
- Researched on various 3D Printing technologies: material capabilities, print resolution and cost-effective analysis.

Argonne National Laboratory **6/2014-9/2014**

Summer Research Student

- Examined the reliability of benzene based redox molecules for overcharge protection of lithium ion batteries cathodes, by assembling coin cell batteries in both half cell and full cell configurations for extreme overcharge condition testing.
- Planned and executed design of experiments to evaluate the functionality of the same redox molecules for non-aqueous redox flow batteries, focusing on improving the solubility and stability in the solvent.

Honors

Guachuan Excellent Student Scholar	2009
Excellent Student Leadership	2009
China Open Excellent Volunteer	2008

Publications

- **Wang, P.**; Zhang, D. et al, Mesoporous carbon nanofibers with a high surface area electrospun from thermoplastic polyvinylpyrrolidone. *Nanoscale,*2012
- **Wang, P.**; Chen, Q.; Xie, S. et al, Enhanced lithium ion storage in nanoimprinted carbon. *App Phys Lett*, 2015
- **Wang, P.**; Zhao, J. et al, Photo-induced ferroelectric switching in perovskite $CH_3NH_3PbI_3$ films. *Under Preparation*, 2016
- **Wang, P**.; Chen, Y.; Li, J. et al, Resistivity switching of ferroelectric elastin. *Under Preparation*, 2016

- Eshghinejad, A.; Esfahani, E.; **Wang, P**.; Li, J. et al, Scanning Thermo-ionic Microscopy for Probing Local Electrochemistry at the Nanoscale. Submitted to *Journal of Applied Physics*, 2016
- Huang, J.; Cheg, L.; Assary, R.; **Wang, P**. et al, Liquid Catholyte Molecules for Nonaqueous Redox Flow Batteries. *Advanced Energy Materials*, 2014
- Huang, J.; Shkrob, IA.; **Wang, P**.; et al, 1, 4-Bis (trimethylsilyl)-2, 5-dimethoxybenzene: a novel redox shuttle additive for overcharge protection in lithium-ion batteries that doubles as a mechanistic chemical probe. *J of Materials Chemistry A*, 2015
- Liu, Y.; Cai, HL.; Zelisko, M.; Wang, Y.; Sun, J.; Yan, F.; Ma, F.; **Wang, P**.; et al, Ferroelectric switching of elastin. *Proceedings of the National Academy of Sciences*, 2014